NGC 1052
A study of the parsec–scale twin jet

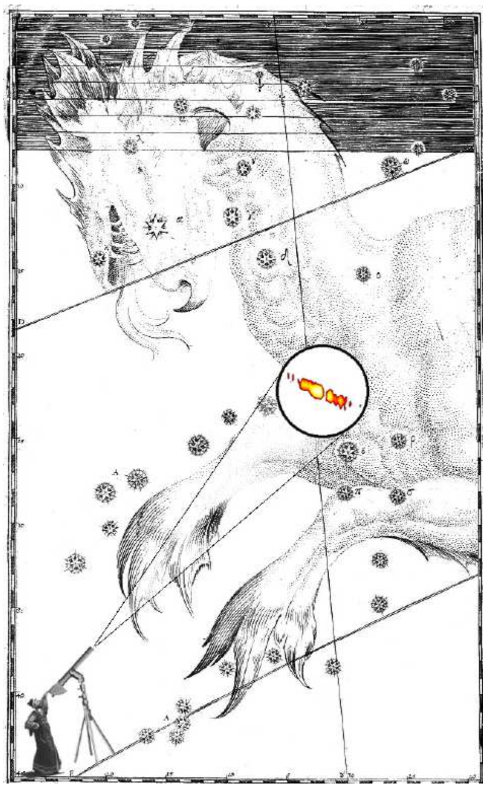

Diplomarbeit im Fach Physik angefertigt im
Max-Planck-Institut für Radioastronomie in Bonn
vorgelegt von
Matthias Kadler

Betreuer: Dr. E. Ros Ibarra
Referent: PD Dr. H. Falcke
Koreferent: Prof. Dr. U. Klein

vorgelegt der
Mathematisch-Naturwissenschaftliche Fakultät der
Rheinischen Friedrich-Wilhelms-Universität Bonn
Juni 2002

Preface

In this diploma thesis the active nucleus of the elliptical galaxy NGC 1052 is studied with the technique of Very Long Baseline Interferometry (VLBI). The radio core of NGC 1052 is unusually bright and compact. Together with the proximity of the source of only about 20 Mpc this makes NGC 1052 a premier object for VLBI studies, aiming at the ultimate goal to reveal the nature of the physical processes at work in such active galactic nuclei (AGN). The source offers a variety of interesting peculiarities over the whole range of observable frequencies that have been studied in great detail over the last decades. However, many questions have remained unanswered heretofore and this diploma thesis is my attempt to answer at least some of them.

The standard model for AGN consists of only a small number of basic ingredients. A supermassive black hole at the very center of the galaxy is surrounded by an accretion disk, which feeds the black hole. In this process enormous amounts of energy are released, making this type of objects bright enough to outshine the starlight from their whole host galaxy by orders of magnitude. A twin jet emanates from the nucleus and transports a synchrotron radiation emitting plasma along two channels back to back out of the black hole′s reach. Finally, a dusty molecular torus, forms the outer extension of the accretion disk. Depending on the geometry of the system a substantial fraction of the receding jet might be covered by this obscuring torus. Evidence for such an "obscuring geometry" can come from the detection of free-free absorbing regions towards the (receding) counter-jet. The spectral signature of free-free absorption is a steep decrease towards low frequencies, a strongly inverted spectrum.

NGC 1052 is one of the most promising candidates for detailed studies of the obscuring torus and therefore for the exploration of the very vicinity of a supermassive black hole. In this thesis the radio core of NGC 1052 is investigated by the analysis of VLBI data at four frequencies and in full polarization mode. Free-free absorption is detected towards both of the two nuclear jets, on the eastern side spatially coinciding with a region of linearly polarized emission at 5 GHz. The detailed analysis of the available data constrains the physical parameters of the torus. Complementarily to the VLBI studies of the compact radio core, the X-ray structure of NGC 1052 is revealed by the analysis of archival CHANDRA data. Analyzing the X-ray spectrum of the (spatially unresolved) core–region substantiates the necessity of a central absorber in order to explain the data. In addition to this, imaging the extended emission results in the first detection of the X-ray jet of NGC 1052.

I will start with an introduction to AGN, their standard model and the unified scheme of AGN in Chapter 1. In Chapter 2 the theoretical background necessary for the understanding of the later chapters is presented. In Chapter 3 the VLBA, the telescope array used for the VLBI observations of NGC 1052, is introduced and the observations and the VLBI data reduction are presented. The results derived from these observations are presented and discussed in Chapter 4. Chapter 5 summarizes the various results derived in Chapter 4 and tries to fit them into a complete picture of the twin jet of NGC 1052. Separated from the main goal of this thesis the CHANDRA and supplementary MERLIN observations and their data reduction are presented in the appendices.

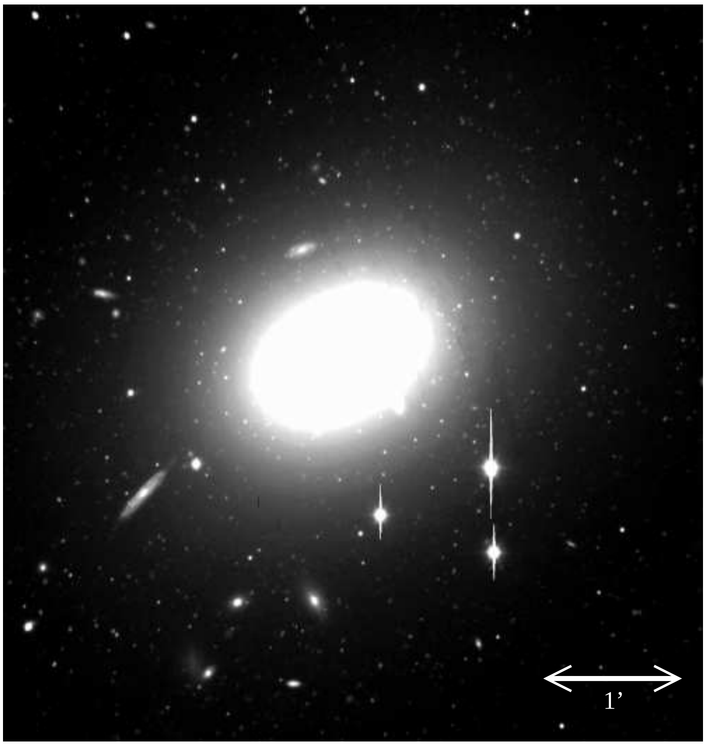

Cover: Assembly of two copperplate prints by Bayer (1603) and Hevelius (1690). This page: The optical structure of NGC 1052 (taken with the Keck telescope by Forbes et al. 2001).

Contents

List of Figures

Chapter 1

Introduction

1.1 The radio sky

The heavens have always fascinated mankind and inspired poets and artists for ages. Myths have been formed which linked human fate to the stars, and early cultures found their gods manifested in the pictures painted in the sky by the constellations of stars. However, anything that has been discovered during the age of the early astronomy turned out to be just one piece of a much bigger puzzle when scientists began to explore the sky at wavelengths invisible to the human eye. At the beginning of the 20th century it was already recognized that visible light was just one special form of electromagnetic radiation which turns into radio radiation if the waves become longer and into X-rays if the waves become shorter. However, nobody looked for any kind of electromagnetic radiation from space besides the light from the Sun and the stars. We first had to invent artificial radio transmitters before we recognized that the whole sky was already totally populated by them. It was Karl Jansky who found in 1931 that a detectable radio signal in his measurements was extraterrestrial in origin. Later it turned out that the extraterrestrial source of radio radiation which Jansky detected was the center of our own star system, the Milky Way, today called Sgr A.

Today we know what the sky looks like across the spectrum, from the X-ray regime, passing the optical and the infrared to the radio wavelengths. Each wavelength regime that became usable to astronomy after the development of new observing techniques showed new mysteries making the overall picture of the universe we live in even more fascinating than it had been to the naked eye alone before. Figure 1.1 shows the radio sky at 408 MHz (73 cm) in Galactic coordinates (the Galactic Center in the middle). This map of the whole sky is the product of about 15 years of observations between 1967 and 1982 with two radio telescopes in the Northern Hemisphere, located at Effelsberg (Germany) and Jodrell Bank (England), and the Parkes telescope in Australia. It shows the distribution of the galactic synchrotron radiation (see chapter 2.1) across the sky, which is responsible for nearly all of the extended and smooth radiation in the map. In contrast to the optical, where the central region of the Milky Way is completely hidden behind dark clouds, it is clearly visible as the region of the strongest synchrotron emission in the radio regime.

Only a few discrete sources are strong enough to be clearly seen distinct from the extended emission, in contrast to the optical view of the Milky Way being dominated by many stars (discrete sources) and underlaid with some extended emission. Only one of

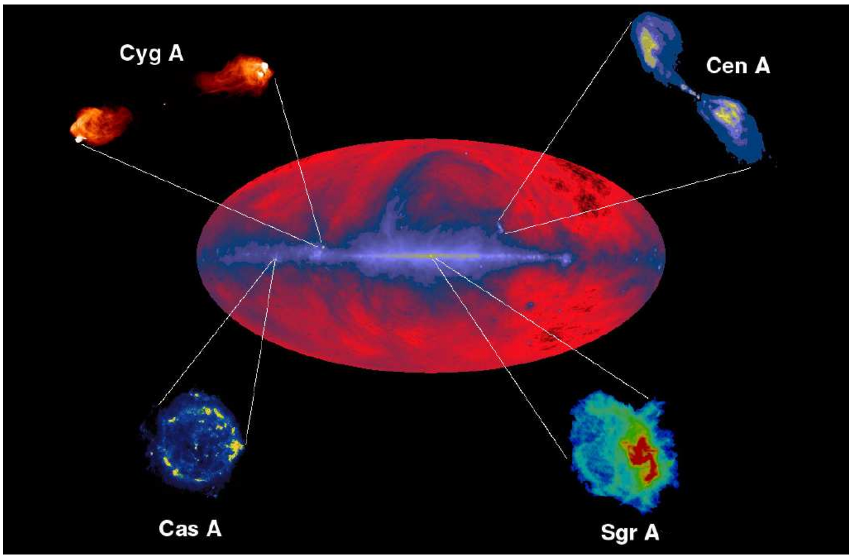

Figure 1.1: The radio sky at 408 MHz (73 cm). The map was produced from the combined data of three radio telescopes, Effelsberg, Jodrell Bank and Parkes taken between 1967 and 1982. The positions of four famous radio sources are indicated: Two radio galaxies, Cygnus A and Centaurus A, a supernova remnant, Cassiopeia A and the center of the Milky Way, Sgr A. The images of Cen A and Cas A are taken from the NRAO image gallery (`www.nrao.edu.imagegallery`). The Cyg A map is shown by courtesy of C. Carilli and the Sgr A image is from Yusef-Zadeh et al. (2000). The 408 MHz all sky map was generated by G. Haslam (MPIfR).

these sources (Cen A) shows structure, all other sources are unresolved, i.e., they appear point–like to a telescope of 70 m[1] in diameter operating at 408 MHz. The resolution of a radio telescope is given by:

$$\Delta\theta = 1.22 \times \frac{\lambda}{D} \tag{1.1}$$

where λ is the wavelength, D is the diameter of the telescope and $\Delta\theta$ is the smallest angular distance which still can be resolved. Thus, in order to find out more about the structure of these sources one had to go to lower wavelengths and/or larger instruments. Although it is technically not possible to build single fully steerable telescopes much bigger than 100 m, the use of interferometric techniques (see chapter 3) allows one to observe with instruments of an effective size of hundreds or even thousands of kilometers. Four of the most prominent discrete sources are shown with higher resolution in Figure 1.1 as they are seen by the Very Large Array (VLA), a connected telescope array of 27 antennas, located in New Mexico, US. Bottom right is a map of the first known extra–solar radio source, Sgr A, which is located at the center of our own galaxy. Bottom left is a map of the strongest discrete radio source visible in the sky, Cas A, a supernova remnant of a star which exploded around 1680. Top left and top right are VLA maps of two radio galaxies, Cyg A and Cen A. Both seem to have a core from which matter is transported along two channels outwards. In usual terminology such a morphology is called a jet. These sources, besides many others, could be identified in the optical regime with galaxies, indicating that there is a process at work which produces very high energies that makes these objects very bright even at these large distances. Radio galaxies are a subclass of the so called

[1] The data of Effelsberg (100 m), Jodrell Bank (76 m) and Parkes (70 m) had to be combined scaling down the resolution of the two bigger telescopes to $0\overset{\circ}{.}85$.

active galaxies. Besides the radio galaxies the most important members of this class of objects are the quasars, blazars and Seyfert galaxies. They all show very high–energetic processes, which are confined to a small region at their center. Sometimes the nuclei of these galaxies are a hundred times brighter than their entire starlight. The next section will deal with this "zoo" of active galaxies, introducing the different types of activity and putting them together into a unified scheme.

1.2 Active galaxies and the standard model of AGN

The term active galactic nucleus (AGN) describes a big variety of galactic nuclei, which are unusual compared to classical galaxies in different respects. A common definition is:

> *Active galactic nuclei are nuclei of galaxies which show energetic phenomena that cannot be clearly and directly attributed to stars.*

AGN are peculiar in luminosity, size, spectroscopic properties, variability and morphology. Sometimes an object shows signs of activity only in one respect but generally the phenomenology is more complex. Depending on their properties and the observing techniques used, AGNs were divided in different classes. Often this classification is not unique and there are different labels which can be given to a special object. However, there are a few things nearly all AGN have in common. First, they have a very broad spectral energy distribution (SED) and are thus among the brightest objects in all wavebands. Second, most AGN are strongly variable at all wavelengths and third, they are usually bright X–ray sources. In section 1.2.1 the most common classes of AGN and their similarities and differences shall be introduced. Section 1.2.2 will present the standard model for the underlying physics of AGN and in section 1.2.3 a unified scheme will try to explain the variety of active galactic nuclei with a small number of basic parameters which vary between the different classes, namely their luminosity, age, viewing angle and the so called radio loudness.

1.2.1 The zoo of active galaxies

Quasars and **QSOs** are both artificial words. The first means **qua**si **s**tell**a**r **ra**dio source, the latter **Q**uasi **S**tellar **O**bject. The difference between both terms is mainly historically in nature and is due to the fact that quasars are strong in the radio regime whereas QSOs are not. Nevertheless both names are used somewhat exchangeable as long as the context does not imply a special radio flux. Both classes appear star-like on optical photographs, have very high intrinsic brightnesses, and are usually found at very large distances[2]. For example, the brightest quasar 3C 273 is at a distance of $\sim$700 Mpc and has an optical magnitude of B=13 mag. This corresponds to an intrinsic brightness about a hundred times larger than that of the Galaxy. QSOs show very rich emission spectra with unusually broad lines (up to 10,000 km s^{-1}). These high line widths indicate that the emission comes from regions with a very high velocity dispersion, typical for a dense medium in a deep potential well.

[2]Bright objects are usually very rare. The tendency of quasars to be very far away is thus simply a selection effect due to the fact that rare objects are found predominantly at great distances.

Seyfert galaxies are less luminous than quasars and usually the host galaxy (in most cases a spiral) can be detected. Nevertheless, the core region of the galaxy is unusually bright. Seyfert galaxies are divided in two subclasses. Seyfert 1 galaxies have two sets of emission lines, one with narrow lines with full width at half maximum (FWHM) corresponding to several hundreds of km s^{-1} and additionally very broad lines with widths up to thousands of km s^{-1}. No broad forbidden lines are present. In contrast, Seyfert 2 galaxies only show narrow lines. The common interpretation is that the the broad lines originate in a gas of very high density (n_e=10^9 cm^{-3} or higher) very close to a massive, compact object (see 1.2.2) while the narrow lines originate in a low density gas (n_e=10^3–10^6 cm^{-3}) farther out. This is in agreement with the prediction that forbidden lines originate only in regions with small densities. Very important for unification models (see 1.2.3) was the detection of "hidden" broad line systems in many Seyfert 2 galaxies in polarized light. This is usually explained in terms of an obscuration effect in that the broad line region is hidden behind a central absorber but stays visible in scattered (and thus polarized) light. The transition from Seyferts to quasars is somewhat arbitrary. The strongest Seyfert 2 galaxies for example are brighter than the weakest quasars. This is simply due to the fact that an AGN which shows broad emission lines and appears star like will probably be classified as a quasar whereas it would have been classified as a Seyfert 1 galaxy if in a slightly deeper observation its weak starlight from the surrounding galaxy would had been detected.

LINERs in general are low luminosity AGN (LLAGN) with an optical spectrum similar to Seyfert 2 galaxies, except that the low–ionization lines are relatively strong. LINER is an acronym for **L**ow–**I**onization **N**uclear **E**mission–line **R**egion galaxies. Figure 1.2 shows the optical spectrum of the main target of this work, NGC 1052, which is often called the prototypical LINER, and the Seyfert 2 galaxy NGC 1667. LINERs are very common. They are found in nearly one third of all bright nearby galaxies (Ho et al. 1995). It is not clear if the whole class of LINERs can be seen as the low luminosity extension of the AGN phenomenon. Alternatively, some of the observed LINER spectra may actually be produced as the result of intense star formation[3]. Similarly to the Seyfert galaxies, about 15% of all LINERS show broad components of the Hα line. They can thus also be divided in the subclasses of LINER 1 and LINER 2 nuclei as those sources in which broad Hα lines are detected or undetected, respectively. Whether LINER 2 nuclei in general contain weak broad line systems or not is less clear than for their more luminous counterparts in the Seyfert class. At least in the case of NGC 1052 the broad wings of the Hα line have been shown to be polarized. Therefore, it seems that at least a subset of the LINER class resembles the Seyfert class in this respect.

Radio galaxies are galaxies which emit at radio frequencies. This trivial statement is probably the only definition which can be given in agreement with the various understanding that different people have about this term. Radio galaxies are often defined as galaxies which show radio structure on kpc–scale rather than compact sources, which in turn would be classified as quasars. On the other hand, the detection of an optical galaxy is often

[3]In the case of NGC 1052, however, many independent indicators as the radio jets, the X-ray flux and the detection of broad wings of the Hα line, underline its AGN nature. Additionally, its optical spectrum can well be explained in terms of a simple photoionization model, like in Seyfert galaxies (Gabel et al. 2000).

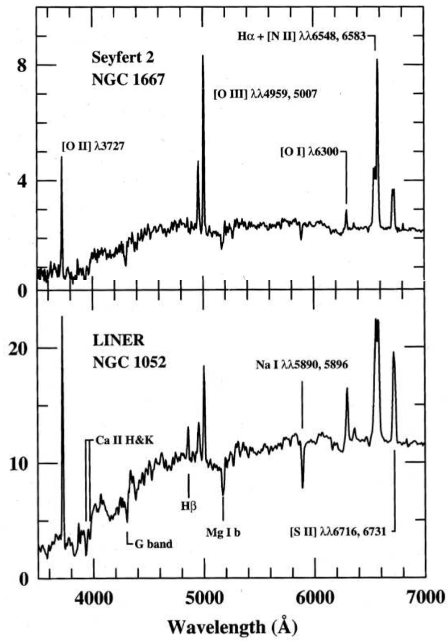

Figure 1.2: The optical spectra of the Seyfert 2 galaxy NGC 1667 and the LINER NGC 1052. Important differences are: The [OIII]/Hβ flux ratio is smaller in LINERs than in Seyfert 2 galaxies, and low–ionization lines ([NII], [SII], [OII] and [OI]) are relatively strong in LINER spectra. Plots taken from Peterson (1997), by courtesy of A. P. Filippenko.

taken as the criterion that turns a quasar into a radio galaxy. Depending on the presence or absence of a broad line system in the optical spectrum, radio galaxies are divided in broad line radio galaxies (BLRG) and narrow line radio galaxies (NLRG). In any case, radio galaxies represent only a small subset of the AGN class since only about 10–15% of all AGN are strong in the radio regime. These are also called radio-loud AGN, in contrast to radio-quiet AGN. A morphological classification is given in section 1.3.2 together with a presentation of the variety of radio sources on parsec– and kiloparsec–scales.

Blazars are radio sources containing a relativistic jet which is directed nearly towards the line of sight to the observer. The beamed jet emission (see section 2.3.1) forms a featureless continuum from the radio regime up to (occasionally hard) X-rays. They can be divided into two subclasses, namely, the BL Lac objects and the core dominated quasars. Emission and absorption lines in BL Lac objects are very weak, if not completely absent. The ones with detected emission lines tend to be at small redshifts. Core dominated quasars often show prominent emission lines which suggest on average higher redshifts. Both show very rapid variability in the optical regime with time scales often smaller than one day.

1.2.2 Basic ingredients of an AGN

In this section the main components of the standard model for AGN is introduced and the observational evidence for the corresponding component will be discussed briefly. Figure 1.3 shows a schematic image of an AGN in the standard model and the relative configuration of its general components.

The central engine – Black hole and accretion disk: Since the detection of AGN, the most fundamental task was to understand what physical mechanism is capable of releasing the enormous energies observed on scales, comparable to the size of the solar system. The only possibility is the accretion of matter onto a very compact object. In this process, the potential energy is converted into kinetic energy, which in turn can be released before the matter reaches the central object. The high observed luminosity (typically 10^{44}–$10^{48}\,\mathrm{erg\,s^{-1}}$ in luminous quasars) and the small scales derived, for example, from the upper limit on the size of unresolved radio cores of <1 pc provides a simple lower limit on the mass of the accreting object, the Eddington mass. The enormous radiation pressure in the surrounding of the central object requires at least this mass to secure that material in the accretion flow can still be gravitationally bound to the center of the galaxy. For a given luminosity of $L = 10^{46}\,\mathrm{erg\,s^{-1}}$ it can be estimated that at least a mass of $M_E = 0.8{\cdot}10^8\,M_\odot$ is needed to sustain the accretion flow. Such a large value implies that the accreting object could be a black hole.

There is increasing evidence for the presences of black holes in the centers of active galaxies and also in many, if not all, "normal" galaxies. The two major proofs are the measurement of radial and proper motion of stars around the center of our own galaxy at the Sgr A region (Eckart & Genzel 1996) and the detection of a set of moving maser spots in a Keplerian disk in NGC 4258 (Miyoshi et al. 1995). In both cases the derived mass density of the central source argues strongly towards the presence of a black hole of $2.6 \cdot 10^6\,\mathrm{M}_\odot$ in the case of our milky way and $3.6 \cdot 10^7\,\mathrm{M}_\odot$ in NGC 4258.

The accretion flow onto the black hole forms an accretion disk. In this disk, angular momentum is transported outwards by means of viscous friction, and matter is transported inwards. The big amount of released energy is due to the viscous friction, which cools the flow. Alternatively, a large fraction of the gained energy may not be radiated away but be transported with the flow inside the event horizon of the black hole. Obviously, the latter possibility cannot lead to as luminous objects as the former one. For this reason the latter solutions, which are called ADAFs (advection dominated accretion flows) are mainly applicable to low luminosity sources (LINERs, X-ray binaries,...). They have however, big problems in explaining the broadband SED of several objects, especially flat spectrum radio sources, without the inclusion of jets.

In many luminous AGN the optical spectrum exhibits a broad feature, called the big blue bump. This bump can in many cases be well explained by the blackbody radiation of an accretion disk. The absence of this bump in several flat spectrum low luminosity AGN argues towards a combination of a jet model (responsible for the radio emission and probably also the X-ray emission) and an ADAF. This is a very disputed topic and judging the debate is not within the scope of this thesis.

The circumnuclear medium – BLR, NLR and obscuring torus: The region around the putative accretion disk is filled by gas and dust. Three main components seem to describe this AGN surrounding: the broad line region (BLR), the narrow line region (NLR), and a molecular (dusty) torus. Since the emission lines are most likely Doppler broadened, the BLR is expected to be very close to the black hole, exhibiting a big velocity dispersion within the set of different emitting gas components. The NLR is the extension of the BLR at larger distances. In both cases, the volume-filling-factor is $\ll 1$, implying a very filamentary structure of both the BLR and the NLR. Although the BLR is very

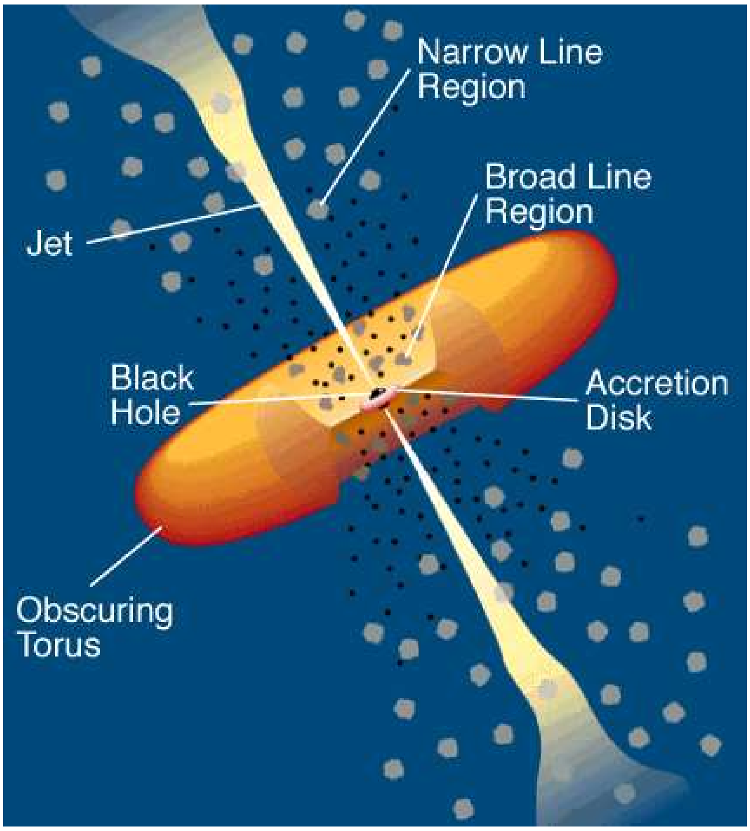

Figure 1.3: Sketch of the standard model, taken from the HEASARC website (`http://guinan.gsfc.nasa.gov`).

compact (smaller than a few tens of lightdays) and presently not resolvable with optical facilities, the NLRs of some AGN have been imaged successfully with the Hubble space telescope (e.g. Falcke et al. 1998). The morphology of the NLR is generally well described by a double–cone emanating from the core of the galaxy.

A small bump in the infrared regime, visible in many AGN spectra, finally suggests the presence of a warm, dusty component. In the unified scheme this dust is usually thought to be ordered in a torus–like structure, possibly being the outer extension part of the accretion disk. Depending on the viewing angle this torus can obscure the BLR, leaving only the emission from the more extended NLR left to observe. Recently, VLBI observations found evidence of such an obscuring absorber, which will be discussed in much more detail in later chapters of this work.

Jets, Hot spots and Lobes: Finally, every AGN is thought to harbor a more or less prominent twin jet, which is emanating perpendicular to the accretion disk. Each of the two jets penetrates the BLR and the NLR, travels on a linear path and finally terminates in a hot spot, the region of interaction between the jet and some kind of surrounding medium. The observed radio lobes represent either a backflow of jet material or the residue of the jet from an earlier epoch. Since these jet components of AGN are the topic of section 1.3 and 2.4, they shall only be listed here.

1.2.3 The unified scheme

With the basic ingredients of the standard model for AGN at hand – namely the supermassive black hole, the accretion disk, the broad and narrow line region, the jet and the obscuring torus – a unified scheme for the different types of AGN can be developed. The phenomenon of a pair of similar types which differ only in the presence or absence of a broad emission line system (Seyfert I/II, LINER I/II, BLRG/NLRG) can be explained with intrinsically only one type each, with the BLR visible or hidden behind the obscuring torus. A viewing angle roughly parallel to the symmetry axis of the torus will make a source appear as a type I object, a line of sight nearly perpendicular to this axis will make the object appear as a type II source. Additionally, this principle can be applied to quasars and radio galaxies. The difference between those is mainly that radio galaxies neither have a BLR nor an UV–bump and the radio cores of quasars are much stronger than in radio galaxies. Applying the same unification principle as above, the BLR and the accretion disk of radio galaxies are hidden behind the torus. In addition, the jet, oriented towards the observer in quasars and perpendicular to the symmetry axis of the torus, becomes Doppler-boosted (see section 2.3.1). In the case of radio galaxies and quasars, as well as for the Seyfert I/II and LINER I/II classes, this simple inclination model reproduces satisfactorily the relative numbers of the corresponding objects. The blazars fit in this scheme as the sources with the jet nearly directly pointing towards the observer. This explains the featureless continuum, since the boosted jet radiation outshines every line feature in the spectrum, as well as the fact that blazars are relatively rare. The small CSS and GPS sources (**C**ompact **S**teep **S**pectrum and **G**iga-Hertz **P**eaked **S**pectrum sources; see section 1.3.2) can be seen as the young radio galaxies and quasars. The remaining differences can be explained in terms of different power and the presence or absence of strong radio emission, the radio loudness.

1.3 A small gallery of radio and X-ray jets

In the previous section we got to know the engines of AGN activity. Now we want to have a look at their "creatures".

Jets are a very common and well studied phenomenon. They occur on very different scales and in various shapes, not only in AGN but also in many Galactic sources where a matter-accreting compact object is involved. This includes young stellar objects (YSOs) as well as nuclei of planetary nebulae, white dwarfs, neutron stars and galactic black holes. A review of galactic jets can be found in Mirabel & Rodríguez (1999). In this section we will focus on the radio and X-ray emission from extragalactic jets.

1.3.1 Kiloparsec–scale radio and X-ray jets

Radio jets on kpc–scale: An extended radio source is typically dominated by the emission from two distinct regions, the radio lobes, which are fed by two jets, emanating from the galactic nucleus. Cyg A (see Figure 1.5) is the standard example for this type of radio sources. The radio lobes extend typically some arcminutes on the sky (corresponding to several hundreds of kpc). The most extreme cases (giants radio galaxies) extend up to some Megaparsec, e.g. 3C 236. Based on their morphology, two separate classes of extended radio sources can be defined. The Fanaroff-Riley class I sources (FR I) exhibit lobes that become darker and smoother at their ends (edge darkening) and show no prominent hot spots. The FR II sources on the other hand have their brightest regions at the edges and exhibit strong hot spots. Both classes differ in more than just morphology. There is a sharp distinction in the radio luminosity at $5{\cdot}10^{25}\,\mathrm{W\,Hz^{-1}}$ with the FR I sources being less luminous. The steepest spectral indices, indicating optically thin radio emission (see section 2.2.2), occur always at the weaker regions of the lobes, at the edges of the FR I class objects and at inner regions at the FR II sources. The jets are usually less prominent in FR II sources and often seem to be one–sided, an effect of beaming (see 2.1.1) and reduced contrast due to the luminous lobes. The opening angle of the jets tends to be bigger in FR I sources, whereas the FR II jets are better collimated. Figure 1.4 shows some examples of extended radio sources and illustrates the differences between FR I and FR II sources. The physical difference between both classes is generally thought to be the power of the jet and the type of the flow in the jets. The transition may represent a change from a turbulent flow in FR I jets to a supersonic flow in FR II jets.

X-ray emission from jets: Before the launch of the CHANDRA X-ray observatory only a handful of radio galaxies were known to be associated with X-ray emission from the knots or hot spots of jets. Namely, only the jets in Cygnus A, M 87, 3C 120, 3C 390.3, 3C 273, NGC 6251, Pictor A and Mrk 266 were known to be X-ray sources. Additionally, the angular resolution was not sufficient to cross-correlate the detected X-ray jet features directly to the radio morphology. This situation has changed dramatically since July 23rd 1999, the launching day of CHANDRA. Right away the first reported shot at a celestial object, PKS 0637–752, revealed an X-ray jet (Schwartz et al. 2000). This detection was not even expected since PKS 0637-752 was chosen as a moderately strong point source for location of the focus and optical axis of the mirror. Numerous recent publications (see Harris & Krawczynski 2002 for a March 2001 list of jet-related X-ray emission) report about CHANDRA detections of extragalactic and galactic hot spots and other jet features. The 'classical', i.e. pre-CHANDRA X-ray jets have now been imaged in much more detail (see e.g. Figure 1.5). Many well-known radio jets, such as the ones in Cen A or 3C 295 have got their X-ray counterpart. CHANDRA offers the opportunity to study simultaneously the more extended X-ray emitting regions of the jet and the compact nuclear X-ray emission associated with the AGN.

The X-ray emission mechanism is nowadays the matter of hot tempered discussions. The four processes being discussed are:

- **Synchrotron emission from high energy electrons** – In this scenario the electron energies are either spread over a wide enough range to produce the whole emission all the way from the radio to the X-ray regime, or are separated in (at least) two distinct populations, a low energy one producing the radio synchrotron emission and a high energy one for the X-rays. The former possibility can be tested simply by looking at the spectral energy distribution (SED) of the emission. If the X-ray flux exceeds the extrapolated flux from the radio spectrum, using the spectral index of the radio data, this possibility can be excluded. However, the reverse argument is not true. Since the spectral index is expected to become steeper at high frequencies due to energy losses of the high energy electrons, this effect (spectral aging) can cause an overestimation of the X-ray flux by a simple extrapolation of the radio spectrum. If a distinct high energy population of electrons causes the X-ray

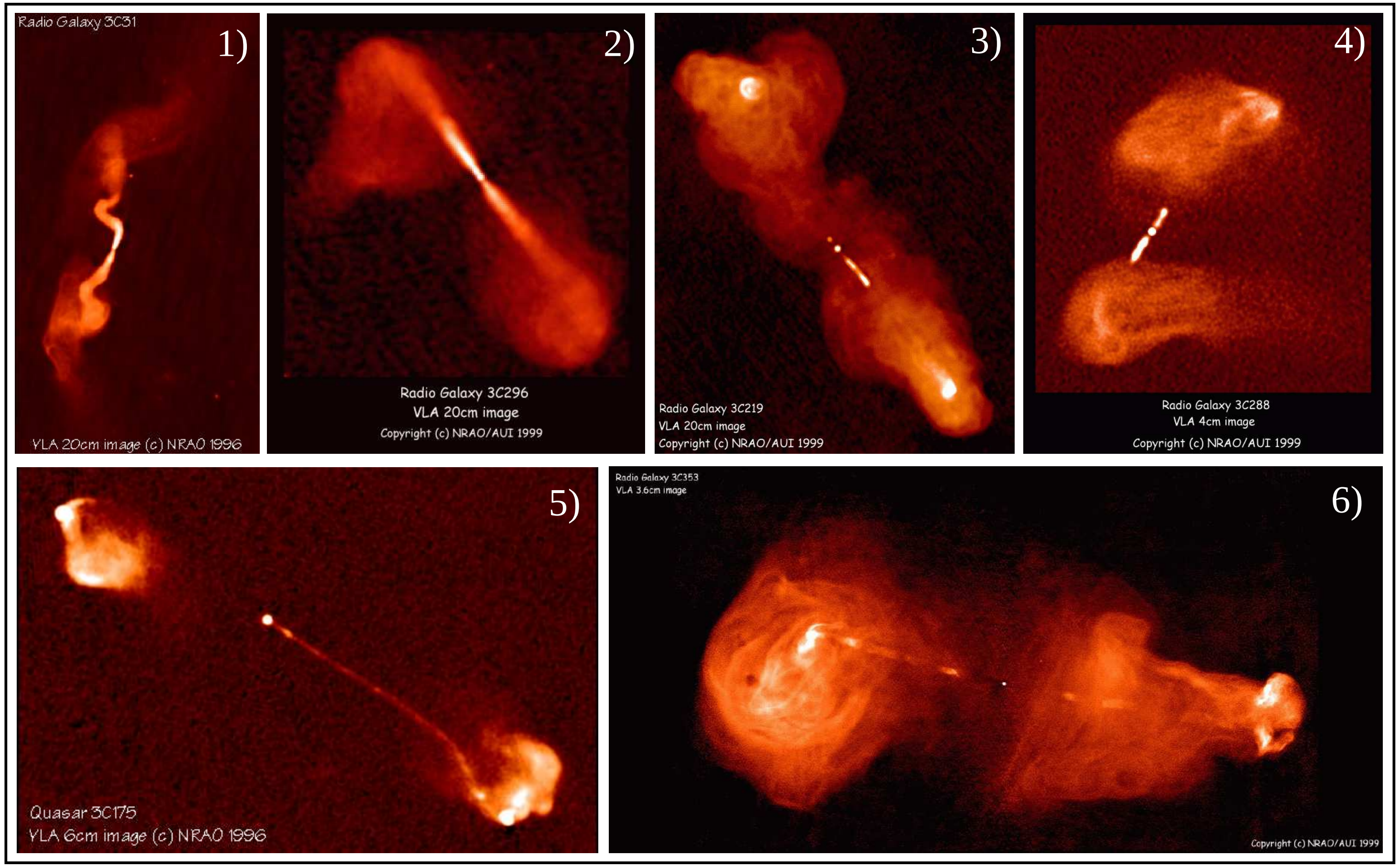

Figure 1.4: Six examples of jets imaged by the VLA (From top left to right bottom): 1) The FR I radio galaxy 3C 31 ($z = 0.0169$; resolution of $5\farcs5$ at 1.4 GHz) has a conical inner jet–counterjet structure and two larger, distorted plumes of emission. 2) 3C 296 is a FR I radio galaxy at z=0.0237 (1.45 GHz map with $4\farcs9$ resolution). 3) 3C 219, a FR II source at z=0.175. The image ($1\farcs4$ resolution, combination of two measurements at 1.4 and 1.6 GHz) shows bright and extended hot spots in both lobes, which extend several hundred kpc. 4) 3C 288, a radio galaxy at z=0.246 shows edge brightening but no prominent hot spots in this 8.4 GHz image ($0\farcs2$ resolution). 5) 3C 175 is a quasar at z=0.768. No counterjet emission is visible at this 4.9 GHz image ($0\farcs35$ resolution). 6) 3C 353 is a radio galaxy at z=0.03 with highly filamentary lobes at 8 GHz ($0\farcs44$ resolution). All images are taken from Alan Bridle's image gallery at the NRAO website.

emission, its mean energy has to be sufficiently higher to match the difference in emitting frequencies (assuming spatial coincidence, i.e. the same magnetic field, see Equation 2.6) and the acceleration event has to have happened more recently since the electrons have not cooled substantially. Single knots in M 87 (Wilson & Yang 2002) could be explained by this model.

- **Thermal emission** – In hot spots the ram pressure of the terminating jet can drive a shock into the surrounding gas. Applying shock jump conditions, it is then possible to estimate the density and temperature of the shocked gas. By comparison with a fitted thermal spectrum this model can be tested. Measurements of the rotation measure in the corresponding region lead to gas densities that can be compared to the predicted values, providing an additional check for thermal models. Hot plasma in an accretion flow could be responsible for the X-ray emission from unresolved cores (see section 2.4.5).

- **Synchrotron self Compton (SSC) emission** – This model has been successfully applied for example to the hot spots of Cygnus A (Harris et al. 1994) and will be described in section 2.3.3. Its main benefit in comparison with the other scenarios is that SSC emission has undoubtly to be produced, since we see the synchrotron emission, while its contribution to the total X-ray flux is not given *a-priori*. It has the problem that the derived values for the magnetic field are well below the equipartition limit (see 2.2.1) given by VLBI measurements of some sources. Note that the equipartition assumption is not given by basic physical principles but is a (well) working hypothesis.

- **External inverse Compton (EIC) scattering of cosmic microwave background photons** – EIC scattering is another process with an uncertain efficiency. In the rest frame of a relativistic jet the cosmic microwave background photons are beamed, enhancing their initially low energy density by a factor D^2 (see Equation 2.11), where D is the Doppler factor of the jet.

None of these processes can explain all observations. Only new observational data and more detailed spectra (as e.g. the X-ray Multi-Mirror Mission (XMM) promises to bring) will solve these questions.

1.3.2 Parsec–scale radio jets

With the development of VLBI (see 3.1) it became possible to resolve the compact radio cores observed in many radio galaxies, as e.g. Cygnus A. The resolution achieved in such experiments is typically about 1 milliarcsecond (mas) depending on the maximal baseline in the VLBI array and the observing frequency. VLBI observations showed that many of the compact radio cores are in fact pc–scale radio jets, apparently the innermost regions of the same jets, which reach out to kpc–scales and feed the lobes of radio galaxies. Additionally, many strong radio sources which show no structure on arcsecond–scales at all, typically quasars in the optical, also turned out to have jet–like morphologies on milliarcsecond–scales giving rise to unification models of radio galaxies and quasars (see 1.2.3).

As a bonus surprise many of these pc–scale jets showed very rapid structural variations. The motions of jet features sometimes appeared to be even faster than the speed of light.

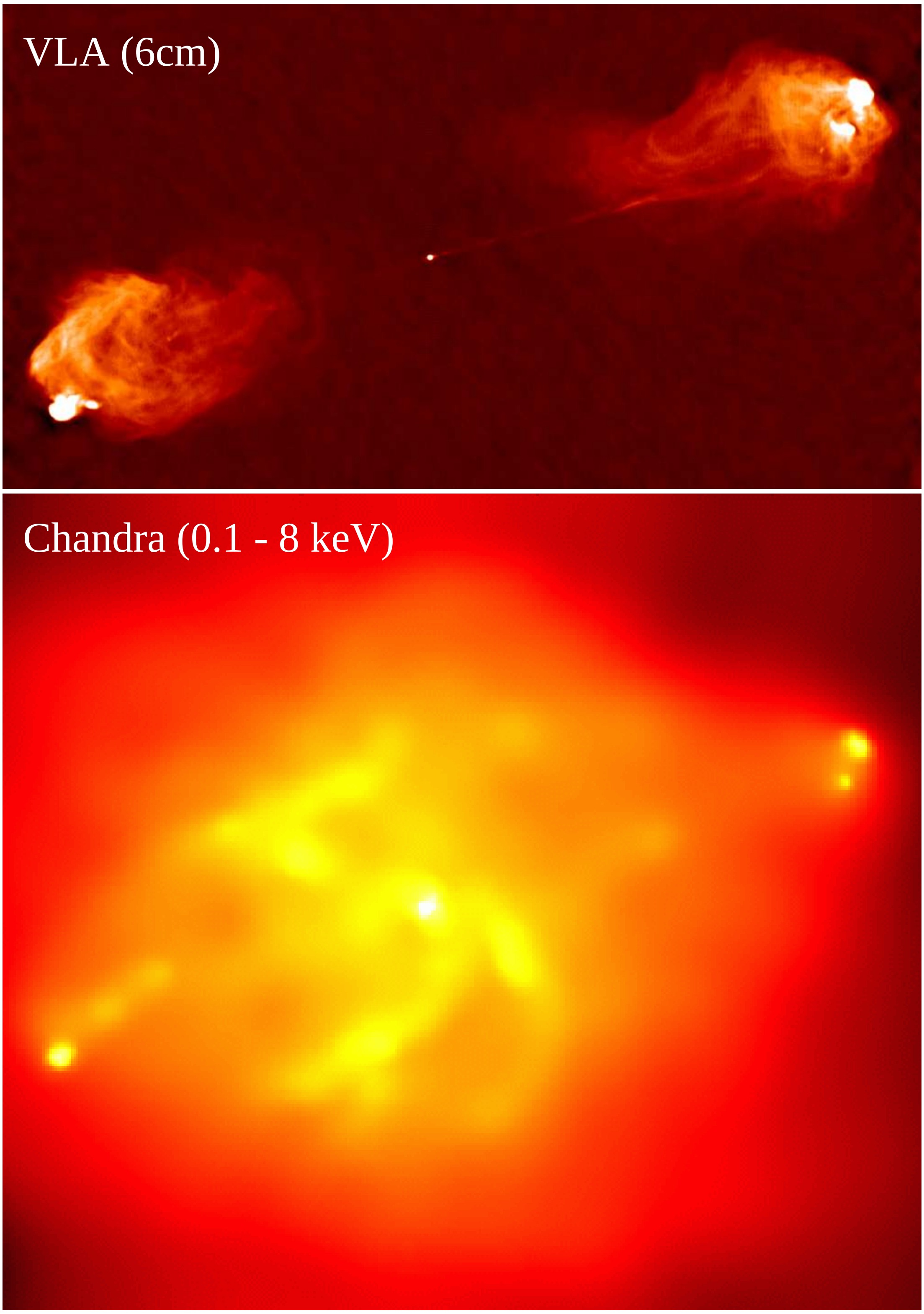

Figure 1.5: Cygnus A at radio and X-ray wavelengths. The upper panel shows a 6 cm ($8.4 \cdot 10^9$ Hz) VLA image (by courtesy of C. Carilli). The lower panel presents a 0.1-8 keV (2.4–$19.2 \cdot 10^{17}$ Hz) CHANDRA image (taken from `http://chandra.harvard.edu/photo/index.html`). Note the 8 orders of magnitude difference in frequency between both images. For a detailed discussion see Wilson et al. (2000), Young et al. (2002) and Smith et al. (2002).

This effect of 'superluminal motion' could be later explained by means of relativistic effects in a special geometry of jet and observer, when small angles to the line of sight and relativistic velocities are involved. During the time interval of the velocity measurement the moving component in the jet then nearly catches up with its own photons, and the measured time difference it takes the component to move perpendicularly to the line of sight appears to be shorter than it really is. The details of this effect can be found for example in (Krolik 1999, page 296).

In contrast to the classical doubles, the pc–scale jets are typically one–sided. The faster a source approaches the observer the stronger its radiation becomes magnified (see Equation 2.4) making the jet on pc–scales appear much brighter than the counterjet (relativistic beaming). These one–sided jets are overrepresented in flux density limited samples (as most surveys of extragalactic radio sources are) and so seem to be more common than their not magnified double–sided counterparts moving mainly in the plane of the sky (Doppler favoritism).

The compactness of some of these sources is proven by flux density variations on time scales of hours (intra day variability (IDV); see Wagner & Witzel 1995). About 30% of all compact flat spectrum sources do present IDV. At present it is not clear whether these variations are intrinsic or due to external scattering. In any case, very compact structures must cause the effect: either smaller than the scattering size of the interstellar medium or of the order of lighthours in size (by light travel time arguments).

Parsec-scale jets can be classified in two groups based on the shape of their radio spectra. Most of them, preferentially the one–sided jets, show nearly flat radio spectra (see Section 2.3.2). Some of the double–sided sources however, exhibit a peak, typically around a few GHz, with a steep decrease of the spectrum above the turnover frequency, similar to the spectra of lobes in radio galaxies. These sources are called GPS (Gigahertz peaked spectrum) sources. If the peak falls below the range of observing frequencies, the source is called a CSS (compact steep spectrum) source.

On this basis, a classification of extragalactic radio sources can be established as follows (adopted from Zensus 1997)

- Luminous core–dominated flat-spectrum sources
- Powerful double–lobed radio galaxies with hot spots (FR II sources)
- Weaker double–lobed radio galaxies without leading hot spots (FR I sources)
- Compact steep–spectrum sources (CSS sources)
- Compact symmetric objects smaller than 1 kpc (CSO sources)

An ongoing effort in studying the sub-milliarcsecond properties of a large sample of radio jets is done in the VLBA 2 cm survey. For this the Very Long Baseline Array (VLBA, see section 3.1.2) has been used since 1994 to image the structure of 171 strong compact sources at 15 GHz with a resolution better than 1 mas. Some images from the survey are shown in figure 1.6.

1.4 NGC 1052 – The star of the show

The main target of this thesis is an elliptical galaxy which has the number 1052 in the New General Catalogue of galaxies. The IAU (B1950.0) name is 0238−084. The Hubble type

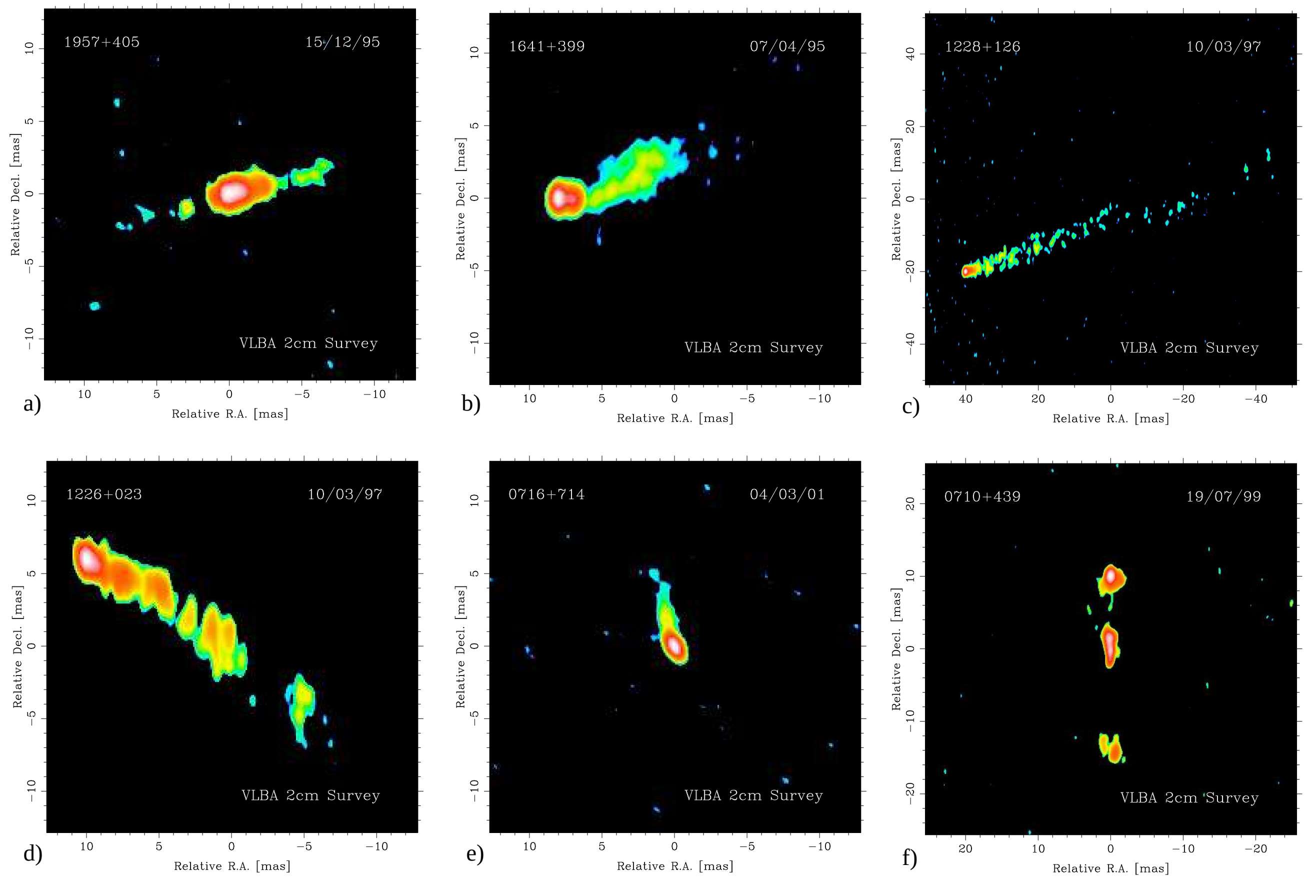

Figure 1.6: Six examples of pc- scale radio jets taken from the VLBA 2 cm survey (Kellermann et al. (1998), Zensus et al. (2002)); a) The core of the prototypical FR II radio galaxy Cygnus A (1957+405) shows a double–sided structure. At 2 cm it contributes less than 1% to the total luminosity of the source; b) The blazar 3C 345 exhibits two distinct regions in its pc–scale jet. At $\sim$ 3 mas distance from the core the well collimated jet with high turnover frequencies turns abruptly into a diffuse jet; c) The jet in M 87 has an apparent kink at about 45 mas from the core; d) 3C 273 was the first detected quasar. Its jet is prominent from radio to x-ray wavelengths; e) 0716+714 is an intra-day variable (IDV) source which shows variations in its flux density of up to 10% within a day. f) 0710+439 is an example of a CSO. Its hot spot advance speed suggests an dynamic age of only a few 1000 years.

of this 12th magnitude object is given as E3 (sometimes as E4). NGC 1052 is the central and dominant galaxy in a small group. Its redshift has been determined to be $z = 0.0049$ (Knapp et al. 1978) corresponding to a distance of 22.6 Mpc (assuming a Hubble constant of $H_0 = 65\,\mathrm{km\,s^{-1}\,Mpc^{-1}}$). This results to a linear scale of $0.11\,\mathrm{pc\,mas^{-1}}$. The proximity of NGC 1052 allows high resolution observations and provides the possibility of exploring relatively weak radiative processes, which would be overlooked in comparable sources at higher redshifts. Table 1.1 summarizes the basic data for NGC 1052.

Optical and infrared properties: The continuum emission in the optical is dominated by starlight with no obvious contribution of a non-thermal component. The optical spectrum of NGC 1052 was found very early (Mayall 1939) to show one of the strongest emission line spectra among elliptical galaxies, which is dominated by low ionization features. Fosbury et al. (1978) showed later that the emission line gas is composed of a luminous central component with a diameter $d \leq 220$ pc and an extended and more diffuse region of $d \sim 2$ kpc. The nuclear emission lines are narrow with very weak broad wings in the H_α line (Ho et al. 1997). NGC 1052 can be classified on a spectroscopic base as a Liner 1.9. Barth et al. (1999) found that the broad wings of the $H\alpha$ line are caused by a broad emission-line in polarized intensity, resembling the hidden type 1 spectra in luminous AGN. This detection is important for two reasons. First, it gives insight into the very vicinity of the putative black hole at the center of the galaxy predicting an obscuring torus which prevents us from seeing the broad line region directly but only in scattered (and thus polarized) emission. Second, it extends the unification scenario established for quasars and Seyfert galaxies to the low luminosity regime. NGC 1052 has a $H\alpha$ luminosity of $1.26 \cdot 10^{40}\mathrm{erg\ s^{-1}}$, well below the mean value of Seyfert galaxies or quasars.

NGC 1052 is known to have a faint dust lane along the minor axis of the optical ellipsoid (Gallagher 1986) and a central dark cloud towards the nucleus, both too faint to be directly visible in an optical image. Gabel et al. (2000) showed that the measured

Table 1.1: NGC 1052 parameters

Names	NGC 1052, 0238−084, 2E 642
Coordinates (J1950.0)	RA: 02 h 38 m 37.3537 s DEC: -08°28′09.″019[(a)]
Coordinates (J2000.0)	RA: 02 h 41 m 04.7984 s DEC: -08°15′20.″750[(a)]
Hubble type	E3/4
Spectroscopic type	LINER 1.9[(b)]
Redshift	0.0049[(c)]
Distance	22.6 Mpc[(d)]
Linear scale	1 mas$\hat{=}$0.11 pc[(d)]
Flux density at 1.4 GHz	1-1.5 Jy
Bolometric radio luminosity (1-100 GHz)	$4.4 \cdot 10^{40}\mathrm{erg\,s^{-1}}$[(e)]
Extended radio jet P.A.	$95° \pm 3°$ [(f)]
Parsec–scale jet P.A.	$63° \pm 6°$ [(g)]

[a] Johnston et al. (1995); [b]Ho et al. (1997); [c] Knapp et al. (1978); [d] assuming H_0=65 km s^{-1} Mpc^{-1}; [e] Wrobel 1984; [f] VLA, MERLIN at 1.4 GHz, Wrobel (1984) and this thesis; [g] Kellermann et al. (1998) and this thesis (the error corresponds to the frequency dependence of the P.A. on pc–scales; see chapter 3)

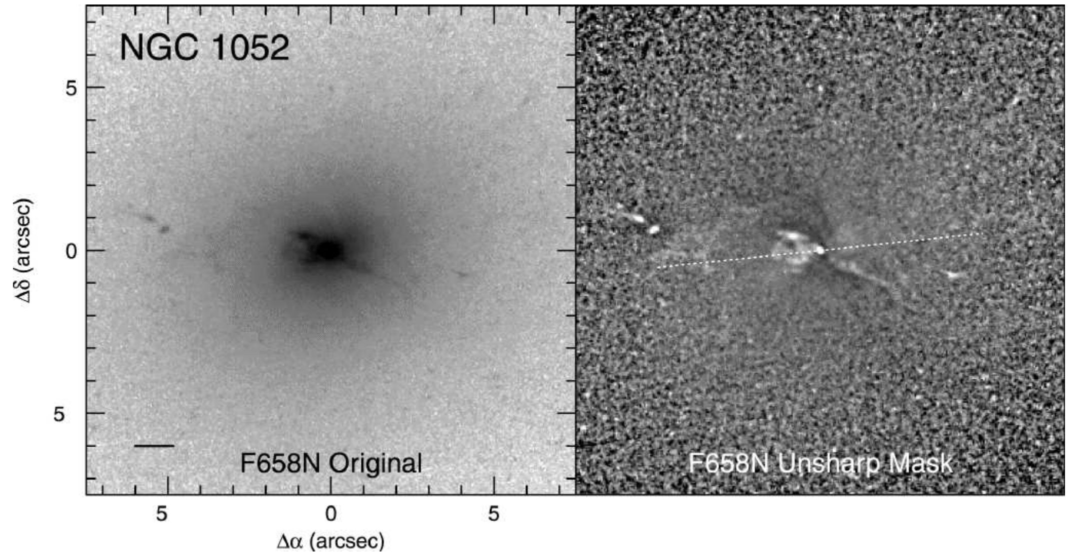

Figure 1.7: The emission cone in Hα of NGC 1052 and its optical jet. Left panel: Hα+ [NII] HST image without continuum subtraction. Right panel: Normalized unsharp masked, residual map of the same data. Absorption regions appear dark and emission bright. The dashed line indicates the axis of the radio jet on kpc–scales. Note the knots of emission, about $5''$ from the core on both sides. Taken from Pogge et al. (2000).

line ratios for Hα/Hβ indicate substantial reddening, with $E(B-V) = 0.42$. They derive that the emission line fluxes can be reproduced well by a simple photo-ionization model. In this model the central power-law ionization source has a spectral index of $\alpha = -1.2$ (flux density $S_\nu \propto \nu^{+\alpha}$) and can also be responsible for the weak high-ionization line system. The gas-covering factor determined from the observed flux distribution agrees with the idea that the line of sight towards the central engine could be obscured. Pogge et al. (2000) reported the presence of a collimated, conical structure in a HST Hα image (see Figure 1.7), probably the NGC 1052 analogon to the emission-line cones known from many Seyfert galaxies. Two knots of emission in the east of the core and one knot in the west indicate a jet-like structure associated with the cone (see Figure 1.7). Recent Keck telescope observations (Forbes et al. 2001) revealed the presence of two distinct globular cluster (GC) sub-populations in NGC 1052. The two populations differ in their color, with a blue and a red population indicating low and high metalicity, respectively. Such a bi-modality in the GC population of early-type galaxies seems to be quite common and suggests that these galaxies might be the product of a merger of two gas–rich spiral galaxies.

NGC 1052 exhibits an infrared excess in its spectrum (see e.g. Becklin et al. 1982), which could be attributed to the central $2''$. This indicates the presence of a dust component, heated by a central non-thermal source.

Radio properties: In the radio regime NGC 1052 is a moderately strong source with a luminosity (integrated between 1 and 100 GHz) of $\sim 4.4 \cdot 10^{40}$erg s^{-1} (Wrobel 1984). It shows a flat or slightly inverted spectrum with a broad peak around 10 GHz and an optically thin decrease in flux density above the peak (e.g. de Vries et al. 1997). The source is variable at all frequencies. At mm-wavelengths, time scales of months and amplitude variations between 0.5 and 2.5 Jy are observed (e.g. Heeschen & Puschell 1983). At longer wavelengths no continuous monitoring was done but different measurements indicate flux density variations of at least 50% with slightly longer time scales, several months to one year. Heeschen (1970) reported that ∼90% of the radio emission of NGC 1052 originates in a compact core ($< 1.5''$). The extended radio emission, distributed over $\sim 25''$, was imaged by Wrobel (1984) with the VLA at 1.4 and 1.6 GHz. Two lobes east and west of the nucleus contain ∼10% of the total flux density at these frequencies. Both lobes contain regions of enhanced surface brightness, similar to hot spots in more powerful radio galaxies.

Early VLBI observations (e.g. Jones et al. 1984) resolved the core into a nuclear jet with a position angle (P.A.) of $\sim 60°$, in contrast to the $\sim 95°$ P.A. of the extended structure seen in VLA maps. In later VLBI maps the pc–scale structure was found to represent a twin jet with an emission gap between the brighter eastern jet and the western jet (e.g. Kellermann et al. 1998). Exploring the origin of this emission gap is one of the main goals of this thesis. The kinematics of both jets at 2 cm have been investigated by Vermeulen et al. (2002). Observations between 1995 and 2001 show outward motions on both sides of the gap with similar velocities around 0.6 to 0.7 mas yr^{-1} corresponding to $\sim 0.25\,c$. The jets seem to be oriented close to the plane of the sky in order to explain the absence of strong velocity differences due to the Doppler effect. Although the two jets are bent, the trajectories of moving components do not differ significantly from ballistic motion. Kellermann et al. (1999) found free-free absorption towards the western jet, performing multifrequency observations between 0.7 and 21 cm. Kameno et al. (2001) suggested the presence of a pc–scale plasma torus, obscuring the core region of the western jet, from the analysis of multifrequency observations at 2.3, 8.4 and 15.4 GHz. They derived a geometry in which 0.1 pc of the eastern jet and 0.7 pc of the western jet are covered by this torus. Besides this ionized (free-free absorbing) gas component there is also evidence for atomic and molecular gas in the central region of NGC 1052. Claussen et al. (1998) detected H_2O maser emission towards the core of the western jet within the same region which is heavily affected by free-free absorption. The maser spots are ordered in two groups along the jet, rather than perpendicularly to it (like in NGC 4258). The maser line is redshifted with respect to the systemic velocity (see Braatz et al. 1996) corresponding to 100–150 km s^{-1}. It is unusually broad ($\sim$ 90 km s^{-1}) and smooth (i.e. not resolved into narrow components). The line varies significantly in shape and velocity with time scales of months. The maser spots seem not to trace a Keplerian disk around the nucleus but show a trend of higher velocities closer to the core. The nature of this maser emission is presently unclear. The masers could originate in the very vicinity of the jet, which is expected to interact strongly with the material in the obscuring torus. Alternatively, they could be the product of an amplification process in a molecular cloud in foreground to the jet (but still within the galaxy or maybe even the torus).

Atomic hydrogen is known to exist in NGC 1052 on various scales. HI in emission was imaged e.g. by Fosbury et al. (1978). Van Gorkom et al. (1986) mapped the distribution of the HI gas with a resolution of $1''$ with the VLA. They report a structure three times the size of the optical galaxy, with an orientation roughly perpendicular to its major axis. The distortion of symmetry in this distribution indicates a recent merger, possibly the same event in that the elliptical galaxy captured the gas. HI absorption is seen against the radio source at the systemic velocity as well as at redshifted velocities. On large scales the gas seems to be ordered in a rotating disk. Recent VLBI observations resolved the HI absorption features towards the nuclear jet (Vermeulen et al. 2002). Different features of a few percent depth can be seen towards the eastern jet. At present it is unclear

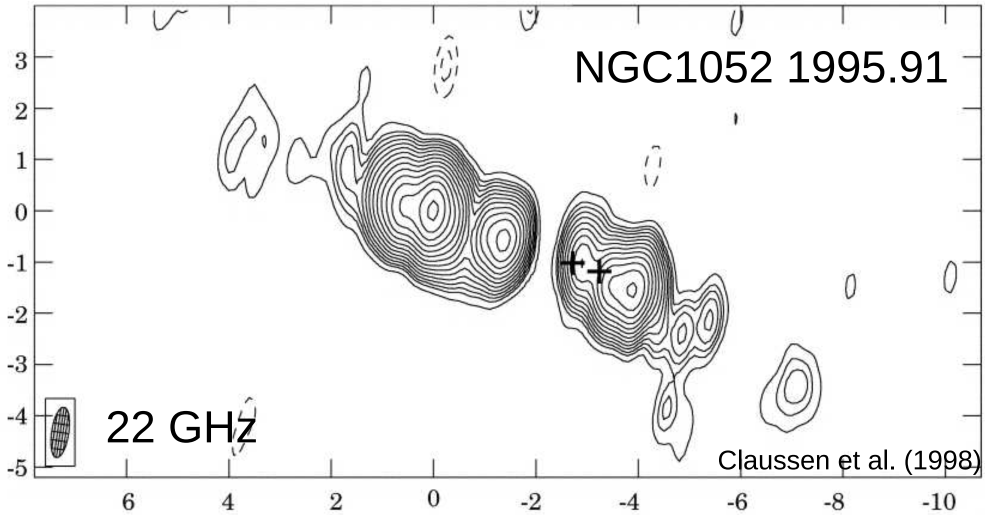

Figure 1.8: The pc–scale twin jet in NGC 1052 at 22 GHz. The contours are -2.9, -1.5, 1.5, 2.9, 4.0, 5.6, 7.8, 10.8, 15.0, 20.8, 29.0, 40.0, 56.0, 78.0, 108.0, 150.9 and 208.0 mJy beam^{-1}. The beamsize is 1.0 $\times$ 0.33 mas at a P.A. of -9°. The two groups of water masers are indicated by the two crosses. Taken from Claussen et al. (1998).

whether there is also absorption towards the western jet, that was not seen due to a lack of sensitivity in these observations, as would be expected in the scenario of the western jet being the counterjet. The most prominent absorption feature occurs $\sim$1–1.5 pc east of the nucleus, interestingly at the same velocity as the maser emission on the other side. Finally, an OH absorption line was also detected by Omar et al. (2002) using the VLA. Future VLBI observations have to explore the distribution of the OH gas on pc–scales.

X-ray properties: NGC 1052 has been detected in X-rays from the satellites Einstein (McDowell 1994), ASCA and ROSAT (Weaver et al. 1999, Guainazzi & Antonelli 1999), Beppo Sax (Guainazzi et al. 2000) and CHANDRA (this thesis). The spectrum of NGC 1052 between 0.1 and 10 keV is very flat (photon index[4] $\Gamma = 0.2 - 1.7$ depending on the applied model) and cannot be modeled with a simple power-law or thermal model. A high column density of absorbing material is needed to model-fit the data. Weaver et al. (1999) derive that the intrinsic spectrum is best described by a power–law that is either (1) attenuated by a two component absorber with $n_{\rm H} = 3 \cdot 10^{23}\,\rm cm^{-2}$ and $n_{\rm H} = 3 - 5 \cdot 10^{22}\,\rm cm^{-2}$, respectively or (2) Compton-reflected by a high density ($n_{\rm H} > 10^{24}\,\rm cm^{-2}$) medium that blocks the direct view to the nuclear source. They calculate 2-10 keV luminosities of $L_{\rm X} = 8 \cdot 10^{41}\,\rm erg\,s^{-1}$ and $L_{\rm X} = 2 \cdot 10^{43}\rm erg\,s^{-1}$ for the two models, respectively. Guainazzi & Antonelli (1999) derived similar models and pointed out that the radial profile of NGC 1052 taken with the HRI camera on board of the ROSAT satellite is not compatible with a point source with an extension going out to 100 arcsec. The broadband spectrum between 0.1 and 100 keV taken with Beppo Sax (Guainazzi et al.

[4]X-ray spectra are usually given in units like photons per keV: $P_{\rm E}(\text{photons s}^{-1}\,\text{keV}^{-1}) \propto \nu^{-\Gamma}$. Γ is called the photon index. Radio flux densities, on the other hand, are given in energy per unit frequency: $S_\nu \propto P_{\rm E} \times {\rm h}\nu \propto \nu^{-\Gamma+1} \propto \nu^{\alpha}$. The relation between the spectral index α and the photon index is therefore $\Gamma = 1 - \alpha$. To clearly distinguish between both power–law indices, α is sometimes referred to as the energy index.

2000) also yields a high column density and a flat spectrum ($n_H = 2 \cdot 10^{23}\,\mathrm{cm}^{-2}$, $\Gamma = 1.4$ for their best model). These authors additionally argue that a thermal bremsstrahlung model can fit the data and that the X–ray luminosity could be due to an advection dominated accretion flow (ADAF).

Chapter 2

Theoretical background

In this chapter theoretical background necessary for the proper understanding of the following chapters is presented. In section 2.1 the basic principles of synchrotron emission are discussed and some fundamental equations for the description of a synchrotron emitting source are derived. Especially relativistic effects will be taken into account and a possible connection between radio and X-ray spectra is investigated, the SSC mechanism. Section 2.2 will deal with synchrotron emission from jets in special consideration of the frequency dependence of the jet-core location.

2.1 Synchrotron radiation

2.1.1 Emission mechanism

Whenever a charged particle passes a region with an electromagnetic field it will interact with this field encountering the Lorentz force

$$\vec{F_L} = q\left(\vec{E} + \vec{\beta} \times \vec{B}\right) \tag{2.1}$$

with $\vec{\beta} = \vec{v}/c$, the velocity in units of the speed of light and q, the charge of the particle. In the case of a vanishing electric field ($\vec{E} = 0$) it will be accelerated perpendicularly to the magnetic field $\vec{B}$. For a linear magnetic field this will result in a helical motion around the direction of $\vec{B}$ as a superposition of a constant velocity component along the field and a constant acceleration perpendicular to it. It will orbit with a period $\gamma mc/2\pi qB$ corresponding to the Larmor frequency

$$\omega_B = \frac{qB}{\gamma mc} \tag{2.2}$$

with the Lorentz factor $\gamma = 1/\sqrt{1-\beta^2}$ and the mass m of the particle. In the non-relativistic case (Cyclotron radiation) the particle will emit an electromagnetic wave with this frequency. It can be shown that the emitted power for each electron energy is given by

$$P = 4/3\,\sigma_T\,c\,(\gamma\beta)^2\,U_B \propto \gamma^2 U_B \tag{2.3}$$

(Larmor formula, see Rybicki & Lightman 1979 for details), with $\sigma_T = 8\pi e^4/m^2c^4$, the Thomson cross section and $U_B = B^2/8\pi$, the magnetic field density. The dependence on

m^{-2} shows that in general the synchrotron emission from electrons will be much stronger than from protons ($m_p \sim 2 \cdot 10^3\, m_e$).

In the relativistic case of charges moving with a substantial fraction of the speed of light there are two major effects which have to be taken into account:

- **Relativistic beaming:** The relativistic Doppler effect affects the observed flux density S_ν (arriving energy per unit area and unit frequency) from a source which moves relativistically with a component of velocity towards or away from the observer $\beta_{||}$ emitting the flux density S'_ν in the comoving frame (e.g. Rybicki & Lightman 1979).

$$S_\nu = D^3 S'_\nu \tag{2.4}$$

with the Doppler factor defined by

$$D = \frac{1}{\gamma(1 - \beta_{||} \cos \Theta)} \quad . \tag{2.5}$$

Although this dependence on the angle of the emitter velocity to the line of sight is reduced to $D^{2-\alpha}$ for a continuous jet with spectral index α, the amplification (or reduction) of an approaching (or receding) source can be dramatic. An intrinsically isotropically emitted radiation is beamed into a cone with the half opening angle $1/\gamma$ making its apparent luminosity strongly dependent on the angle it is viewed from.

- **The lighthouse effect:** The former effect implies that the radiation from a relativistically gyrating charge in a magnetic field can only be observed in a short pulse when (and if) the beaming cone of the moving charge on its way around the magnetic field line crosses the line of sight. A short calculation reveals the pulse to be of the length $\Delta T = \gamma^3 \omega_B \sin\alpha$. A Fourier analysis shows that a short pulse is always composed out of a wide range of frequencies up to $1/\Delta T$. For this reason, a charge which gyrates with a single discrete frequency around magnetic field line emits in a wide waveband around a characteristic frequency of

$$\nu_c = 1\,\mathrm{MHz} \cdot \gamma^2 \left(\frac{B}{1\,G}\right) \tag{2.6}$$

for a mean pitch angle of 30°.

2.1.2 Spectral distribution

In nature, there are usually ensembles of electrons, large numbers of particles with a certain energy distribution, involved in physical processes rather than single electrons of fixed energy. In the case of jets, it is usually assumed that this distribution corresponds to a power-law between two energy values E_1 and E_2.

$$N(\gamma)d\gamma = N_0 \cdot \gamma^{-s} d\gamma \tag{2.7}$$

An ensemble of electrons with a power-law energy distribution in the presence of a magnetic field emits a continuous spectrum of synchrotron radiation which has again the spectral shape of a power-law:

$$S_\nu \propto \nu^\alpha \quad . \tag{2.8}$$

Indeed this is the typical shape of many classes of radio sources[1]. In this case the energy distribution of the electrons in the source can be derived:

$$\alpha = \frac{1-s}{2} \quad \Rightarrow \quad s = 1 - 2\alpha \tag{2.9}$$

The radio lobes of Cygnus A, for example, show a spectral index α of ~ -0.8 indicating an energy distribution of $s = 2.6$. The spectrum of a synchrotron source can usually be described by a single power–law above a specific frequency ν_t. Below ν_t the spectrum typically falls of, which indicates the start of an absorption mechanism at lower frequencies. ν_t is called the turnover frequency. The next section describes the two most important absorption mechanisms with respect to AGN spectra.

2.1.3 The SSC mechanism

Based on the compactness of the features observed in extragalactic jets by VLBI (often unresolved at milliarcsecond–scales) and on the observation of intra–day variability, indicating emitting regions of the order of lightdays, there is evidence that Compton scattering processes are at work in AGN. It is rather an open question of whether this effect contributes a substantial fraction of the high energy emission (e.g. in the X-ray regime) observed in many sources (or are even the main contributor of such photons) or if these processes are negligible. There are other processes which can produce high energy photons, such as thermal bremsstrahlung of hot gas (possibly of an ADAF–like accretion flow), but there always have to be high energy photons originating in a Compton scattering event of lower energy photons at high energy particles.

The SSC (Synchrotron Self Compton) mechanism is the special case of inverse Compton scattering where synchrotron photons scatter off the very same electrons which produced them. 'Inverse' means that the radio photons gain energy in this event from the electrons and are upscattered to higher frequencies. In this model the inverse Compton spectrum should mimic the synchrotron spectrum in a different wavelength regime. Assuming a simple homogeneous sphere model for a component in a radio jet and deriving the jet parameters from VLBI observations it is possible to predict the SSC-scattered spectrum of the jet component. By adding up all the jet components (perhaps with a special consideration about the core component, for which a sphere is a poor approximation) a SSC-flux density can be obtained at every frequency to be compared with the measured flux density. The sum has to extend from the innermost component of a jet (depending on the considered frequency of the seed photons) out to the hot spots which will contribute a substantial fraction of the scattered flux in some cases.

It can be shown (e.g. Krolik 1999, section 9.2.1) that the luminosity of the inverse Compton radiation P_C relative to to the initial synchrotron luminosity P_S depends simply on the ratio of the energy density in the synchrotron photon field U_S and the magnetic field energy density U_B:

$$\frac{P_C}{P_S} = \frac{U_S}{U_B} \quad , \tag{2.10}$$

with $U_B = B^2/8\pi$. For a measured synchrotron flux density S_ν from a homogeneous

[1]With this definition of the spectral index α, negative values indicate a spectrum that falls towards higher frequencies. Sources with $-0.5 < \alpha < 0.5$ are usually called flat spectrum sources.

sphere with radius R the energy density of the photon field is

$$U_S = \frac{\text{Luminosity}}{\text{Proj.Area} \times \text{velocity}} = \frac{S_\nu \nu 4\pi D^2}{4\pi R^2 c} = S_\nu \cdot \nu \frac{1}{c}\frac{D^2}{R^2} \quad . \tag{2.11}$$

If S_ν, R and D are measured and B can be estimated (see Section 2.4.1 and 2.4.3), the Compton luminosity can be predicted and compared to the measurements.

The frequency of the inverse Compton scattered photons ν' simply depends on the frequency of the seed photons ν and the Lorentz factor γ_e of the electrons responsible for the scattering (e.g. Rybicki & Lightman 1979)

$$\nu' \sim \gamma_e^2 \nu \quad . \tag{2.12}$$

Thus, in order to produce X-ray emission of 1 keV ($\hat{=}2.4 \cdot 10^{17}$ Hz) from seed photons of 22 GHz, high energy electrons with Lorentz factors $\gamma_e = 1600$ are needed. Since these are the same electrons which produce the seed photons, the inverse Compton spectrum will be a "high energy reflection" of the initial synchrotron spectrum. A more detailed calculation of the spectrum can be found in Rybicki & Lightman (1979).

2.2 Jets

In chapter 1.2 a pure phenomenological description of extragalactic radio jets was given, with the emphasis on the morphology and the huge range in astronomical scales on which jets arise. In this section the underlying physics of the jet phenomenon shall be discussed in more detail, although many things will only be superficially presented. Not every aspect of jet theory is completely understood at present, especially how jets are formed and accelerated.

The black hole paradigm is generally accepted at present to explain the enormous amounts of energy liberated on small scales. For this, it seems quite natural to search for a principle that permits the ejection of matter perpendicular to the accretion disk feeding the black hole. The ejecta have to contain high energy electrons and/or positrons, since the radiation of jets is convincingly ascribed to synchrotron radiation which predicts magnetic fields to be involved. A strong interaction with the circumnuclear medium is expected, since the matter density in the vicinity of a black hole has to be substantial. At the base of a jet absorption effects are expected, first due to self absorption of the jet radiation and second due to free-free absorption of the circumnuclear medium. This section shall throw light on those aspects of jet physics, used in later chapters of the work.

2.2.1 Jet formation and propagation

Astrophysical jets always seem to be associated with black holes, or more general, a very compact object, which appears to be the prerequisite of jet formation. The most plausible theory of jet formation deals with the formation of a toroidal magnetic field, building a channel for charged particles due to electromagnetic interaction. If this picture were true, human–built particle accelerators on earth would just pattern themselves on active galactic nuclei in forming a collimated beam of charged particles in toroidal electromagnetic fields. The basic idea how these toroidal magnetic fields could be formed in AGN is that the footpoints of existing magnetic field lines in an accretion disk should be frozen in the rotating matter. As the matter is compressed in the accretion process the magnetic field densities should increase and the field lines should be wound up as their footpoints rotate around the disk axis.

Other mechanisms could also lead to an acceleration and collimation of particles away from a compact and very active region as gas pressure or radiative forces. A more detailed review of theories on jet formation can be found for example in Krolik (1999).

As a basis for further discussion the following picture shall be taken as a paradigm for the innermost region of a jet: Substantial particle acceleration takes place in the very vicinity of an accretion disk. The accelerated particles are collimated by magnetohydrodynamic forces and guided along a channel outwards the central region in both directions perpendicular to the disk. At a distance r_N a nozzle is formed and the jet flow becomes supersonic. Beyond this point the particles are (re–)accelerated by the conversion of bulk kinetic energy to internal particle energy γ_e, e.g. via shock formation, resulting in a particle energy distribution represented by a power law

$$N(\gamma_e) = N_0 \gamma_e^{-s} \quad , \tag{2.13}$$

within a range $[\gamma_1, \gamma_2]$ of Lorentz factors. The jet is confined by an ambient medium with steep pressure and density gradients along the jet axis. Its hydrodynamics are given by a stationary adiabatic flow satisfying Bernoulli's equation $(\vec{v} \cdot \nabla)\gamma_j p^{1/4} = 0$ (Daly & Marscher 1988) with p, the pressure of the flow. This implies that the opening angle and the jet Lorentz factor should vary in presence of pressure gradients of the ambient medium. Nevertheless, the jet geometry can be approximated by a conical expansion, with a transverse radius $R \propto r$ with a opening angle $\Phi = \arctan(R/r)$.

Often it is assumed that the kinetic energy density of the jet (carried by electrons and protons) is in equipartition with the magnetic energy density

$$U_{e+p} = k \cdot U_B, \quad \text{with} \quad k \lesssim 1 \tag{2.14}$$

with $U_B = B^2/8\pi$. Under this assumption it is possible to integrate over the particle density distribution from γ_1 to γ_2 to derive the total density n of relativistic particles in the jet. A detailed calculation (e.g. Falcke & Biermann 1995) predicts

$$B \propto r^{-1} \quad \text{and} \quad n \propto r^{-2} \tag{2.15}$$

for the equipartition case. As another conclusion of the equipartition assumption it is possible to quantify the constant of proportionality in equation (2.8):

$$S_\nu = \frac{840 \cdot k}{\ln(\gamma_2/\gamma_1)} \mathrm{Jy} \left(\frac{B}{\mathrm{mG}}\right)^{3.5} \left(\frac{R}{\mathrm{kpc}}\right)^3 \left(\frac{D}{\mathrm{Gpc}}\right)^{-2} \left(\frac{\nu}{\mathrm{GHz}}\right)^{-\frac{1}{2}} \tag{2.16}$$

for $s = 2$ (power law index of the particle energy distribution) and

$$S_\nu = \frac{840 \cdot k(s-2)}{(\gamma_1^{2-s} - \gamma_2^{2-s})} \mathrm{Jy} \left(\frac{B}{\mathrm{mG}}\right)^{3.5} \left(\frac{R}{\mathrm{kpc}}\right)^3 \left(\frac{D}{\mathrm{Gpc}}\right)^{-2} \left(\frac{\nu}{\mathrm{GHz}}\right)^{\frac{1-s}{2}} \tag{2.17}$$

for $s \neq 2$. Thus, the flux density at the frequency ν of a spherical synchrotron source with the radius R and the distance D is determined mainly by the magnetic field and the energy index and range of Lorentz factors in the particle population.

2.2.2 Jet emission

According to the jet model described in 2.2.1 and the theory of synchrotron radiation a jet can be represented as the sum of many infinite thin slices forming the jet cone, each emitting synchrotron radiation determined through the local magnetic field, the energy index and range of Lorentz factors of the particle population, the distance to the jet origin and the frequency. The sum should extend from an innermost slice where the optical depth $\tau_S = 1$ (see Section 2.4.3) to a farthest slice at the end of the jet. This situation applies to an observation with a telescope which has a poor resolution compared to the extend of the jet, i.e. where the jet appears unresolved. Equation (2.16) has to be integrated along the jet axis from $r_{\tau=1}$ to infinity in order to derive the whole jet spectrum. For this integration the volume of the emitting sphere in Equation (2.16) has to be replaced by $4\pi R^2 dr$, with $R = \sin\Phi r$ the radius of a slice at the distance r to the jet origin. After a small calculation one ends up with

$$S_{Jet} \propto \nu^{-0.5} r_{\tau=1}^{-0.5} \tag{2.18}$$

for $s = 2$. Once again assuming equipartition and neglecting external absorption it can be used that the $\tau = 1$ surface depends on the observing frequency as

$$r_{\tau=1} \propto \nu^{-1} \tag{2.19}$$

(but see Section 2.4.3 for a general expression) and the frequency dependence in the spectrum cancels out.

> **The interpretation of a jet as a series of synchrotron emitting slices naturally leads to a flat spectrum!**

Deviation of flatness can be attributed to changes in the particle energy distribution along the jet, for example particle acceleration, bulk acceleration or a non–conical geometry.

2.2.3 The core–shift

Images of pc–scale jets obtained with Very Long Baseline Interferometry often show a feature with the following properties:

- Very compact or even unresolved on milliarcsecond scales
- Relatively bright, i.e. contributing a substantial fraction to the total flux
- In one–sided jets typically at one end of the linear structure
- Flat spectrum

A feature that has at least the first two properties is usually called the core of the jet. This term is quite misleading as it should not be identified with the central engine but with the part of the jet where it becomes visible. The innermost part of a jet is always invisible due to synchrotron self–absorption, since the optical depth τ of the jet at this part is very high. Traveling outwards the optical depth decreases due to the transversal expansion of the jet. The core is the part of the jet where $\tau \sim 1$ is reached. The optical depth due to self–absorption τ_s depends on the observing frequency and so does the core position. For this reason it is often not correct to align VLBI maps at different frequencies by matching the position of the strongest component. One has to account for possible frequency-dependent shifts of optically thick features like a jet-core. An examination of the component spectra is required as optically thin features are much better candidates for footpoints of frequency independent regions.

With this definition of a core, it is obvious that a double–sided source as NGC 1052 should have two cores, one for each jet. Both cores are expected at the innermost part of the corresponding jet with the true origin of the jet activity somewhere in between.

In general a jet becomes visible at the distance r_c from the central engine where the optical depth due to synchrotron self–absorption and external absorption $\tau = \tau_s + \tau_f = 1$. If both sides are affected asymmetrically by external absorption, as it is implied by the standard model, in a disk or torus around the central engine, the optical depth on each side is altered correspondingly and the cores appear at different distances from the central engine. These different distances contain information about the different contributions of external absorption. Additionally, the optical depth due to free-free absorption τ_f depends differently on frequency than τ_s does. So, an analysis of the core shift with frequency can further constrain the influences of external absorption on both jets.

NGC 1052 is a prime object for such a kind of analysis, because both jets are still visible at the highest frequencies and so, the high resolution gives a very good estimate of the central engine position. It is possible to deal with absolute core shifts with frequency rather than relative changes as in one–sided jets.

Synchrotron self–absorption and pressure gradients: An expanding jet, confined by a medium with pressure p can be described by its opening angle $\Phi = \arctan(R/r)$ and the magnetic field B and the particle density N in the jet, with

$$B = B_1(r_1/r)^m, \quad N = N_1(r_1/r)^n \tag{2.20}$$

where R is the diameter of the jet at distance r and B_1 and N_1 are the magnetic field and the particle density at $r_1 = 1\,\mathrm{pc}$. The optical depth due to synchrotron self–absorption τ_s is (e.g. Rybicki & Lightman 1979)

$$\tau_s(r) = C(\alpha) N_1 \left(\frac{e\delta B_1}{2\pi m_e}\right)^{\epsilon} \frac{\Phi_0}{r^{\epsilon m+n-1}\nu^{\epsilon+1}} \tag{2.21}$$

where m_e is the electron mass, $\epsilon = 3/2 - \alpha$, $\Phi_0 = \Phi\csc(\theta)$ the observed opening angle, θ the viewing angle, r the distance from the central engine, ν the observing frequency and δ the Doppler factor. $C(\alpha)$ is described in Blumenthal & Gould (1970) and can be evaluated for every intrinsic spectral index α. If there is no contribution of external absorption, the core can be described by setting τ_s to 1. Equation (2.21) gives for the core position

$$r_c[\mathrm{pc}] = C_1 \cdot \nu^{-1/k_r} \tag{2.22}$$

with

$$C_1 = B_1^{k_b/k_r}(1+z)^{-1}[6.2 \cdot 10^{18} C(\alpha)\delta^{\epsilon} N_1 \Phi_0]^{1/(\epsilon+1)}. \tag{2.23}$$

Here $k_b = (3-2\alpha)/(5-2\alpha)$, and the core–shift is parameterized via

$$k_r = ((3-2\alpha)m + 2n - 2)/(5-2\alpha). \tag{2.24}$$

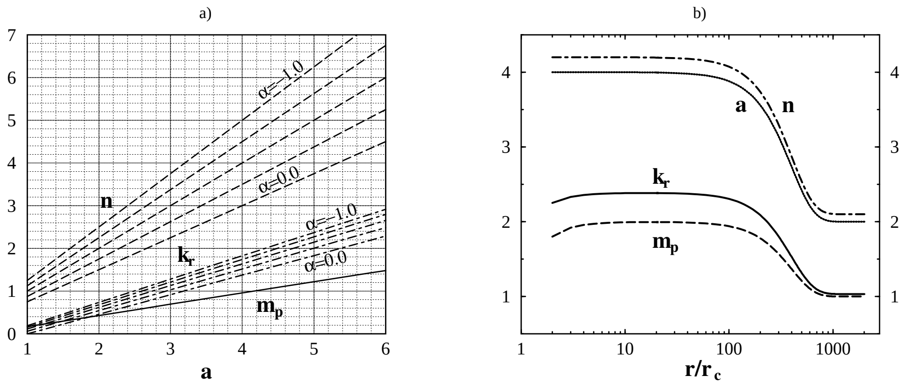

Figure 2.1: a) Dependence of n, m_p and k_r on pressure gradients. m is set to 1 and n and k_r are shown for different values of spectral index α. b) Change of the physical conditions along the jet axis, r. A spheric symmetrical exponential decrease of the pressure is assumed, $p(r) = p_0 \exp(-r^2/d^2)$. The medium extends to $400\,r_N$. k_r exhibits the largest deviations from its equipartition value of 1 at scales smaller than $100\,r_N$. Taken from Lobanov (1998).

Equation (2.22) predicts a linear relation between the logarithms of r_c and ν if m and n remain constant along the jet, i.e. if there are no pressure gradients. The slope of this relation is determined via Equation (2.24).

$$\log(r_c) \propto -\frac{1}{k_r} \cdot \log(\nu) \tag{2.25}$$

It can be shown (e.g. Falcke & Biermann 1995) that in the equipartition case $k_r = 1$. So, the task is to measure r_c at different frequencies and determine k_r via (2.24). Deviations from 1 then have to be attributed to pressure gradients in a confining medium. In the presence of steep pressure gradients, the Doppler factor and opening angle of the jet will vary in order to fulfill Bernoulli's equation and so will m and n (Georganopoulos & Marscher 1996) which determine the gradients of B and N, respectively. If the pressure varies as $p \propto r^{-a}$ then $m \to m_p = a/4m$ and $n = a(3-2\alpha)/4$. Figure 2.1 a (taken from Lobanov 1998) shows the dependence of magnetic field and particle density gradients on the pressure gradients of the ambient medium. In a more realistic model, the pressure density falls exponentially

$$p(r) = p_0 e^{-r^2/d^2}, \tag{2.26}$$

with a characteristic distance d from the central engine. This pressure gradient is more likely to be appropriate to model either a smooth medium like a torus or a cloudy one, maybe the same as the broad line region indicated by optical studies of AGN. In this case an approximation with a power–law is only useful with a variable power law index $a = a(r)$. Lobanov (1998) calculated the dependence of a, n, m_p and k_r along r in such a system with $d = 400 r_N$, $m = 2$ and $a(r_c) = 4$, with r_N the distance from the central engine to the location where the flow becomes supersonic (see Figure 2.1b). It is obvious that k_r does not exceed values of 2.5 for reasonable power–law indices a of the pressure. Higher values of k_r, i.e., smaller core shifts than $\propto \nu^{-0.4}$ can not be attributed to synchrotron self–absorption.

External absorption: The optical depth of a jet region can be altered from its intrinsic value due to synchrotron self–absorption if the foreground medium causes external absorption. This absorber can be located anywhere between the observer and the source but especially a circumnuclear medium, possibly with a disk-like or toroidal shape, can contribute significantly to the optical depth. In this case, one expects the medium to be ionized from the central source causing free-free absorption. In the general case $\tau = \tau_s + \tau_f$, with τ_f the optical depth due to free-free absorption.

Observations of Cyg A (Krichbaum et al. 1998), Cen A (Jones et al. 1996) and also NGC 1052 (Kellermann et al. 1999) suggest a free–free absorbing torus around the nucleus of an AGN perpendicular to the jet axis. If this is inclined by a moderate angle to the line of sight of the observer, the counterjet is obscured with the strongest absorption at its core. Depending on the geometry of the system, a smaller fraction of the jet can also be covered by the absorber if the torus extends sufficiently high above the accretion disk plane. Another possibility would be a cloudy medium like the broad line region (BLR) formed of hydrogen plasma clouds. The optical depth due to free-free absorption is given by (see Levinson et al. 1995)

$$\tau_f(r) = \int_L 5 \cdot 10^{16} T^{-1.5} \nu^{-2} \bar{g} n_e(r) n_i(r) dl \quad , \tag{2.27}$$

where L is the length of the absorbing path in units of pc and dl a line element along this path. T is the temperature of the absorber, n_e and n_i the electron and ion density, respectively, and $\bar{g}$ is the hydrogenic gaunt factor. The latter can be written as $\bar{g} \sim 5.99 \cdot T^{0.15} \nu^{-0.1}$ (e.g. Brown 1987). If we assume a pure hydrogen plasma and a power–law decrease of the density, we can set $n_e(r) = n_i(r) = n_0 r^{-n}$ and equation (2.27) becomes

$$\tau_f(r) \sim 30 \cdot 10^{16} \int_L T^{-1.35} \nu^{-2.1} n_0^2 r^{-2n} dl \tag{2.28}$$

In the scenario of an initially optically thin region of the jet, which becomes optically thick only due to free-free absorption, this expression has to be set to 1. In general, a special model has to be developed to solve for the dependence of r on l. To the first order, r can be set to be independent of l and $\int_L dl = L$. In this case $\tau_f \propto \nu^{-2.1} r^{-2n}$ and values of $n \leq 4$ (comparable to the ones used in the example in Figure 2.1) lead to

$$r_c \propto \nu^{-0.25} \Rightarrow k_r = 4, \tag{2.29}$$

a value much higher than possible without external absorption effects. In this simple model the value of k_r is a direct measure of the density gradient at the core position. The analysis of core–shifts in jets therefore is capable to distinguish between internal and external absorption, if the crucial parameter k_r is determined to a value larger than 2.5. The combination of spectral– and core–shift analysis can even constrain the density gradients of an external absorber or the confining medium of the jet, respectively.

Chapter 3

Observations and data reduction

The basis for this thesis are radio and X-ray observations of NGC 1052. The observations have been performed by three different instruments; the VLBA (Very Long Baseline Array), a telescope array of 10 antennas in the USA; MERLIN (Multi–Element Radio–Linked Interferometer Network), a connected array of telescopes in Great Britain; and the X-Ray satellite CHANDRA. The VLBA observations were planned and scheduled in 1998 by Dr. A. P. Lobanov, who provided the obtained data for the purpose of this diploma thesis. The MERLIN and CHANDRA data were obtained from public archives in the Internet. Since this thesis focuses mainly on the VLBA data, only these observations and the underlying principle will be discussed here. MERLIN and CHANDRA will be presented in Appendix B as well as an outline of the corresponding data reduction.

I will start with a brief introduction of Very Long Baseline Interferometry (VLBI), the observing technique of the VLBA. The VLBA data reduction will be discussed in Section 3.3 . Both sections will be kept brief, since VLBI and in general radio interferometry is discussed in more detail in many textbooks as e.g., Thompson et al. (1986).

3.1 Fundamentals of radio aperture synthesis

Figure 3.1 shows the geometry of a simple radio interferometer consisting of two antennas, pointed at a distant radio source. If the source is far enough (in the so called far-field-pattern), the incoming rays to the different interferometer elements can be assumed to be parallel. Each of the two antennas registers a signal that produces voltages V_1 and V_2 in the telescope backend. These voltages are eventually correlated, i.e., a circuitry performs a multiplication and averaging of the (converted) voltages[1]. If the source is, for simplicity, a monochromatic emitter, then V_1 and V_2 both are sinusoidal functions. Figure 3.1 shows that the cosmic signal reaches the first antenna at a time $\tau_g = (D/c)\cos\theta$ before it arrives at the second one, where D is the baseline of the two telescopes and c is the velocity of light. This is called the geometrical delay and the correlator output is proportional to

$$F = \sin(2\pi\nu t)\sin(2\pi\nu[t-\tau_g]) \quad . \tag{3.1}$$

[1]In contrast to the simple adding interferometer, which basically receives the quantity $(V_1 + V_2)^2$, the correlator interferometer is proportional only to the correlated component of the two signals. The uncorrelated components cancel out during the time averaging process. This leads to a substantial reduction of noise in the output.

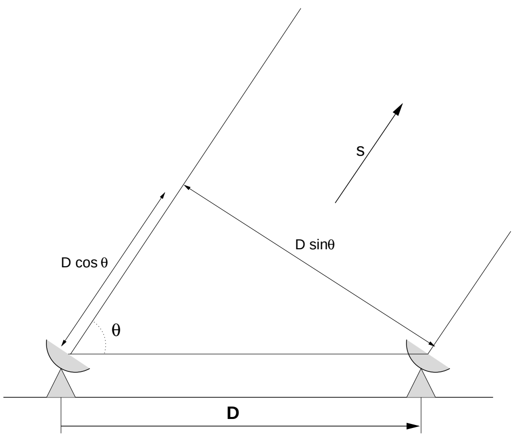

Figure 3.1: An elementary radio interferometer. Taken from Ros (1997).

Since the Earth rotates, the projected baseline $D\sin\theta$ varies with time and so does the geometrical delay. The terms independent of τ_g can be filtered out, leaving for the correlator output (after some trigonometrical transformations)

$$F = \cos\left(2\pi\nu\tau_\mathrm{g}\cos\theta\right) \quad . \tag{3.2}$$

Therefore, the correlator output is proportional to a quasi-sinusoidal fringe pattern[2], due to the rotation of the Earth. If the cosmic source is not a point source, but has extended structure, the interferometer receives the signal not only from the direction $\vec{s}$, where it is pointed at, but from a whole area around a nominal position $\vec{s}_0$. From the position $\vec{s} = \vec{s}_0 + \vec{\sigma}$, an element of solid angle $d\Omega$ of the source then contributes the power $1/2\Delta\nu B(\vec{\sigma})A(\vec{\sigma})d\Omega$ at each of the two antennas. $\Delta\nu$ is the observing bandwidth, $B(\vec{\sigma})$ is the brightness at position $\vec{\sigma}$, $A(\vec{\sigma})$ is the reception pattern of the antenna, and the factor 1/2 represents the capability of a telescope to receive only one direction of circular polarization. Correlating the two antenna output powers and applying the fringe term of Equation (3.2), the interferometer output becomes

$$\begin{aligned} r(\vec{D}_\lambda, \vec{S}_0) &= \Delta\nu \int_{4\pi} A(\vec{\sigma})B(\vec{\sigma})\cos(2\pi\vec{D}_\lambda\cdot\vec{s})d\Omega \\ &= \Delta\nu\cos(2\pi\vec{D}_\lambda\cdot\vec{s_0})\int_{4\pi} A(\vec{\sigma})B(\vec{\sigma})\cos(2\pi\vec{D}_\lambda\cdot\vec{\sigma})d\Omega \\ &- \Delta\nu\sin(2\pi\vec{D}_\lambda\cdot\vec{s_0})\int_{4\pi} A(\vec{\sigma})B(\vec{\sigma})\cos(2\pi\vec{D}_\lambda\cdot\vec{\sigma})d\Omega \end{aligned} \tag{3.3}$$

with $\nu\tau_\mathrm{g} = \vec{D}_\lambda\cdot\vec{s}$, where $\vec{D}_\lambda$ is the vector of the baseline in units of the observing wavelength. Introducing a complex quantity

$$V = |V|\mathrm{e}^{i\Phi_V} = \int_{4\pi} A_N(\vec{\sigma})B(\vec{\sigma})\mathrm{e}^{-i2\pi\vec{D}_\lambda\cdot\vec{\sigma}}d\Omega \tag{3.4}$$

[2]In reality a cosmic signal is never just composed out of one single frequency. The interference between different frequency components causes a modulation of the fringe function, which also depends on θ. This so called fringe-washing function has the shape of a sinc–function envelope, in the special case of a uniform power spectral density.

with a normalized reception pattern $A_N(\vec{\sigma}) = A(\vec{\sigma})/A_0$, where A_0 is the antenna collecting area in direction $\vec{s}_0$, the correlator output is

$$r(\vec{D}_\lambda, \vec{S}_0) = A_0 \Delta\nu |V| \cos(2\pi \vec{D}_\lambda \cdot \vec{s}_0 - \Phi_V) \quad . \tag{3.5}$$

V is called the complex visibility. The correlator output can be expressed in terms of a fringe pattern with the modulus and phase of V. The phase is measured relative to the phase of a hypothetical fringe pattern, received from a point source at the position $\vec{s}_0$. Both, modulus and phase of V are observables, and Equation (3.4) shows that the visibility is the Fourier transform of the brightness distribution $B(\vec{\sigma})$. In order to reconstruct B, the visibility V has to be measured with different baselines $\vec{D}_\lambda$. Usually this is expressed in terms of a two-dimensional plane with coordinates $u = \vec{D}_\lambda^{E/W} \cos\theta$ and $v = \vec{D}_\lambda^{N/S} \cos\theta$, which are basically the projected baselines in east–west and in north–south direction and are called spatial frequencies. This (u,v)–plane has to be sampled frequently enough in order to be able to perform a discrete Fourier transform[3] of the measured visibility function $V(u,v)$ and thus retrieve the brightness distribution B of the source with an angular resolution determined by the highest spatial frequency of the interferometer.

3.2 Observations of NGC 1052 with the VLBA

The VLBA is a dedicated VLBI array of ten antennas across the US. It was built to overcome some of the problems that early VLBI experiments suffered from, namely limited observing time, not optimized locations and difficulties in data calibration due to inhomogeneity of the different antennas. The longest baseline of the VLBA (about 8600 km) is between the western most antenna at Mauna Kea on Hawaii and the eastern most one at St. Croix on the Virgin Islands. The location of the 10 (nearly identical) antennas, each of 25 m in diameter, is shown in Figure 3.2. VLBA observations are possible between 21 cm and 0.35 mm wavelengths. The details of the VLBA design and technical properties are reviewed by Napier (1994).

NGC 1052 was observed on December 28th 1998 with all 10 antennas of the VLBA at four frequencies (5, 8.4, 22.2 and 43.2 GHz) in dual polarization mode. The data were recorded with a bit rate of 128 Mbps at 2-bit sampling providing a bandwidth of 16 MHz per polarization hand (divided in 2 blocks of 16 0.5 MHz channels each). The total integration time on NGC 1052 was about one hour at 5, 8.4, and 22.2 GHz each, and about six hours at 43.2 GHz, to compensate the lower array-sensitivity and the lower source flux density at this frequency. 3C 345 and 0237+28 were used as calibrators during the observation. A standard correlation was done at the Array Operations Center of the VLBA in Socorro NM, US, with an averaging time of two seconds and the data were distributed as a DAT tape. The performance of the array was very good during the observations. The Owens Valley antenna did not record data at 8.4 and 22.2 GHz. The high frequency data at 22.2 and 43.2 GHz suffered from some snow in the Brewster dish and rain at St. Croix.

[3]According to the sampling theorem a discrete Fourier transformation, as an approximation to a continuous Fourier transformation of an analytically given function, can be done, if the sampling frequency is at least twice the frequency of the highest spatial frequency.

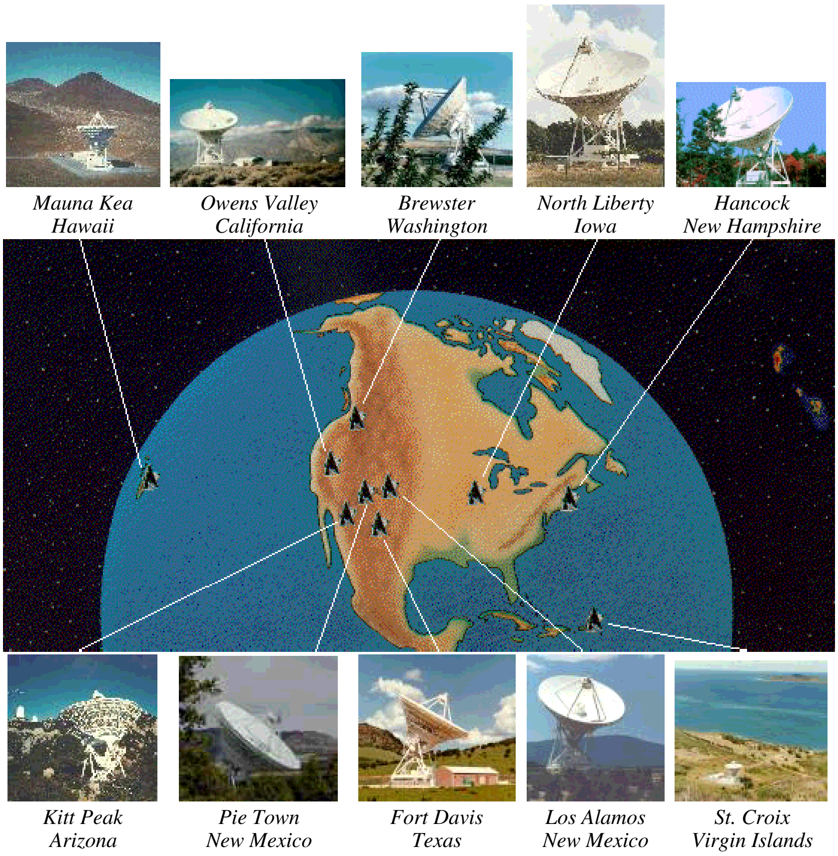

Figure 3.2: The antennas of the VLBA. Taken from the NRAO website (`http://www.nrao.edu`).

3.3 VLBI data reduction

VLBI data analysis requires a complex post-processing before the brightness distribution of the target source and its polarimetric properties can be obtained. This section describes the different steps of data reduction, performed to derive the astronomical information, discussed in chapter 4. The first part of the data reduction was done in $\mathcal{AIPS}$ (Astronomical Image Processing System; Fomalont 1981). After this *a–priori* calibration the visibility-data were exported and further processed in DIFMAP (Pearson et al. 1994). In this part, the brightness distribution of NGC 1052 was derived. From the information about the source structure in total intensity, the polarimetric properties of the source were obtained using $\mathcal{AIPS}$ routines. These three steps are described briefly as follows.

Pre–calibration data processing: Using the task FITLD the data were read from the VLBA correlator distribution tape into $\mathcal{AIPS}$. During this procedure, the visibilities with low weight in the correlation process (due to a poor signal to noise ratio (SNR) of the detected fringes) were flagged. The visibilities were sorted according to their baseline and time stamp order using the task MSORT. The task INDXR produces an index table which can be read in from other tasks in order to get a faster access to the visibilities of a special time and/or baseline.

As a reference antenna, with respect to whose fringes the phases are taken, LA (Los

Álamos) was chosen for all four frequencies since it had good data for the whole experiment and had also the benefit that it is located in the center of the array, providing both short and long baselines.

After this, the visibilities have to be examined carefully to get a "feeling" for the data quality and find bad data points to be flagged due, for example, to recording or bandpass problems at a single antenna. The task POSSM, e.g., allows one to plot the measured visibilities against frequency, divided by 16 channels in two frequency bands (IFs). Degraded data at the upper edge of both IFs, namely in channel 15 and 16, required the flagging of the corresponding data. The tasks VPLOT, UVPLT and SNPLT offered additional possibilities of data examination that will not be described here in detail.

The calibration of the data in $\mathcal{AIPS}$, described in the next paragraphs, is based on the following "philosophy": the data themselves are not modified during the calibration process. In each incremental step of data calibration, conversion factors are determined and stored in a separate file, called a solution table (SN). After the next calibration step a second SN table is produced and stored. The task CLCAL is used to produce a calibration table (CL) with the combined conversion factors, calculated from the two separate SN tables. In each additional calibration step a new SN table is produced and CLCAL calculates a new CL table from the previous one and the new SN table. Each SN table represents an individual calibration step and each CL table contains the combination of all the calibration steps performed so far. If it becomes necessary during the data calibration to flag single data points or regions of data, the corresponding information is stored in flag tables (FG). Only at the very end of the calibration process in $\mathcal{AIPS}$ the latest CL table and the most complete FG table are applied to the data. The benefit of this principle is that it is possible to redo a special calibration step without the need to throw away the solutions corresponding to the following calibration steps. So it is easy to correct errors that might have happened and are detected in a later stage of the data reduction.

A-priori **amplitude calibration:** In the first part of the data calibration the amplitudes of the visibility data points are corrected for instrumental effects. The visibility amplitudes can be expressed in terms of a correlation coefficient ρ, which is equal to one if the signals at the two telescopes are totally correlated, i.e., if they are identical, and which is equal to zero if the signals are totally uncorrelated. The case $\rho = 1$ corresponds to an idealized observation of a point source. A fully resolved, extended structure corresponds to ρ=0. The measured visibility V_{m} then can be expressed as

$$V_{\mathrm{m}} = \rho\, b \sqrt{\frac{T_{\mathrm{sys},i}}{T_{\mathrm{sys},j}} K_i K_j} \quad , \tag{3.6}$$

where b describes losses in the digitalization process of the signal. For dual-polarization observation data, the b factors can be determined from the amplitude offsets between the RR (the right hand polarization signal of the first antenna correlated with the right hand polarization signal of the second antenna) and LL (correlation of the left hand signals) visibilities. This is done with the task ACCOR, which produces a solution table (SN) with the necessary correcting factors. $T_{\mathrm{sys},i/j}$ are the system temperatures of the two telescopes and $K_{i/j}$ the corresponding sensitivities. Since the system temperature, the antenna sensitivities and the digitalization losses can be derived from calibration measurements of known sources, the correlation coefficient ρ and the "true" visibilities can be reconstructed. To do this in practice a so called radiometry file has to be produced, which contains the necessary antenna information. Two files containing the system temperatures and the gain curves (the elevation-dependent antenna sensitivities) were retrieved from the VLBA-observations archive[4]. The gain curves are contained in the file `vlba_gains.key`, which has to be edited, according to the epoch of the observation. The system temperatures are concatenated to the same file and from this radiometry file the information is read into a gain-curve table (GC) and a system temperature table (TY) in $\mathcal{AIPS}$ using the task ANTAB. The task APCAL produces from those a solution table (SN). The task CLCAL applies the correcting factors of the first SN table to the first CL table and produces a second calibration table (CL). A second run of CLCAL produces a third CL table containing the combined correction factors of both SN tables with the necessary corrections to get *a–priori* amplitude calibrated visibilities.

If at any step of the data reduction the examination of the data reveals bad regions of data, for example time ranges, channels or single points, the task UVFLG can be used to flag these data. The inspection of the system temperatures (task SNPLT) showed for example that one antenna had collected about one hour of data with unusually high system temperatures. This was due to a very low elevation of the target source. This region of data has been flagged for the corresponding frequency and the flagging information was written into a flag table (FG).

***A–priori* phase calibration:** Since the right circular polarization (RCP) and left circular polarization (LCP) feeds of an antenna rotate in position angle with respect to a source during an experiment (Earth rotation) this contribution to the phases had to be removed first (parallactic angle correction). For this purpose the task CLCOR was applied to a copy of the most recent CL table, since CLCOR directly affects the CL table entries.

The measured visibility phases are affected by instrumental offsets and slopes between and within the different frequency channel bands (IFs). These phase offsets and gradients are caused by the passage of the signal through the electronics of the VLBA baseband converters and can be determined from so called phase–cal signals that had been injected into the data stream during the data recording process. Appropriate corrections have to be applied to the data, to permit to average the visibilities over frequency and time. The phase-cal information can be read into $\mathcal{AIPS}$ from an external file using the task PCLOD, which produces a first phase-cal table (PC). The task PCCOR was used to calculate a SN table from the entries of the PC table for the four frequencies separately, that can be used to correct for the instrumental single-band phase and delay offsets. For this purpose a "good" scan was chosen, that contained a data point on a calibrator for every antenna and a corresponding entry in the PC table. This should solve for any 2π ambiguities. The phase rates were set to zero with task SNCOR and the resulting SN table was applied to the most recent CL table with CLCAL. After this calibration step the visibility phase as a function of frequency is smooth and shows no sharp jumps anymore.

Fringe fitting: After correcting the visibility phases for instrumental effects in the *a–priori* phase calibration, small residual phase errors remain in the data, due to propagation effects in the Earth/s atmosphere and inaccurate modeling of the geometry of the interferometer. This results in a phase gradient between the wavebands, measured as the

[4] `ftp://ftp.aspen.nrao.edu`

multi-band delay, in contrast to the single-band delay, that has been calibrated in the *a–priori* calibration. There are however, residual single-band delays that could not be removed in the *a–priori* phase calibration. The residual errors are larger at higher frequencies. Those can be inspected using the tasks POSSM (showing the visibility averaged in time as a function of frequency) and VPLOT (averaged in frequency as a function of time). Both rates were removed with the task FRING to make the data ready for averaging in time and frequency. The last CL and FG tables were specified to perform this task. LA (Los Álamos) was again chosen as the reference antenna and the sequence of the fringe fitting on the different baselines was specified, so that the fitting was done first on short baselines with high flux density and good SNR. This prevents the loss of data from a whole antenna if no solution is found at first instance. The two polarization hands were treated separately for each frequency. The time and frequency intervals that should be searched for fringes had to be specified as a compromise between a bad signal to noise ratio (with small windows) and the loss of coherence (with too big windows). The derived solutions can be checked for consistency using the task SNPLT and edited when necessary with the tasks SNSMO or SNEDT. Figure 3.3 shows the visibilities of a scan on NGC 1052 for a single baseline (Kitt Peak – North Liberty) as a function of frequency after the fringe fitting and shows that the data after this calibration are now ready for averaging. The amplitudes are smooth and the phases show no offsets or slopes.

The last CL table with the complete calibration information had finally to be applied

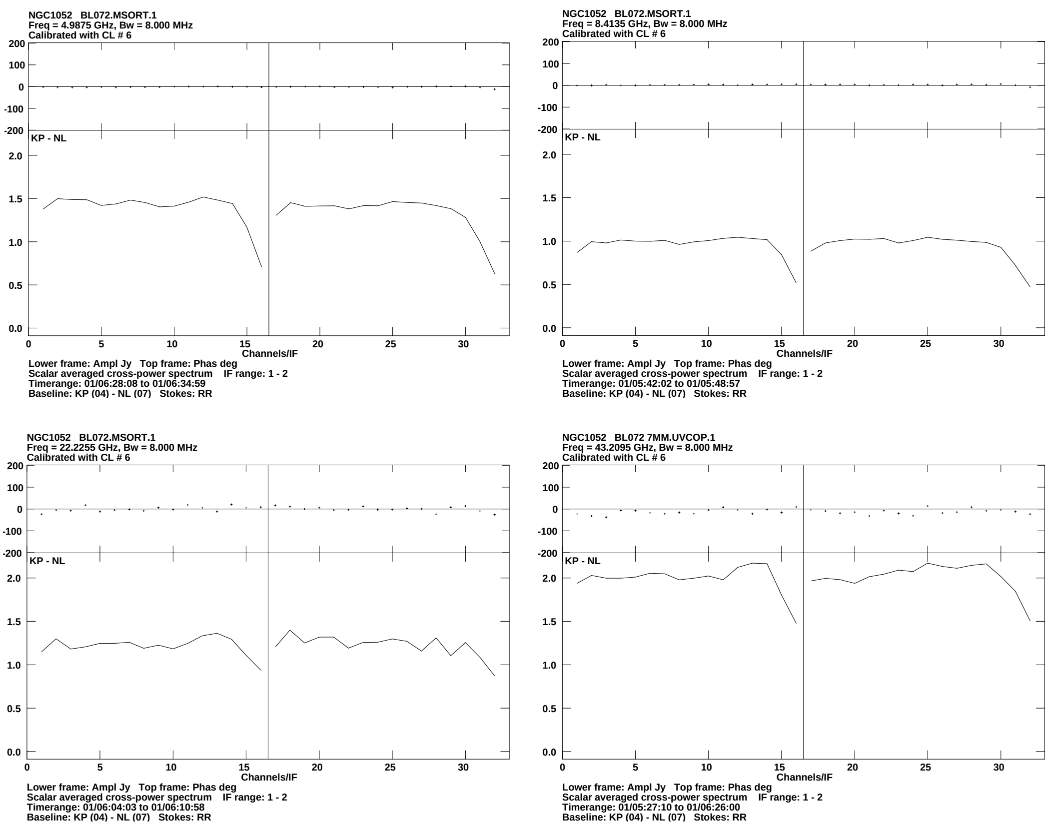

Figure 3.3: A POSSM plot of one scan on the baseline Kitt Peak – North Liberty for each of the four frequencies showing fringe-fitted data as a function of frequency.

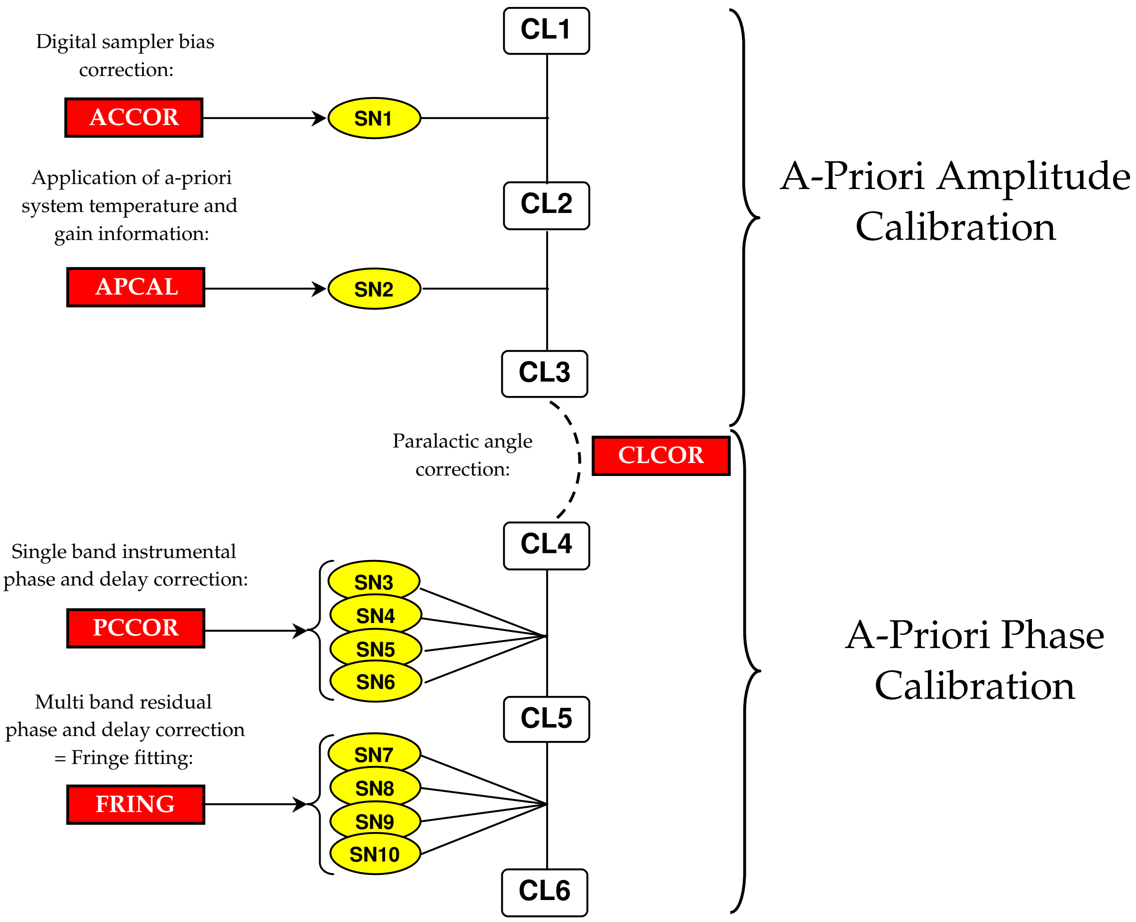

Figure 3.4: The basic path of data *a–priori* calibration in *AIPS*.

to the data using the task SPLIT. In this step a calibrated data set for each source at each frequency is produced and these data sets are exported from *AIPS*. Figure 3.4 summarizes the various calibration steps performed within *AIPS* in a flux diagram.

Data self–calibration and mapping the total intensity distribution: The data output from *AIPS* is in the FITS format (Wells et al. 1981) and can be read in by the program DIFMAP (Pearson et al. 1994), an interactively editing and mapping program. DIFMAP provides a variety of possibilities to plot and edit the (u, v)–data, yielding a more user-friendly access to the data than *AIPS*.

At this point the data are organized in one-source files for each frequency and in the case of full polarization data in different data streams for RCP and LCP. To map the total intensity the data stream 'I' has to be chosen. The commands UVPLOT and TPLOT provide information about the (u, v)–coverage and the time coverage of the observation. Examples for both are given in Figure 3.5 and 3.6 for the case of the 43 GHz data of NGC 1052. The structure of the measured visibilities as a function of time and (u, v)–distance can be examined with the commands RADPLOT, VPLOT and PROJPLOT.

The (u, v)–data have to be Fourier-transformed to derive the brightness distribution of NGC 1052 at the four frequencies. Since the two-dimensional visibility function is

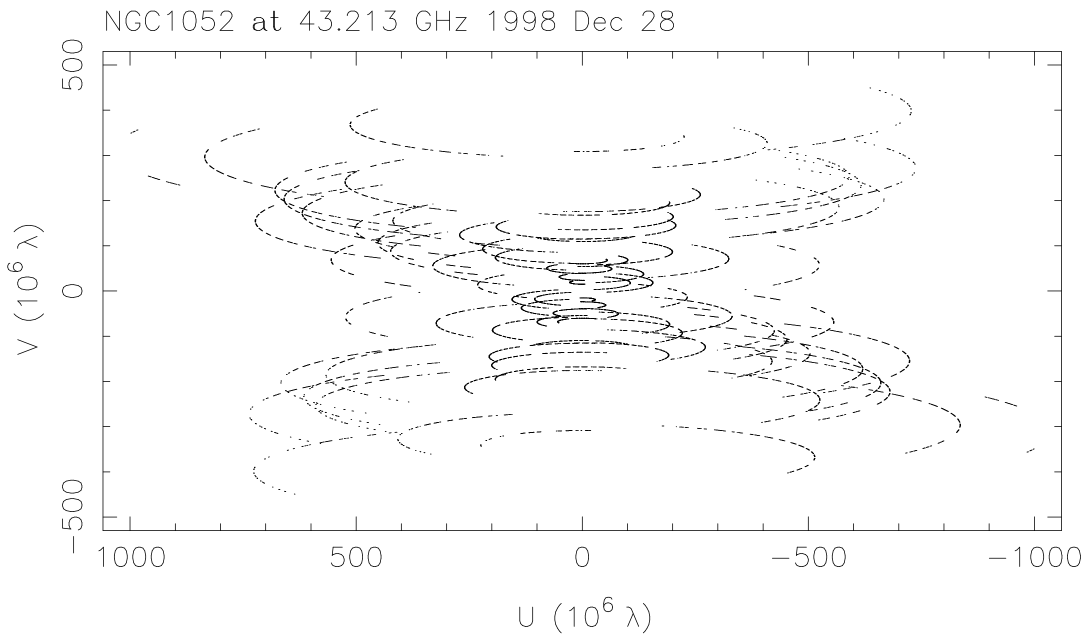

Figure 3.5: A (u,v)–plot, showing the location of baselines in the (u,v)–plane during the 43 GHz observation of NGC 1052

measured only at 45 points in the (u,v)–domain[5] during one integration bin, the discrete Fourier transform algorithm has to be used, to derive an approximation to the true Fourier transform of this function:

$$B'(x,y) = \sum_{j=1}^{M} V(u_j,v_j) \exp^{2\pi i(u_j x + v_j y)} \tag{3.7}$$

with

$$V(u_j,v_j) = V(u,v) \cdot w_j; \qquad w_j = \begin{cases} 1 & : \quad u = u_j, v = v_j \\ 0 & : \quad u \neq u_j, v \neq v_j \end{cases}$$

The result of this procedure is the "dirty map", which is the convolution of the true brightness distribution $B(x,y)$ with the reception pattern of the array, the "dirty beam". The "dirty beam" is composed of a central peak with the full width at half maximum (FWHM) of $(u_{max} \cdot v_{max})^{-1/2}$ and a number of weaker, local maxima, which are due to the imperfect sampling of the (u,v)–plane. The better the sampling is, the less prominent are these local maxima. Different algorithms have been developed to deconvolve the "dirty map", the CLEAN algorithm (Högbom 1983) being the most extended. In each step of this iterative algorithm a fraction (loop gain) of the "dirty beam", a CLEAN component, is subtracted from the "dirty map" at the position of its maximum. The position and flux of the CLEAN component is stored temporarily as well as the modified "dirty map", without the contribution of the CLEAN component, now called the residual map. In this residual map the new maximum is searched and another cycle of "cleaning" is applied. This algorithm should make the residual map smooth and featureless. In a final step, the temporary map that contains the CLEAN components has to be convolved

[5]A telescope array of N antennas provides $N(N-1)/2$ baselines. For the VLBA and its 10 antennas this results in 45 baselines.

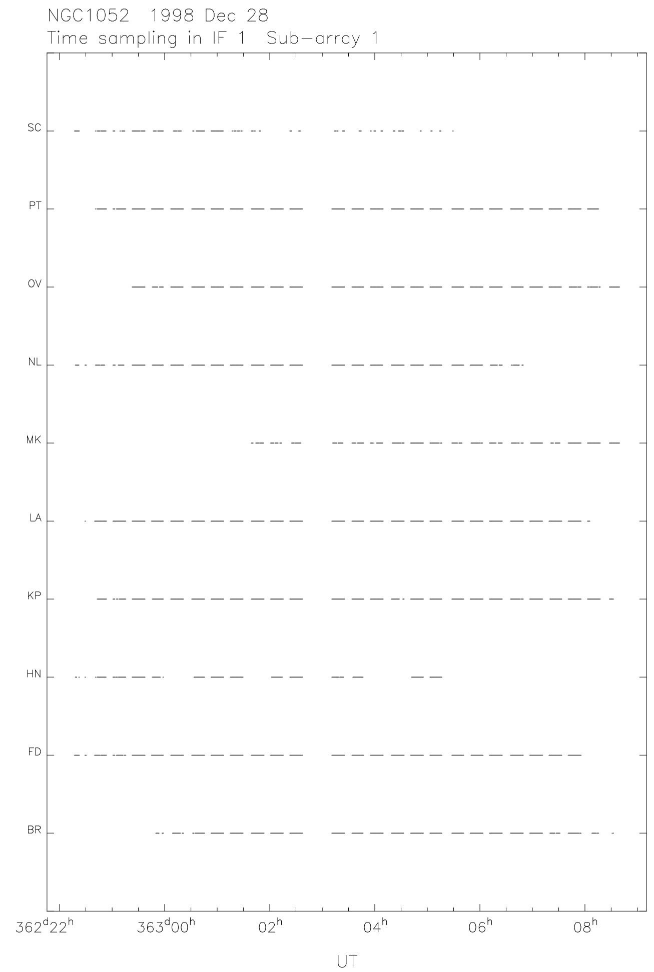

Figure 3.6: Time coverage of the NGC 1052 observation at 43 GHz.

with an idealized interferometer beam (equivalent to the diffraction pattern), which is a two-dimensional Gaussian function with the FWHM of the "dirty beam". The residual map is added to this "CLEAN map", resulting to a final map, which represents the true brightness distribution as approximated from the measurements. The choice of a loop gain smaller than one in each cycle ensures that no artificial effects arise in the "clean map".

The quality of the final map can be enhanced, using the self consistency of the data and the derived model, by self–calibration. Even after the *a–priori* calibration of the data in $\mathcal{AIPS}$, both the amplitudes and the phases of the visibilities are affected by errors. The measured phases can be written as

$$\Theta'_{i,j} = \Theta_{i,j} + \Phi_i - \Phi_j + \epsilon_{i,j} \quad , \tag{3.8}$$

with $\Theta_{i,j}$ the true phase, $\Phi_{i/j}$ an error contribution arising at station i and j, respectively, and a noise term ϵ. The influence of the station-dependent terms cancel out if the sum of three different stations are added up:

$$\Theta'_{i,j} + \Theta'_{i,k} + \Theta'_{j,k} = \Theta_{i,j} + \Theta_{i,k} + \Theta_{j,k} + \epsilon_{i,j} + \epsilon_{i,k} + \epsilon_{j,k} \tag{3.9}$$

This closure-phase relationship is used in the phase self calibration that can be applied between the subsequent CLEAN steps. The visibility phases are varied in order to best fit the derived model, keeping the closure phases constant.

The CLEAN algorithm is implemented in DIFMAP and can be applied with the command CLEAN N, L, where N is the number of CLEAN iterations to perform, each with a loop gain L. After a CLEAN cycle, phase self–calibration is applied with the command SELFCAL. When the iteration has converged, i.e., when the "cleaned" flux no longer increases and/or the residual map has become smooth and featureless, the derived model can be used to self–calibrate the visibility amplitudes. After this, the mapping process starts from the beginning, but now using the better calibrated data.

The (u, v)–data of NGC 1052 at the four frequencies have been mapped according to this strategy. After reading in the data, they were averaged into 30 second bins to accelerate the mapping process. The data were examined using the commands VPLOT, which shows the visibilities as a function of time for each baseline, and CPPLOT, which displays the closure phases for the various triangles of telescopes. Any obviously bad data points were flagged. Starting from a point source model the "dirty map" at each frequency was "cleaned" and the data were phase self–calibrated. In this first cycle each data point was given the same weight (natural weighting). This overemphasizes the short (u, v)–spacings, which are more frequently sampled in the (u, v)–plane and prevents one from loosing extended structures.

After obtaining a first good model, the data were amplitude self–calibrated for a first time with the command GSCALE. In this procedure time-independent gain factors for each antenna are determined, which increase the consistency between the data and the model. These factors are given in the output of GSCALE and should be small. For 5 and 8.4 GHz the performance was excellent, with correction factors not bigger than 2% with a mean of 0.9% and 0.6%, respectively. At 22 GHz the biggest correction of 4% was applied to the antenna at St. Croix and the mean correction was about 2%. At 43 GHz the antenna at Mauna Kea needed a rather big correction of 29% but the other antennas also had a remarkably good *a–priori* calibration at this very high frequency with correction-factors below 5%. Having this amplitude self–calibrated data set, the "cleaning" and phase self–calibration process was restarted from a point-source model. At the end of this second cycle a second amplitude self–calibration was performed with a time scale of 180 minutes. The time dependent correction factors were examined with the command CORPLOT.

In the following iterations the time scale was decreased further in 8 steps, down to a time scale of 1 minute. From the second cycle on, uniform weighting was chosen, which gives the weights in the (u, v)–plane according to the local density of data points. Uniform weighting gives the best angular resolution but reduces the sensitivity of the array. In the last cycle the amplitudes were allowed to vary freely and a fully amplitude and phase self–calibrated dataset was saved. From this the final map for each frequency was produced.

Figure 3.7 shows the visibilities of the 43 GHz observation of NGC 1052 as a function of time for the baseline Fort Davies to Pie Town at the beginning and at the end of the self–calibration process. In Figure 3.8 the final 5 GHz data set is plotted as a function of radial (u, v)–distance projected on two one dimensional slices along a position angle (P.A.) of 69° (parallel to the VLBI jet) and 159° (perpendicular to the axis of the VLBI jet), respectively. Along P.A.=69° the visibility shows fringes indicating at least two strong and interfering components. Perpendicularly to this, no obvious structure can be seen from the (u, v)–data. The good agreement between the model and the data also allowed to derive a model visibility distribution in the (u, v)–plane as the Fourier transform of the

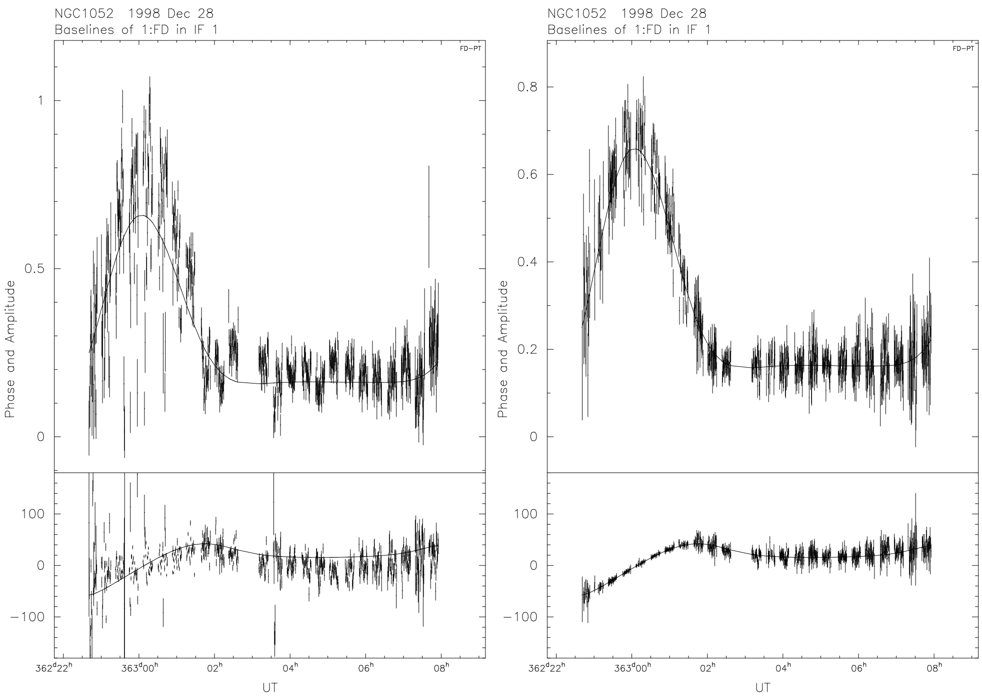

Figure 3.7: 43 GHz Visibility amplitude (top) and phase (bottom) versus time on the baseline FD–PT. Left: *A–priori* calibrated data; Right: Edited and fully calibrated data. The data are shown as points with error bars, and the final model is plotted in both cases as a continuous line.

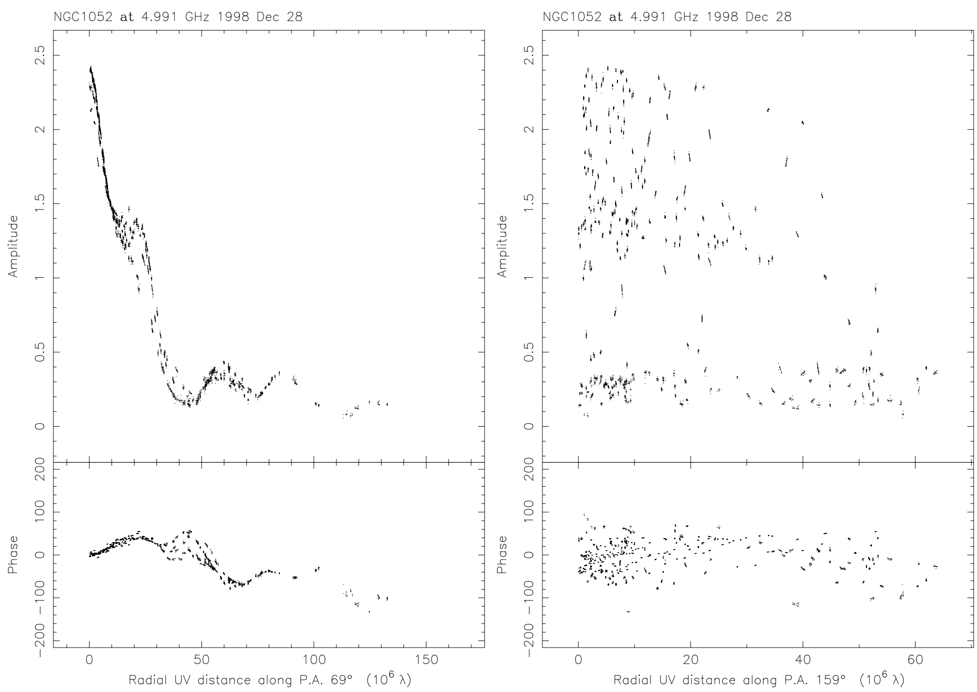

Figure 3.8: The visibility distribution projected on two perpendicular planes in the (u, v)–plane. The local maxima, visible in the left panel (P.A.=69°), correspond to the side-lobes of the visibility amplitude in the (u, v)–plane, in Figure 3.9.

model brightness distribution. Figure 3.9 shows contour plots of the brightness distribution ((x, y) domain) and the visibility amplitude ((u, v)–domain). The (u, v)–plane sampling points ((u, v)–coverage) at which the visibility was measured are shown superimposed on the model visibility amplitudes. The amplitude of the visibility is dominated by a central maximum (note the uneven contour levels given in the figure caption). Along P.A.=69° several side-lobes are prominent, corresponding to the fringes in Figure 3.8.

Polarization calibration and mapping the polarization structure: In very long baseline polarimetric (VLBP) observations the antenna feeds record circular polarization in both hands, RCP and LCP. From the observations of NGC 1052 in December 1998 the cross correlations r_{mn}^{RR}, r_{mn}^{LL}, r_{mn}^{RL} and r_{mn}^{LR} for each antenna pair m, n were formed in the VLBA correlator from the measured right circular and left circular polarized (RCP and LCP) signals. These cross correlations have to be corrected for instrumental effects, described in this paragraph, in order to derive the true visibilities $\mathfrak{RR}, \mathfrak{LL}, \mathfrak{RL}$ and $\mathfrak{LR}$. Following the discussion of Leppänen et al. (1995), the four Stokes parameters I, Q, U and V, which specify the polarimetric properties of the source radiation, can be obtained as the Fourier transform (indicated by $\rightleftharpoons$) of these correlations

$$\begin{aligned} \mathfrak{RR} &\rightleftharpoons I + V \\ \mathfrak{LL} &\rightleftharpoons I - V \\ \mathfrak{RL} &\rightleftharpoons Q + iU = P \\ \mathfrak{LR} &\rightleftharpoons Q - iU = P^* \quad , \end{aligned} \tag{3.10}$$

where $P = p\mathrm{e}^{2i\chi}$, with p the polarized intensity and χ the electric vector position angle (EVPA). Unfortunately, real antenna feeds do not exclusively register one single polarization, some leaking of the opposite hand is always present. This effect of instrumental polarization can be expressed in a model of the interferometer response (Kemball et al. 1995:

$$\begin{aligned} r_{mn}^{RR} &= g_m^R g_n^{R*} \{ \mathrm{e}^{-i(\alpha_m - \alpha_n)} \cdot \mathfrak{RR} + D_m^R \mathrm{e}^{i(\alpha_m + \alpha_n)} \cdot \mathfrak{LR} \} \\ &\quad + D_n^{R*} \{ \mathrm{e}^{-i(\alpha_m + \alpha_n)} \cdot \mathfrak{RL} + D_m^R D_n^{R*} \mathrm{e}^{i(\alpha_m - \alpha_n)} \cdot \mathfrak{LL} \} \\ r_{mn}^{LL} &= g_m^L g_n^{L*} \{ \mathrm{e}^{i(\alpha_m - \alpha_n)} \cdot \mathfrak{LL} + D_m^L \mathrm{e}^{-i(\alpha_m + \alpha_n)} \cdot \mathfrak{RL} \} \\ &\quad + D_n^{L*} \{ \mathrm{e}^{i(\alpha_m + \alpha_n)} \cdot \mathfrak{LR} + D_m^L D_n^{L*} \mathrm{e}^{-i(\alpha_m - \alpha_n)} \cdot \mathfrak{RR} \} \\ r_{mn}^{RL} &= g_m^R g_n^{L*} \{ \mathrm{e}^{-i(\alpha_m + \alpha_n)} \cdot \mathfrak{RL} + D_m^R \mathrm{e}^{i(\alpha_m - \alpha_n)} \cdot \mathfrak{LL} \} \\ &\quad + D_n^{L*} \{ \mathrm{e}^{-i(\alpha_m - \alpha_n)} \cdot \mathfrak{RR} + D_m^R D_n^{L*} \mathrm{e}^{i(\alpha_m + \alpha_n)} \cdot \mathfrak{LR} \} \\ r_{mn}^{LR} &= g_m^L g_n^{R*} \{ \mathrm{e}^{i(\alpha_m + \alpha_n)} \cdot \mathfrak{LR} + D_m^L \mathrm{e}^{-i(\alpha_m - \alpha_n)} \cdot \mathfrak{RR} \} \\ &\quad + D_n^{R*} \{ \mathrm{e}^{i(\alpha_m - \alpha_n)} \cdot \mathfrak{LL} + D_m^L D_n^{R*} \mathrm{e}^{-i(\alpha_m + \alpha_n)} \cdot \mathfrak{RL} \} \end{aligned} \tag{3.11}$$

In these expressions, the subscripts m, n denote different antennas, the superscripts R, L denote different polarizations and the parallactic angles are denoted by α. The g-factors represent the complex antenna gains and the D–terms the ratios of the received unwanted polarization to the received nominal polarization in the complex voltage response (or leaking between the polarization hands). Note that the D–terms are the only quantities in these formulae, which are not known from the *a–priori* calibration of the data in $\mathcal{AIPS}$. Especially the parallactic angle correction that has been performed (page 36) simplifies the formulae since this correction corresponds to the substitution

$$g_m^R \mathrm{e}^{-i\alpha_m} \rightarrow g_m^R, \quad g_m^L \mathrm{e}^{i\alpha_m} \rightarrow g_m^L, \tag{3.12}$$

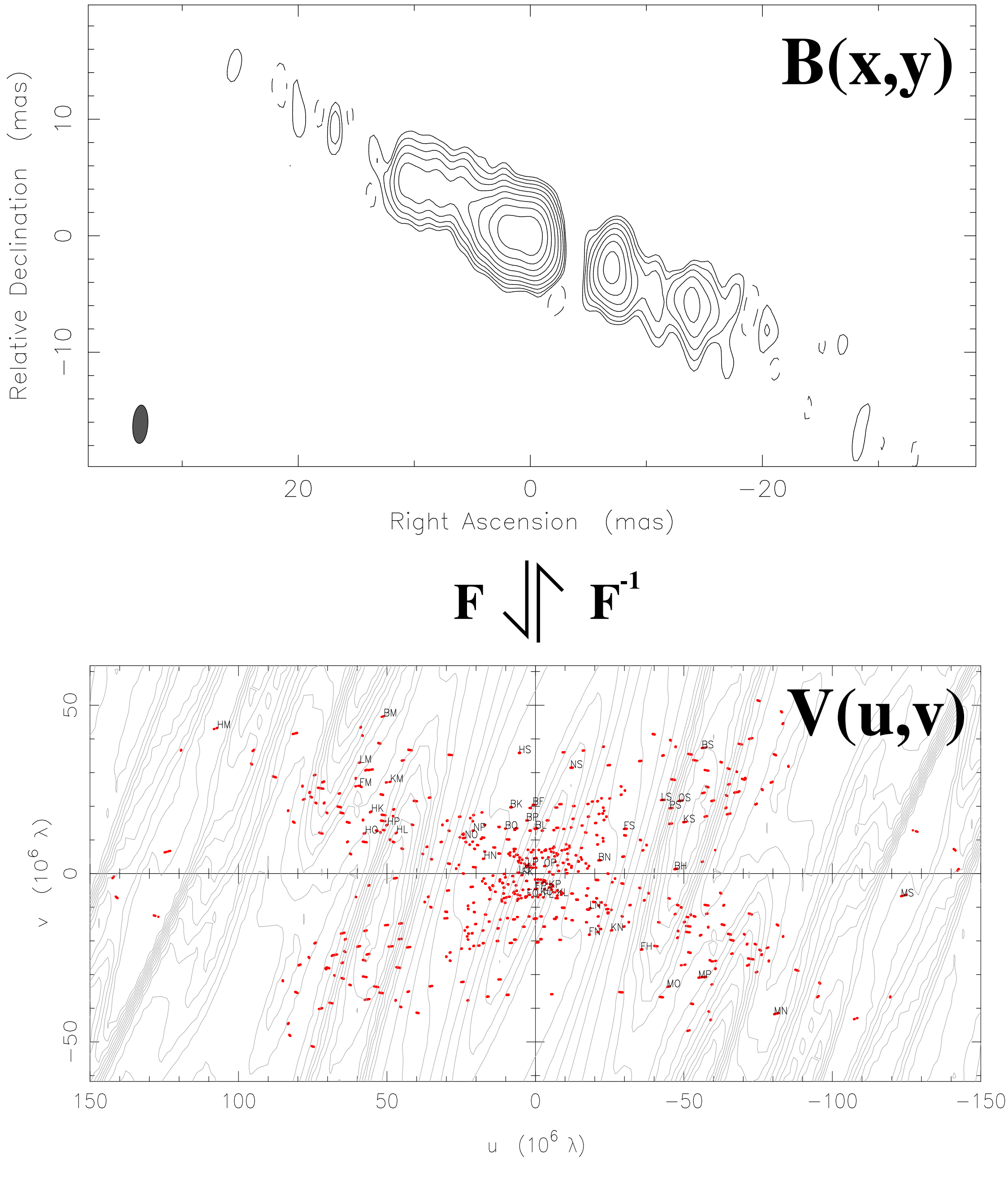

Figure 3.9: Top: Contour image of the brightness distribution ($B(x,y)$) of NGC 1052 at 5 GHz. Bottom: Contour plot of the (real part of the) Fourier transform of the brightness distribution, the visibility amplitude in the (u,v)–plane. The contours for 0.1, 0.125, 0.15, 0.175, 0.2, 0.225, 0.25, 0.275, 0.3, 0.35, 0.4, 0.6, 0.8, 1, 1.2, 1.4, 1.6, 1.8, 2, and 2.2 Jy are shown. Superimposed is the (u,v)–coverage during the experiment.

representing a rotation of the gain phases by the time dependent parallactic angle. A further simplification is achieved by neglecting second and third order terms in D, $\mathfrak{RL}$ and $\mathfrak{LR}$, since both the D–terms and the fractional polarization $\mathfrak{m} = P/I \propto \mathfrak{RL} \propto \mathfrak{LR}$ are small quantities. If additionally circular polarization is neglected ($\mathfrak{RR} = \mathfrak{LL} = \mathfrak{I} \rightleftharpoons I$) Equation (3.11) become

$$\begin{aligned} r_{mn}^{RR} &= g_m^R g_n^{R*} \cdot \mathfrak{I} \\ r_{mn}^{LL} &= g_m^L g_n^{L*} \cdot \mathfrak{I} \\ r_{mn}^{RL} &= g_m^R g_n^{L*} \{\mathfrak{RL} + (D_m^R \mathrm{e}^{2i\alpha_m} + D_n^{L*} \mathrm{e}^{2i\alpha_n}) \cdot \mathfrak{I}\} \\ r_{mn}^{LR} &= g_m^L g_n^{R*} \{\mathfrak{LR} + (D_m^L \mathrm{e}^{-2i\alpha_m} + D_n^{R*} \mathrm{e}^{-2i\alpha_n}) \cdot \mathfrak{I}\} \quad . \end{aligned} \tag{3.13}$$

Equations (3.13) represent a linearized model of the interferometer response in VLBP experiments. It is based on the assumption that the D–terms are small ($< 5\%$), which is usually true for observations made with the VLBA.

To the degree that these are valid assumptions, Equation (3.13) shows that the parallel-hand cross correlations (r_{mn}^{RR}, r_{mn}^{LL}) respond only to the total intensity I and the cross-hand correlations (r_{mn}^{RL}, r_{mn}^{LR}) are sensitive to linearly polarized intensity. Once the D–terms are known, the true visibilities $\mathfrak{RR}, \mathfrak{LL}, \mathfrak{RL}$ and $\mathfrak{LR}$ can be determined from Equation (3.13) and the degree of linear polarization $\mathfrak{m}$ and the EVPA χ from Equation (3.10):

$$\mathfrak{m} = \frac{\sqrt{Q^2 + U^2}}{I}, \quad \chi = \frac{1}{2} \cdot \arctan\left(\frac{U}{Q}\right) \tag{3.14}$$

The D–terms are complex quantities. Their modulus affect the degree of polarization and their phase determines the polarization plane. Equation (3.10) shows that the latter depends on the phase difference between the $\mathfrak{RL}$ and the $\mathfrak{LR}$ cross correlations. Since χ is determined by the difference of $\mathfrak{RL}$ and $\mathfrak{LR}$, an offset for both is usually allowed. Special care has to be taken therefore to calibrate the absolute EVPA of the radiation.

Leppänen et al. (1995) developed an algorithm to determine the instrumental polarization leakage factors and to separate the source and instrumental polarization, using the target source itself. This algorithm was applied to self–calibrate the polarization characteristics of the VLBA in the polarimetric observation of NGC 1052, since the polarization of the source was unknown and, especially at the high frequencies, no suitable calibrators were available. This calibration step, usually referred to as feed calibration, is described in this paragraph. The only assumption in this algorithm is the spatial coincidence of polarized emission (if any) with the total intensity emission. To account for this constraint, a model for the total intensity, available from imaging in DIFMAP (or IMAGR within $\mathcal{AIPS}$), is used. To allow structural differences between the polarized and the total intensity structure, this model is divided into sub–models, whose polarizations are characterized by complex coefficients $p_s = (Q_s + iU_s)/I_s$) for each sub-model with the total intensity I_s. Setting the gain terms to unity and substituting the true parallel hand visibilities ($\mathfrak{I} = \mathfrak{RR} = \mathfrak{LL}$) with the observed counterparts (r_{mn}^{LL} and r_{mn}^{RR}), which is allowed if the gain self–calibration in DIFMAP has worked properly, the cross hand terms in Equation (3.13) become

$$\begin{aligned} \tilde{r}_{mn}^{RL}(u,v) &= \textstyle\sum_s p_s \mathfrak{I}_s(u,v) + D_m^R \mathrm{e}^{2i\alpha_m} r_{mn}^{LL}(u,v) + D_n^{L*} \mathrm{e}^{2i\alpha_n} r_{mn}^{RR}(u,v) \\ \tilde{r}_{mn}^{LR}(u,v) &= \textstyle\sum_s p_s^* \mathfrak{I}_s(u,v) + D_m^L \mathrm{e}^{-2i\alpha_m} r_{mn}^{RR}(u,v) + D_n^{R*} \mathrm{e}^{-2i\alpha_n} r_{mn}^{LL}(u,v) \quad , \end{aligned} \tag{3.15}$$

with $\mathfrak{I}(u,v)$, the Fourier transform of I_s and the sum over all sub-models. A linear least–squares–fit to the measured cross polarized visibilities can determine the unknown factors

p_s and D_m. The details of this algorithm can be found in Leppänen et al. (1995) and shall not be discussed here. However, the way the model is divided does not affect the solution, as long as the model has enough degrees of freedom to fit the true distribution of polarized emission. This requires a good enough parallactic angle coverage and a not too complicated polarization structure of the source.

As already mentioned, a common offset in the RCP and LCP gains does not affect the quality of the fit, since it is only the difference between both which is taken into account. This leads to the need for an absolute calibration of the EVPA, which is actually affected by such a common offset. In principle the application of the phase-cal information with PCCOR during the *a–priori* calibration should have removed such ambiguities, but it is necessary to check this externally. The way the EVPA can be calibrated depends on the special observation characteristics, and in Section 4.5 it is described how this was actually obtained in the case of NGC 1052.

To perform the feed calibration using the described algorithm, the best CLEAN component model from the hybrid mapping process in DIFMAP, contained in a FITS file was read into $\mathcal{AIPS}$ for all four frequencies, using the task IMLOD. The model information is contained in a CLEAN component (CC) table of the image. Using this model the (u, v)–data were phase self–calibrated with the task CALIB. Bad data points were flagged, using the task CLIP, by setting appropriate clipping levels, known from the data examination within DIFMAP, for the four Stokes parameters. With the fully calibrated data a total intensity source model was obtained with the task IMAGR within $\mathcal{AIPS}$. The map-size, the cell-size, the number of iterations and the weighting of the data had to be specified, which were all known from the mapping procedure within DIFMAP. The resulting map was checked for consistency with the map produced by DIFMAP. From the $\mathcal{AIPS}$ image file the CC table was now subdivided into ten sub-CC tables with the task CCEDT. Specifying these ten sub-models, a linear approximation of the D–terms was performed with the task LPCAL, according to Equation (3.15), which writes the results into the antenna table (AN), to be examined with the task PRTAN. The determination of the D–terms yielded values below 5% (except SC at 22 and 43 GHz), and are shown in Table 3.1. With the knowledge of the D–terms the Stokes parameters Q, U and V can be mapped, with the same mapping parameters of IMAGR as for the Stokes I map. The phase calibration from CALIB guarantees the proper registration of the maps with different Stokes parameters. Maps of the polarized intensity were produced, combining the corresponding Q and U maps with the task COMB (to be plotted with the task PCNTR). In Section 4.5 the results are presented and discussed. The basic path of feed calibration in $\mathcal{AIPS}$ is plotted schematically in Figure 3.10.

Table 3.1: The D–terms of the VLBA antennas on Dec 28th 1998

Antenna	Feed pol. type	D_5^{a}	$D_{8.4}^{\mathrm{b}}$	D_{22}^{c}	D_{43}^{d}
BR	RCP	$0.0041\mathrm{e}^{i149.0}$	$0.0216\mathrm{e}^{i148.1}$	$0.0268\mathrm{e}^{i77.8}$	$0.0342\mathrm{e}^{i286.3}$
(Brewster)	LCP	$0.0107\mathrm{e}^{i50.9}$	$0.0086\mathrm{e}^{i250.2}$	$0.0113\mathrm{e}^{i146.4}$	$0.0376\mathrm{e}^{i232.4}$
FD	RCP	$0.0086\mathrm{e}^{i144.1}$	$0.0064\mathrm{e}^{i64.9}$	$0.0043\mathrm{e}^{i55.3}$	$0.0144\mathrm{e}^{i281.7}$
(Fort Davis)	LCP	$0.0104\mathrm{e}^{i39.3}$	$0.0138\mathrm{e}^{i153.0}$	$0.0122\mathrm{e}^{i46.1}$	$0.0163\mathrm{e}^{i23.5}$
HN	RCP	$0.0115\mathrm{e}^{i177.1}$	$0.0153\mathrm{e}^{i79.3}$	$0.0290\mathrm{e}^{i343.5}$	$0.0479\mathrm{e}^{i232.9}$
(Hancock)	LCP	$0.0067\mathrm{e}^{i45.6}$	$0.0152\mathrm{e}^{i126.8}$	$0.0252\mathrm{e}^{i146.9}$	$0.0355\mathrm{e}^{i349.6}$
KP	RCP	$0.0137\mathrm{e}^{i156.8}$	$0.0019\mathrm{e}^{i176.1}$	$0.0250\mathrm{e}^{i36.8}$	$0.0150\mathrm{e}^{i248.8}$
(Kitt Peak)	LCP	$0.0136\mathrm{e}^{i33.3}$	$0.0060\mathrm{e}^{i123.3}$	$0.0123\mathrm{e}^{i176.4}$	$0.0200\mathrm{e}^{i225.2}$
LA	RCP	$0.0125\mathrm{e}^{i149.2}$	$0.0046\mathrm{e}^{i143.5}$	$0.0158\mathrm{e}^{i310.7}$	$0.0225\mathrm{e}^{i302.8}$
(Los Álamos)	LCP	$0.0115\mathrm{e}^{i22.9}$	$0.0118\mathrm{e}^{i178.4}$	$0.0083\mathrm{e}^{i29.0}$	$0.0102\mathrm{e}^{i217.8}$
MK	RCP	$0.0080\mathrm{e}^{i188.7}$	$0.0017\mathrm{e}^{i299.9}$	$0.0085\mathrm{e}^{i235.6}$	$0.0493\mathrm{e}^{i216.6}$
(Mauna Kea)	LCP	$0.0135\mathrm{e}^{i348.8}$	$0.0114\mathrm{e}^{i175.5}$	$0.0217\mathrm{e}^{i42.9}$	$0.0124\mathrm{e}^{i113.1}$
NL	RCP	$0.0196\mathrm{e}^{i154.5}$	$0.0059\mathrm{e}^{i58.8}$	$0.0346\mathrm{e}^{i14.1}$	$0.0413\mathrm{e}^{i331.8}$
(North Liberty)	LCP	$0.0134\mathrm{e}^{i10.3}$	$0.0066\mathrm{e}^{i107.3}$	$0.0289\mathrm{e}^{i164.1}$	$0.0299\mathrm{e}^{i193.5}$
OV	RCP	$0.0063\mathrm{e}^{i155.9}$	–[e]	–[e]	$0.0224\mathrm{e}^{i100.7}$
(Owens Valley)	LCP	$0.0068\mathrm{e}^{i7.9}$	–[e]	–[e]	$0.0287\mathrm{e}^{i344.7}$
PT	RCP	$0.0121\mathrm{e}^{i163.1}$	$0.0098\mathrm{e}^{i192.1}$	$0.0082\mathrm{e}^{i158.4}$	$0.0239\mathrm{e}^{i275.4}$
(Pie Town)	LCP	$0.0203\mathrm{e}^{i17.8}$	$0.0086\mathrm{e}^{i19.6}$	$0.0155\mathrm{e}^{i192.7}$	$0.0350\mathrm{e}^{i74.5}$
SC	RCP	$0.0071\mathrm{e}^{i225.0}$	$0.0152\mathrm{e}^{i168.8}$	$0.0609\mathrm{e}^{i195.3}$	$0.0402\mathrm{e}^{i242.0}$
(St. Croix)	LCP	$0.0036\mathrm{e}^{i11.8}$	$0.0089\mathrm{e}^{i24.2}$	$0.0805\mathrm{e}^{i318.9}$	$0.0596\mathrm{e}^{i183.5}$

[a] D–terms at 5 GHz; [b] D–terms at 8.4 GHz; [c] D–terms at 22 GHz; [d] D–terms at 43 GHz; [e] OV did not observe at 8.4 and 22 GHz

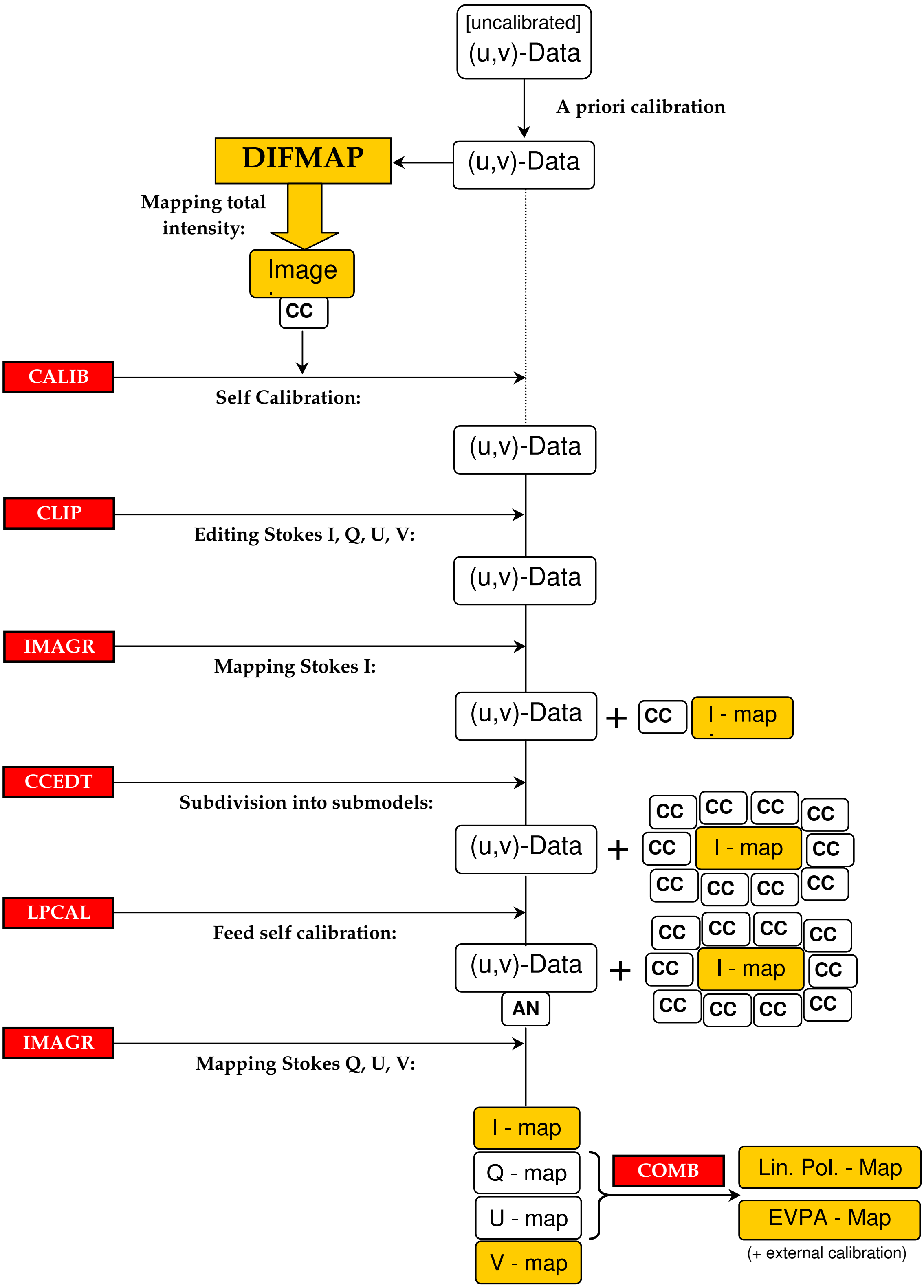

Figure 3.10: The basic feed self–calibration path in $\mathcal{AIPS}$.

Chapter 4

Results

In this chapter I will present and discuss the results obtained from the multi–frequency VLBI observations of NGC 1052. I will start with the presentation of the VLBI images (Section 4.1), produced from the self–calibrated (u, v)-data. The pre-analysis of these images will include the alignment and modeling of the VLBI structure of NGC 1052 at the four observed frequencies (Section 4.2). In Section 4.3, the spectral properties of NGC 1052 and the various components in the jets will be discussed. A method to obtain source information from the brightness temperature distribution across the source will be presented and applied in Section 4.4 . The polarimetric properties of NGC 1052 on VLBI scales will be reported, for the first time, in Section 4.5 . In Section 4.6, an analysis of the core-shift of the two jet–cores with respect to frequency will be performed.

4.1 Total intensity mapping

Figure 4.1 shows the total intensity images, produced with the hybrid mapping software DIFMAP (Pearson et al. 1994), as described in Chapter 3. The main characteristics of the source visible in these images, which are described in the following, are summarized in Table 4.1. Table 4.2 gives the map parameters.

The basic features in the VLBI structure of NGC 1052 are two oppositely directed jets divided by an emission gap in between. These are visible in the 5 and 8.4 GHz map with a resolution of about 3 and 2 mas, respectively. At 5 GHz structures out to about 30 mas from the gap on both sides can be seen. At 8.4 GHz, emission out to about 14 mas on both sides from the gap is visible.

At both frequencies, the source geometry can be described by a position angle (P.A.) of approximately 65° (−155° for the western jet)[1]. The source exhibits a kink about 8 mas east from the gap, where the eastern jet turns slightly to the north and back to its old direction some milliarcseconds further out. Although not that pronounced, this kink is visible as well in the 8.4 GHz map at the same distance from the gap.

The 22 GHz image shows the inner part of the eastern jet out to 6 mas from the gap and a slightly shorter western jet out to about 4 mas from the gap both with submilliarcsecond resolution. Marginally detected emission is spread out to 13 mas in the eastern jet and to 6 mas on the western side. The eastern jet seems to be slightly curved on this scale with the P.A. changing smoothly from 67° to 83° (counterclockwise, in contrast to the behavior

[1]The P.A. is measured from north through east.

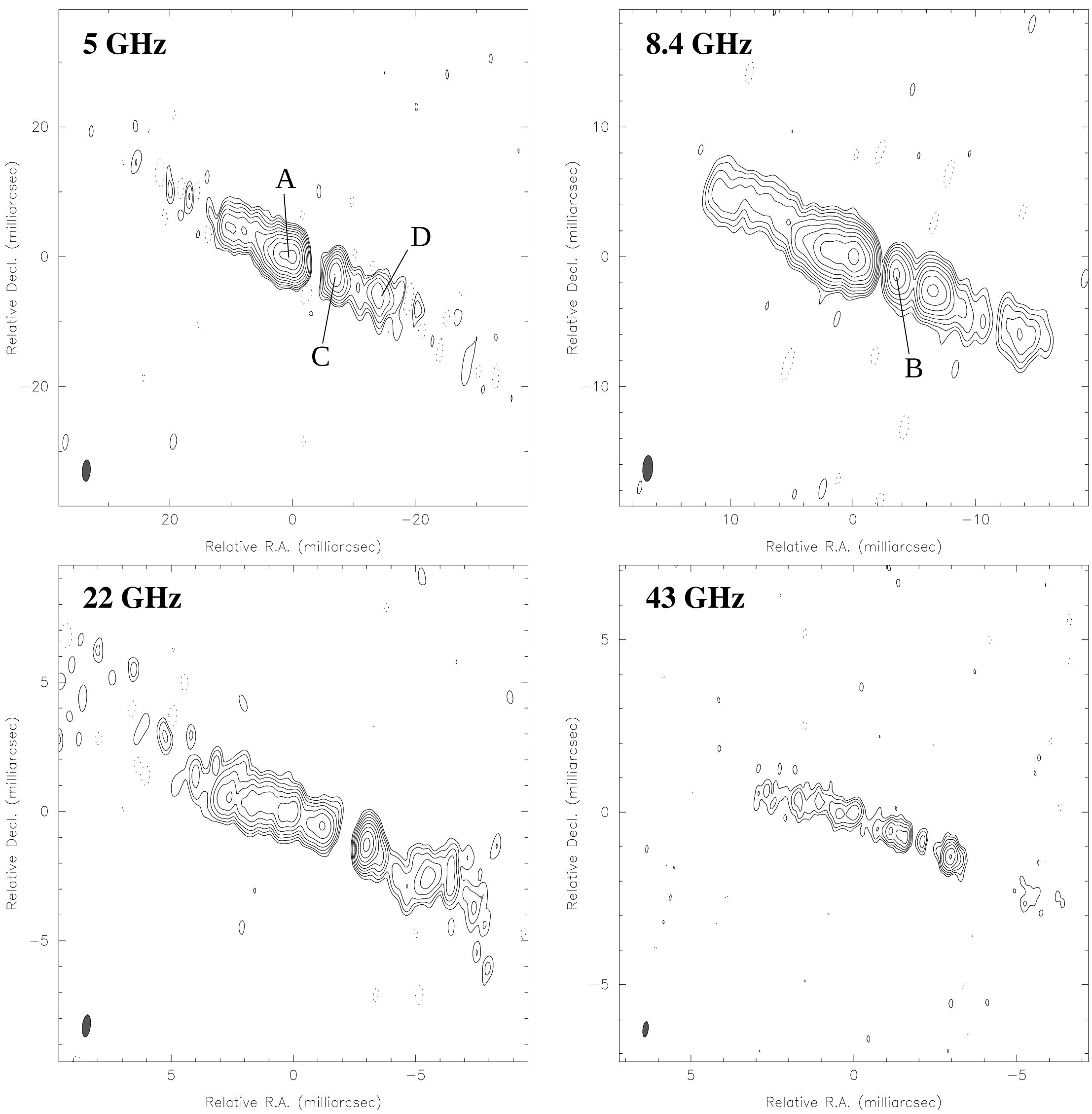

Figure 4.1: Contour plots of the total intensity flux of NGC 1052 at the observed frequencies. The convolution beams are shown at the bottom left corner of each map. Table 4.1 summerizes the source characteristics at each frequency and Table **??** gives the map parameters. Note the different map scales at the different frequencies.

at the kink further out at lower frequencies). The western jet shows strong curvature. From the very prominent core (component B) the outflow has an initial position angle of $-140°$. At 3 mas from the gap the position angle changes by $90°$ to $-50°$ followed by a slower curvature towards the P.A. of $-155°$, visible at the lower frequency maps.

The 43 GHz image could be misinterpreted, if it had been obtained from a single frequency observation, as a one–sided source with a strong core and only marginal emission on the counterjet side. The comparison with the 22 GHz image, however, ascribes this strong core (component B) to the western jet (look for details at the model fitting and the core–shift analysis results in Section 4.2 and 4.6) and the curved structure in the east of it to the eastern jet. The curvature is consistent with the 22 GHz map but emission is only visible out to 5 mas from the gap. The angular resolution achieved here is about 0.5 mas (see table 4.2 for the exact map parameters).

The angular distance measurements in this paragraph are based on the interpretation of component B as the core of the western jet and the gap position between it and the next component on its east side at 43 GHz. This interpretation will be tested and discussed in more detail in Section 4.6 but seems reasonable even at this point of the analysis.

The jets appear nearly symmetric in the 5 GHz and 8.4 GHz maps, symmetry becoming less prominent at higher frequencies. At 43 GHz the eastern jet appears very rich in detail while in the western jet only two components remain detectable above the noise level. The emission gap is most prominent at 5 GHz. The maps at 8.4, 22 and 43 GHz reveal jet components occupying the region where the gap is located at 5 GHz, leaving a smaller but still prominent gap–region left. The eastern jet appears rather continuous with a strong inner region (labeled as component A) and fainter emission further out from the center of symmetry. The western jet has a much more fragmentary structure. It seems to be composed of single "blobs" which are unresolved and partly blended at low frequencies.

It is not easy to identify the single components at different frequencies. Especially between 5 and 8.4 GHz the identification is problematic because the higher frequency map shows a larger number of components than the lower frequency one. Although this problem cannot be overcome just by a visual inspection of the maps (but the next section will deal with the topic of alignment) there are hints for an alignment, which identifies the innermost part of the western jet at 5 GHz (component C) with the second component from the gap at 8.4 GHz. The core of the western jet (component B) is too weak to be detectable at 5 GHz but becomes more and more dominant at higher frequencies. At 8.4 GHz it occupies nearly the whole 5 GHz–gap region.

Table 4.1: Source characteristics on mas-scales

ν	Mean P.A.	eastern jet extension	western jet extension	Gap region	Notes
5 GHz	$\sim 65°$	30 mas	30 mas	prominent, $\sim$1.25 mas	A dominates; B totally absorbed; kink, 8 mas east of the gap
8.4 GHz	$\sim 65°$	14 mas	14 mas	nearly closed	A dominates; B occupies the 5 GHz gap-region; kink, 8 mas east of the gap
22 GHz	$\sim 67°$	13 mas	6 mas	prominent, $\sim$0.45 mas	B dominates; curved eastern jet (P.A.ϵ [67°,83°]); heavy bending of the western jet
43 GHz	$\sim 70°$	5 mas	3.5 mas	$\sim$0.2 mas	B dominates; curved eastern jet (P.A.ϵ[67°,83°]

Table 4.2: Total intensity map parameters

ν [Hz]	λ [cm]	beam [mas × mas,°]	S_{peak} [Jy/beam]	S_{tot} [a] [Jy]	rms [mJy/beam]	Contours [d] [mJy/beam]
5	6	3.30 × 1.31,–3.74	0.660 [b]	2.41	0.26	0.99 × (-1,1,2,4,...,256,512)
8.4	4	1.98 × 0.81 ,–3.87	0.538 [b]	2.39	0.25	0.81 × (-1,1,2,4,...,256,512)
22	1.3	0.86 × 0.32 ,–7.63	0.339 [c]	1.51	1.20	1.02 × (-1,1,2,4,...,128,256)
43	0.7	0.45 × 0.16 ,–7.93	0.126 [c]	0.67	0.67	1.89 × (-1,1,2,4,...,16,32,64)

[a] Total flux density recovered in the map model; [b] Corresponds to the A component; [c] Corresponds to the B component; [d] Contours in Figure 4.1 (There are more maps in the following sections with different contours).

4.2 Model fitting and image alignment

In VLBI imaging the absolute positional information is lost in the phase-calibration process. In the case of simultaneous multi-frequency observations this means that *a–priori* it is not clear how the images at the different frequencies have to be aligned. The ideal method for overcoming this is to carry out phase-referencing observations, using a compact nearby object and using it to calculate the position of the target source relative to it. Our VLBA observations were not phase-referenced, so another way was used to register the four maps. For this a model fitting of the visibilities with circular[2] Gaussian components was performed.

The aim of model fitting is to find a simple parametrization of the data using only a few model components which should be identifiable with characteristic features in the total intensity images. A pairwise identification of the model components between adjacent frequencies then allows to register the images. As another benefit the spectra of the model components can be derived.

The model fitting was performed in DIFMAP in a very similar way to the CLEANing and phase self-calibration process (without amplitude calibration) of the total intensity maps. The (uv)–data was approximated in a first step by just one model component in the phase center in varying its full width at half maximum (FWHM) and the contained flux density. Then the residual map was inspected and a second model component was added at the position of the largest residual. This second component was set to be variable in flux density, position and diameter. DIFMAP allows to vary these parameters in order to minimize the deviations between model and data in performing a least squares fit. The number of model fit iterations had to be specified and additional model components were added and fitted in the same way. Once a good approximation to the data was found (which was checked by comparing the model visibilities to the data in the tasks RADPLOT, VPLOT,... as in the hybrid mapping process) a self-calibration of the phases was performed. It is always possible to reduce the deviations between a model and the data by adding more components, resulting in more degrees of freedom for the fitting procedure. For this, it had to be checked if the introduction of a new component improved the fit significantly to justify the necessity of this component. The quality of the achieved fit was determined by the value of χ^2, the likelihood, which is a measure of the deviations between model and data being the sum of the squared differences at each data point (in the visibility domain) divided by the number of degrees of freedom (reduced χ^2). For a good fit this value should be of the order of one.

The fits were performed initially independently in order not to be biased one by another. Once good fits for all four frequencies were obtained, a cross inspection of the resulting maps was done and the fits were modified in order to get a set of model fits as consistent as possible. Criteria for consistency are:

- Regions which show emission at two adjacent frequencies should be represented by the same number of components.
- In the outer parts components should tend to fade away towards higher frequencies as they most likely represent optically thin synchrotron emitting regions.

[2]Although less realistic than elliptical components, we used circular Gaussian components to reduce the degrees of freedom of the model and to make the models comparable between the different frequencies.

- In the inner parts of both jets there can be new components showing up at higher frequencies, which have no low frequency counterpart due to external or self absorption.
- Optically thin features should not show positional changes with frequency. In other words, it should be possible to align the model maps in a way that all optically thin features are connected by vertical lines, if the maps are plotted one above the other.
- Optically thick features are expected at the base of both jets and not at the outer parts. They should have the tendency to be shifted closer to the gap at higher frequencies exhibiting a "V"–like structure in the gap region.
- "Strange spectra", i.e. components which first become dimmer and then brighter again with rising frequency, indicate the influence of two distinct physical emission regions. They should be checked and possibly divided into two separate components.

To achieve a maximal consistency between adjacent frequencies, model components can be added to one of the two models if the reduced χ^2 decreases significantly. Alternatively, components can be taken away from the other model if this does not alter the value of χ^2 too much.

Tables 4.3 to 4.6 give the parameters of the final models for the four frequencies. The errors were determined with the program ERFIT, a program from the Caltech VLBI data analysis package (California Institute of Technology 1991), that calculates the statistical confidence intervalls of the fitted model parameters. The obtained values of χ^2 are all satisfactory small but at the price of a rather big number of model components. Over the frequencies 15 model components were needed for the eastern jet of which 9 are contained in the 5 GHz–fit and 11, 8 and 10 in the 8.4, 22 and 43 GHz–fits, respectively. For the western jet 4, 6, 5 and 3 components were needed for the fits resulting to a total number of 8 jet components after the cross identification. Especially the cross check of the resulting maps with the total intensity maps obtained with the CLEAN algorithm argued convincingly against a smaller number of components at any frequency. The image alignment was performed in three steps:

1. A reliable alignment of the model fit maps had to be found. For this the fitted components first had to be cross–identified. Then the model fit maps could be aligned pairwise, assuming frequency independent positions of optically thin features. Above 8.4 GHz the position of the component A7 in the 43 GHz model was used as a measure of relative shifts between adjacent frequency models since this component is relatively strong at all three frequencies and unambiguously identifyable. A shift of 0.008 mas to the west and 0.014 mas to the south of the 22 GHz model as well as of the 8.4 GHz model (with respect to the 43 GHz model) was determined. For the alignment of the 5 GHz and the 8.4 GHz model fit maps the distance between the two most distant components was measured and the center was calculated for both frequencies. This center then was assumed to be intrinsically spatially coincident resulting to a shift of 0.115 mas to the west and 0.051 mas to the south for the 5 GHz model.

   In Figure 4.3 the aligned model fit maps are shown and the model fit component identifications are indicated by lines. The most distant component in the eastern jet was labeled as A1, the adjacent inner one as A2, and so on. The western jet was devided into three parts following the convention introduced in Section 4.1 . The model fit component in the innermost part of the western jet were labeled as B2b, B2a, B1 from east to west. Further out the components C3b, C3a, C2, C1 and D follow.

Most of the lines in Figure 4.3 are nearly vertical indicating frequency independent component positions. This fact underlines the reliability of the obtained fits as a high quality approximation of the true source structure strikingly. Inclined connection lines arise only at points where components split into two distinct ones at the higher frequency whereas the data set could be modelled as well with only one component at the lower frequency.

At the inner edge of the eastern jet new components are showing up at higher frequencies as the innermost region components of the western jet do between 5 and 8.4 GHz. Above 8.4 GHz the innermost component in the western jet B2b moves slightly to the east. These effects represent the core–shift, discussed in detail in Section 4.6 .

2. In order to align the CLEAN maps their charactristic features first had to be identified with model components in the corresponding "model fit map". These CLEAN map features were set at the relative position of the cross–identified model components. For this the brightness peak of region C was identified with C3 in the 5 and 8.4 GHz maps, and component B2b was ascribed to the brightness peak of region B for the other pairs of CLEAN maps. The aligned CLEAN maps are shown in Figure 4.4. They contain the whole multi-frequency information obtained in the observation and will be used in the next section to derive the spectral index distribution across the source.

3. A fixpoint can be determined from which angular distances are measured as absolute distances rather than relative distances between distinct components. A natural choice for this fixpoint would be the most probable position of the true center of jet activity, namely the position of the central engine. The center between the components A15 and B2b was chosen for this purpose (see Section 4.6). The component positions in Table 4.3 to 4.6 are given relative to this reference point.

In Figure 4.2 the locations of the model components in the sky at all four observed frequencies are shown. The cross–identification of the various components is very obvious in this plot for the most cases. The errors in x (R.A.) and y (Dec.) have been calculated from the statistical errors in r and ϕ, from the ERFIT-output. For the most components, these errors are to small to be visible in Figure 4.2, especially at the highest frequencies. The components in both jets do not follow a straight trajectory, but are aligned along a helical path. The helical structure is more pronounced at the highest frequencies and has an opening angle of $\sim 10°$ in the eastern jet and $\sim 15°$ in the western jet.

Although the pieces of this puzzle fit convincingly well, it has to be remarked that the method of alignment used here is not *a–priori* definite. It is based on the assumption that optically thin components have frequency-independent positions and that the cross identification of the model components is correct. However, it is obvious that the used identification is the most reasonable as a shift of the whole set of model components

Table 4.3: 5 GHz model fit parameters ($\chi^2_{red} = 1.12$).

Component	Flux density [mJy]	Radius[a] [mas]	P.A.	FWHM [mas]
A1	80±2	14.56±0.03	66.5±0.1	2.14±0.03
A2	54±2	12.01±0.04	63.6±0.1	1.87±0.08
A3	60±2	9.61±0.05	65.3±0.3	1.63±0.04
A4	150±7	7.46±0.05	71.7±0.2	0.99±0.02
A5	338±37	6.0±0.2	72.8±0.1	0.93±0.25
A6	447±48	5.1±0.1	72.8±0.2	0.83±0.19
A7/8	450±28	4.0±0.1	71.0±0.2	0.69±0.08
A9	397±30	3.1±0.2	71.1±0.3	0.20±0.07
A10	140±37	2.3±0.2	70.9±0.4	0.46±0.05
C3	137±3	3.84±0.03	-114.2±0.1	1.03±0.06
C2	59±3	4.75±0.06	-115.7±0.3	0.83±0.09
C1	24±1	7.19±0.03	-119.6±0.4	1.85±0.10
D	67±1	11.81±0.01	-114.7±0.1	2.24±0.05

[a] The radius is measured from the center between A15 and B2b (see Section 4.6).

Table 4.4: 8.4 GHz model fit parameters ($\chi^2_{red} = 1.76$).

Component	Flux density [mJy]	Radius[a] [mas]	P.A.	FWHM [mas]
A1	38±1	14.70±0.03	66.5±0.1	2.00±0.03
A2	37±1	12.04±0.04	64.0±0.1	2.34±0.08
A3	36±1	9.30±0.05	65.9±0.3	1.62±0.04
A4	83±4	7.34±0.05	71.9±0.2	0.98±0.02
A5	72±8	6.4±0.2	72.7±0.1	0.59±0.25
A6	360±26	5.5±0.1	72.8±0.2	0.81±0.12
A7	396±22	4.4±0.1	72.3±0.2	0.74±0.06
A8	146±8	3.8±0.1	69.7±0.2	0.28±0.06
A9	360±21	3.2±0.2	71.3±0.3	0.34±0.05
A10	316±47	2.7±0.2	69.2±0.4	0.31±0.03
A11	137±25	1.9±0.2	74.3±0.4	0.34±0.07
B2a/b	56±4	0.60±0.03	-119.8±0.1	0.36±0.02
B1	29±2	1.26±0.03	-119.9±0.1	0.31±0.02
C3	20±1	3.75±0.03	-114.2±0.1	1.06±0.08
C2	77±4	4.86±0.06	-114.9±0.3	0.90±0.09
C1	21±1	7.03±0.03	-119.1±0.4	1.68±0.10
D	48±1	11.95±0.01	-114.7±0.1	2.21±0.05

[a] The radius is measured from the center between A15 and B2b (see Section 4.6).

Table 4.5: 22 GHz model fit parameters ($\chi^2_{red} = 0.71$).

Component	Flux density [mJy]	Radius[a] [mas]	P.A.	FWHM [mas]
A6	138±5	5.48±0.03	72.4±0.2	0.98±0.04
A7	140±7	4.39±0.01	72.2±0.2	0.65±0.03
A8	99±5	3.72±0.01	68.1±0.2	0.47±0.03
A9	139±6	3.09±0.01	72.2±0.2	0.32±0.02
A10	144±5	2.70±0.01	68.5±0.2	0.27±0.01
A11	44±8	1.98±0.04	73.0±0.8	0.29±0.07
A12	86±15	1.53±0.04	72.1±0.4	0.26±0.06
A13	54±14	1.20±0.04	71.1±0.9	0.22±0.06
B2b	341±14	0.52±0.02	-123±1	0.21±0.01
B2a	151±14	0.72±0.05	-115±2	0.29±0.02
B1	31±2	1.38±0.02	-132±1	0.3±1.7
C3a	50±4	3.34±0.02	-116.4±0.4	0.58±0.03
C3b	86±6	4.18±0.07	-116±1	1.95±0.16

[a] The radius is measured from the center between A15 and B2b (see Section 4.6).

Table 4.6: 43 GHz model fit parameters ($\chi^2_{red} = 0.83$).

Component	Flux density [mJy]	Radius[a] [mas]	P.A.	FWHM [mas]
A6	40±2	5.36±0.03	72.8±0.2	0.92±0.05
A7	44±2	4.39±0.01	72.2±0.2	0.51±0.03
A8	39±2	3.76±0.01	68.7±0.1	0.46±0.03
A9	37±1	3.177±0.003	71.8±0.1	0.22±0.01
A10	70±1	2.772±0.004	68.4±0.1	0.33±0.01
A11	19±1	1.95±0.01	71.6±0.5	0.32±0.03
A12	57±2	1.499±0.004	70.2±0.2	0.22±0.01
A13	43±2	1.221±0.006	70.8±0.2	0.12±0.01
A14	54±1	1.017±0.003	71.9±0.2	0.08±0.05
A15	19±1	0.47±0.01	61±2	0.21±0.03
B2b	225±2	0.467±0.002	-119.2±0.3	0.224±0.002
B2a	31±2	0.779±0.007	-120.9±0.6	0.22±0.01
C3b	27±2	3.33±0.05	-116.5±0.8	0.95±0.08

[a] The radius is measured from the center between A15 and B2b (see Section 4.6).

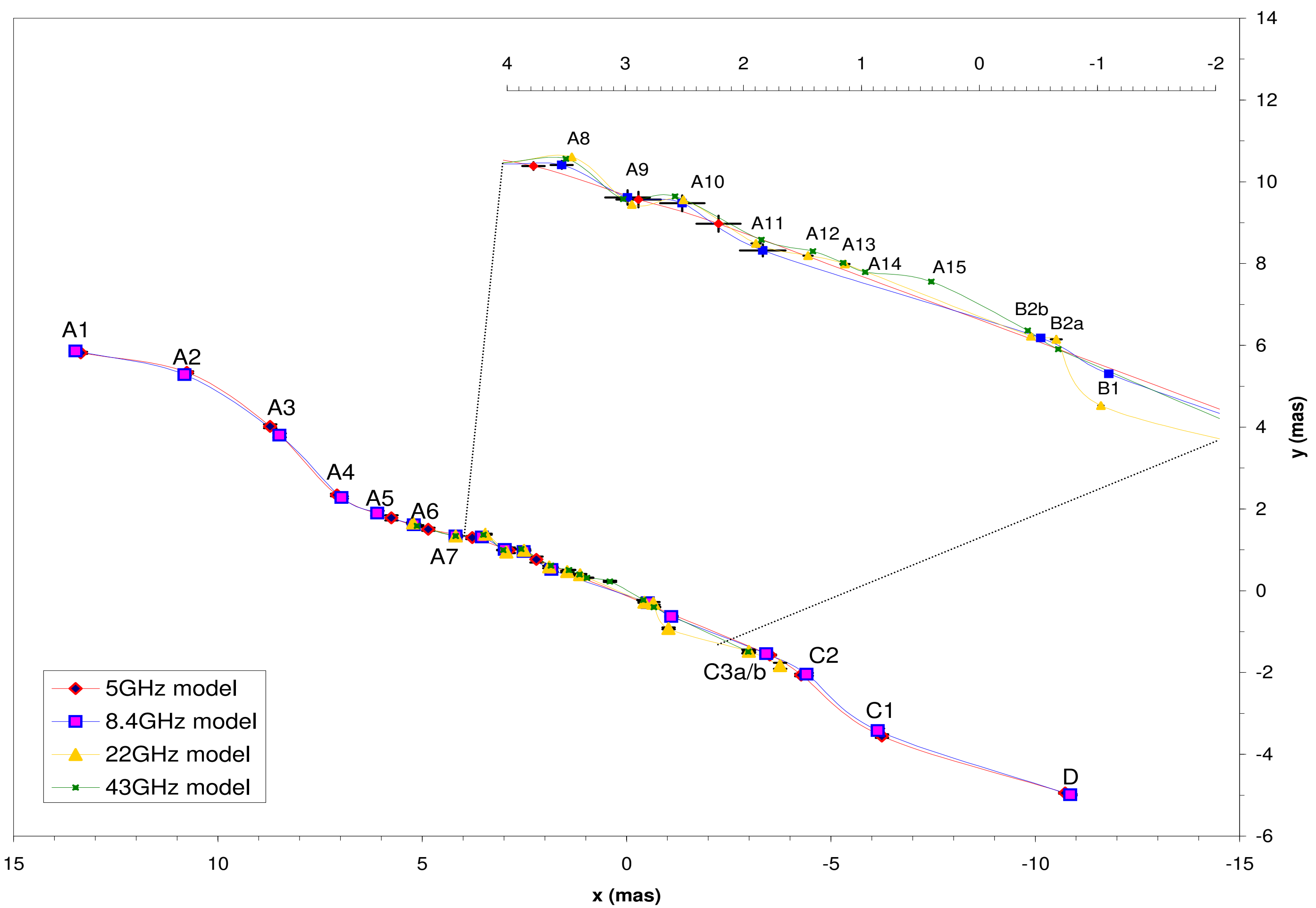

Figure 4.2: Locations of the various model components at all four observed frequencies on the sky. The positional errors in x and y have been calculated from the statistical errors in r and ϕ, as given by the ERFIT-output and are indicated in the inlaid magnification of the inner 6 mas of the source structure. The model components are aligned along a helical path with an opening angle of $\sim 10°$ of the eastern jet and $\sim 15°$ of the western jet.

concatenated with another identification introduces physical implausibilities. If one, for example, identifies the outermost component in the 8.4 GHz map with the second (counted from the east) component at 5 GHz, many of the components in the western jet have no direct counterpart and component D must be interpreted as an optically thick feature below 8.4 GHz, which seems very unlikely (see Figure 4.3). However, all possible combinations of other identifications have been tested but dismissed because of such physical implausibilities.

An impression of the full multi-frequency structure of NGC 1052 can be obtained from a film produced from the maps at the four observing frequencies. Two versions are available (see Appendix D for a detailed description), which can be obtained via the Internet at the URLs: `http://www.mpifr-bonn.mpg.de/staff/mkadler/hollywood_1052.avi` and `http://www.mpifr-bonn.mpg.de/staff/mkadler/ufa_1052.avi`, respectively.

4.3 Spectral analysis

After obtaining a reliable registration of the four maps of NGC 1052 and a cross–identification of the model fit components, there are two approaches to study its spectral properties. The first approach is to use the knowlwdge of the proper alignment of the CLEAN maps to derive maps of the spectral index between two adjacent frequencies. The second one is to derive spectra of the model fit components. Both approaches are somewhat complementary. The latter gives a handy number of component spectra which can be analyzed in detail, whereas the spectral index mapping represents the course of the spectral index along the jet axis in a more complete way yielding additional information at parts of the jet which are not represented by model components. The results of both approaches will be presented in this section.

Spectral index mapping In order to compare the aligned CLEAN maps at adjacent frequencies directly, special renditions are needed with matching uv–ranges and a common restoring beam. This can be achieved using the commands *uvtaper* and/or *restore* at the beginning and the end, respectively, of the hybrid mapping process in DIFMAP. Table 4.7 gives the restoring beams and the other relevant parameters of the derived maps. After being aligned, using the method described in the previous section, they were read into $\mathcal{AIPS}$ and combined to a spectral index map[3] using the task COMB. Since the spectral index can only be calculated meaningful at pixels above the 1σ noise level, information

[3]At each pair of pixels of the two (coinciding) maps, the spectral index α is calculated from the flux densities per beam S_1 and S_2 at the two frequencies ν_1 and ν_2: $\alpha = (\lg S_1 - \lg S_2)/(\lg \nu_1 - \lg \nu_2)$

Table 4.7: Spectral index map parameters

ν_1 [Hz]	ν_2 [Hz]	Common Beam [mas × mas, °]	Lowest Contour$_1^a$ (mJy/beam)	Lowest Contour$_2^b$ (mJy/beam)	*Contours*$_3^c$ [(mJy/beam) × (levels)]
5	8.4	2.64 × 1.06, -3.805	2	2	(-2.5,-1.5,-0.5,0,0.5,1.5,2.5)
8.4	22	1.42 × 0.565, -5.75	1	1	(-2.5,-1.5,-0.5,0,0.5,1.5,2.5)
22	43	0.655 × 0.240, -7.78	1	1	(-2.5,-1.5,-0.5,0,0.5,1.5,2.5)

[a] Lowest contour in the low–ν map; [b] Lowest contour in the high–ν map; [c] Contours in the spectral index map.

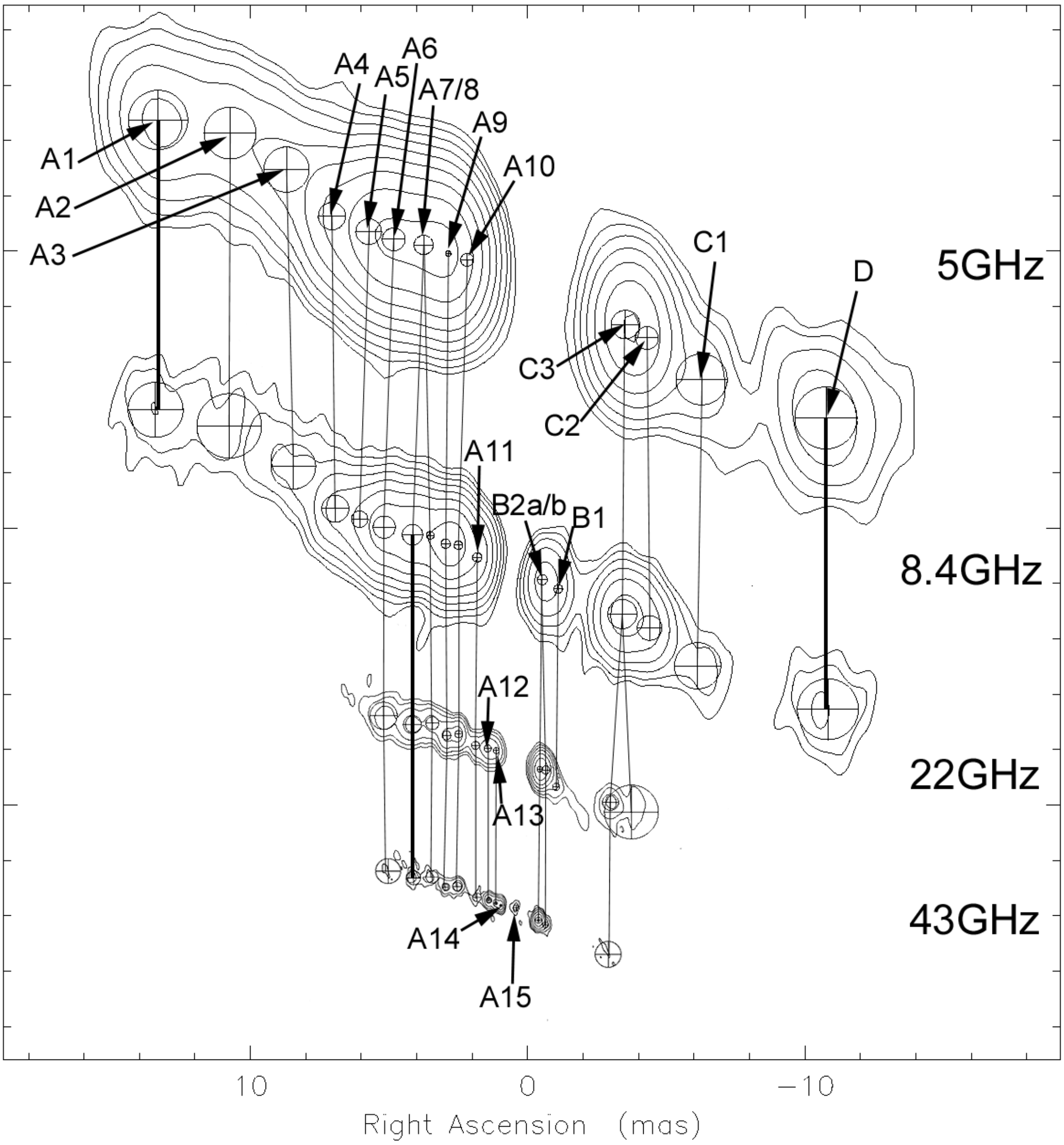

Figure 4.3: The aligned model fit maps. The circles represent the FWHM of the circular Gaussians. The vertical and oblique lines join the associated components between different frequencies. The components A1 and D between 5 and 8.4 GHz and A7 between 8.4, 22 and 43 GHz (joined by a thicker trace) were used for the alignment. The contours are 1.872 mJy × (-1,1,2,4,...,256) for the 5 GHz model, 2.62 mJy × (-1,1,2,4,...,128) for the 8.4 GHz model, 5.01 mJy × (-1,1,2,4,...,64) for the 22 GHz model and 3.45 mJy × (-1,1,2,4,...,32) for the 43 GHz model. The beams are 3.08 × 1.29 mas at 0.851° at 5 GHz, 1.95 × 0.806 mas at -3.97° at 8.4 GHz, 0.75 × 0.325 mas at -1.32° at 22 GHz and 0.385 × 0.161 mas at -2.62° at 43 GHz,

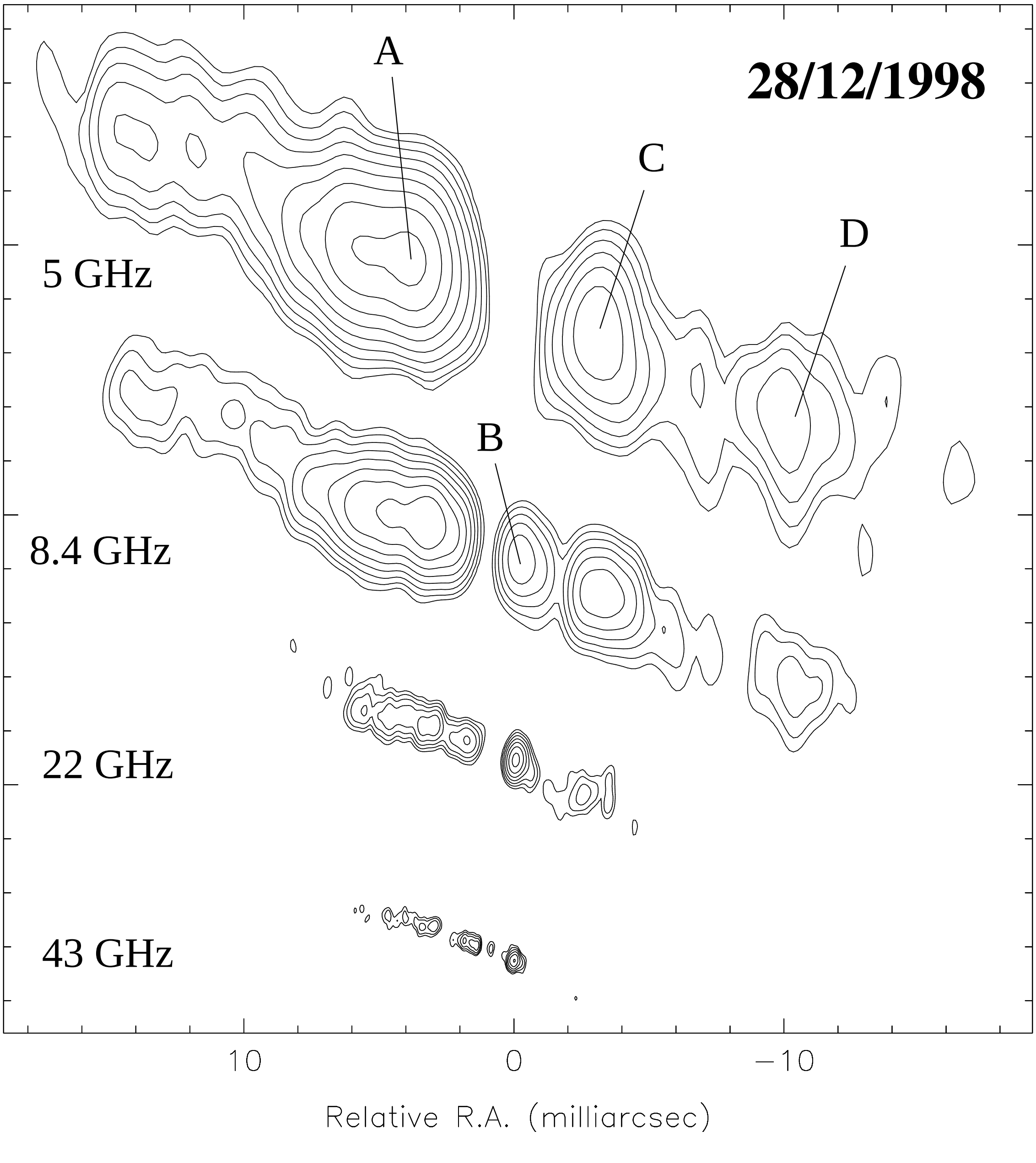

Figure 4.4: The aligned CLEAN maps. The contours are as given in Table 4.2, but without the two lowest contour levels. The beamsizes are the same as in Figure 4.1.

below 1 mJy/beam was discarded. This flux density threshold can introduce artifical features at the edges of the resulting spectral index map, which should not be interpreted as intrinsic source features.

A common slice through the spectral index maps was chosen (P.A. = 69.3°) to give a profile of the spectral index behaviour. This choice is in good agreement with the jet–axis at the inner part but a little too large in the outer part because of the curved jet structure. In order to avoid this it would be necessary to define a series of slice segments along the ridge line of the source. Nevertheless, the slice matches the jet axis at 5 GHz quite well and an examination of the spectral index maps shows that there are no unphysical trends visible, perpendicular to the slice. For this, the mismatching of the jet axis in the outer parts of the jet seems tolerable. The common–beam maps are shown pairwise in Fig 4.5 to 4.7 together with the spectral index maps. Additionally the figures show the course of the flux density and the value of the spectral index, respectively, along the slice. The latter were determined using the task SLICE in $\mathcal{AIPS}$.

The main feature in each spectral index map is an optically thick inner edge of the innermost part of both jets. Outwards, the spectral index tends to decrease but is superimposed by local extrema. Some of these are actually a composite of several blended lines making it difficult to judge the overall quality of the registration just by looking at the brightness cuts. Nevertheless, the inconsistencies in position are small and can be estimated to be of the order of ±1 map pixel (corresponding to 0.3,0.15 and 0.075 mas in the 5-8.4, 8.4-22 and 22-43 GHz map, respectively).

Between 5 GHz and 8.4 GHz the spectral index α diverges at the region of the components A11 and B2[4] (see Figure 4.5). The value of 2.5 is exceeded on both sides indicating a region of extrinsic absorption at the center of NGC 1052. The spectral index at the inner edge of the eastern jet, however, is affected by the tail of the B2 component which contributes to this region at 8.4 GHz due to the size of the beam. The position where this effect is negligible is indicated by the first kink in the eastern part of the spectral index slice around map pixel 120. At this point the spectral index is still above the theoretical maximum of 2.5 for self absorption but a small shift of the 5 GHz map to the east would probably drop it to values around 1. In the outer part of the eastern jet the spectral index oscillates around ~ -1, therefore being optically thin. The western jet also shows a decrease of the spectral index from ~ 2 at the region of C3 and C2 to ~ 1 around D.

Between 8.4 and 22 GHz (Figure 4.6) the spectral index in the eastern jet is extremely smooth between the regions of A5 and A11, followed by a very sharp rise towards A12 and A13 with values of α up to 3.5. On the western side there are also very high values of α but not larger than 2.5, not ruling out the possibility of external absorption but being compatible with internal self absorption of the jet core. Outwards in the western jet, there is a kink in the decrease of α which is again an artificial contribution of the optically thick components of the other jet side (A12 and A13), which tails are folded partially onto the western side. Behind this kink the spectral index keeps falling until it rises again very quickly at the inner edge of the region C. On the outer part of the C region α falls down below values of -1.

Between 22 and 43 GHz (Figure 4.7) the spectral index is fairly constant with values around -1.5 on the eastern side and a rise up to $+1.5$ from the region of the component

[4]In this section the components A1 to D serve just as a way to describe a special region in the source. "The region around C", e.g. means the part of the western jet between 2 and 8 mas from the gap.

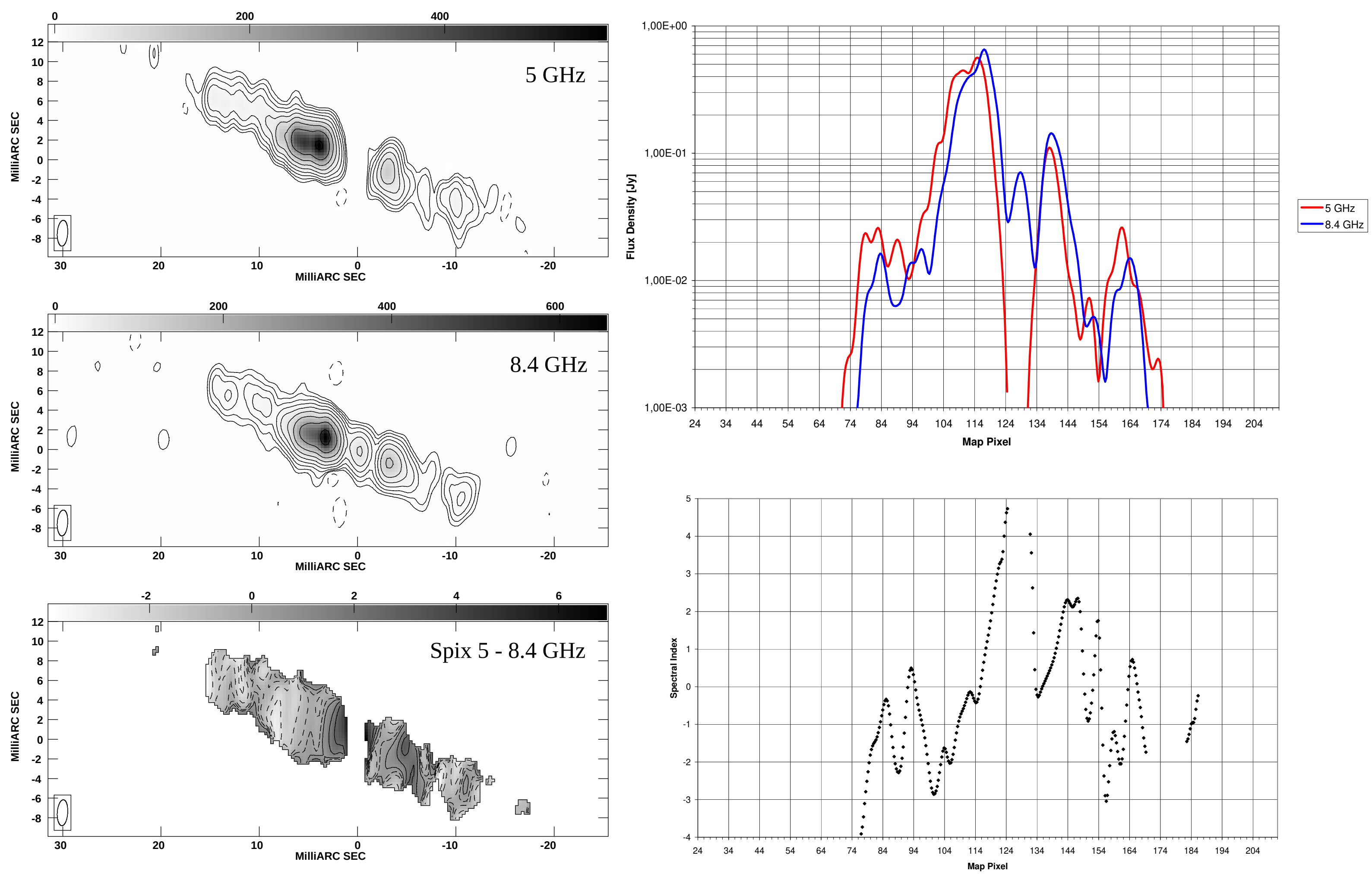

Figure 4.5: Left hand side: Total intensity maps of NGC 1052 at 5 GHz and 8.4 GHz (top) restored with a common beam and the spectral index map between 5 and 8.4 GHz (bottom). The contours and beam parameters are given in Table 4.7. Right hand side: The course of the brightness (top) and the spectral index (bottom) along a P.A. of 69.3° (top left corner to bottom right cornor of the images on the left side.

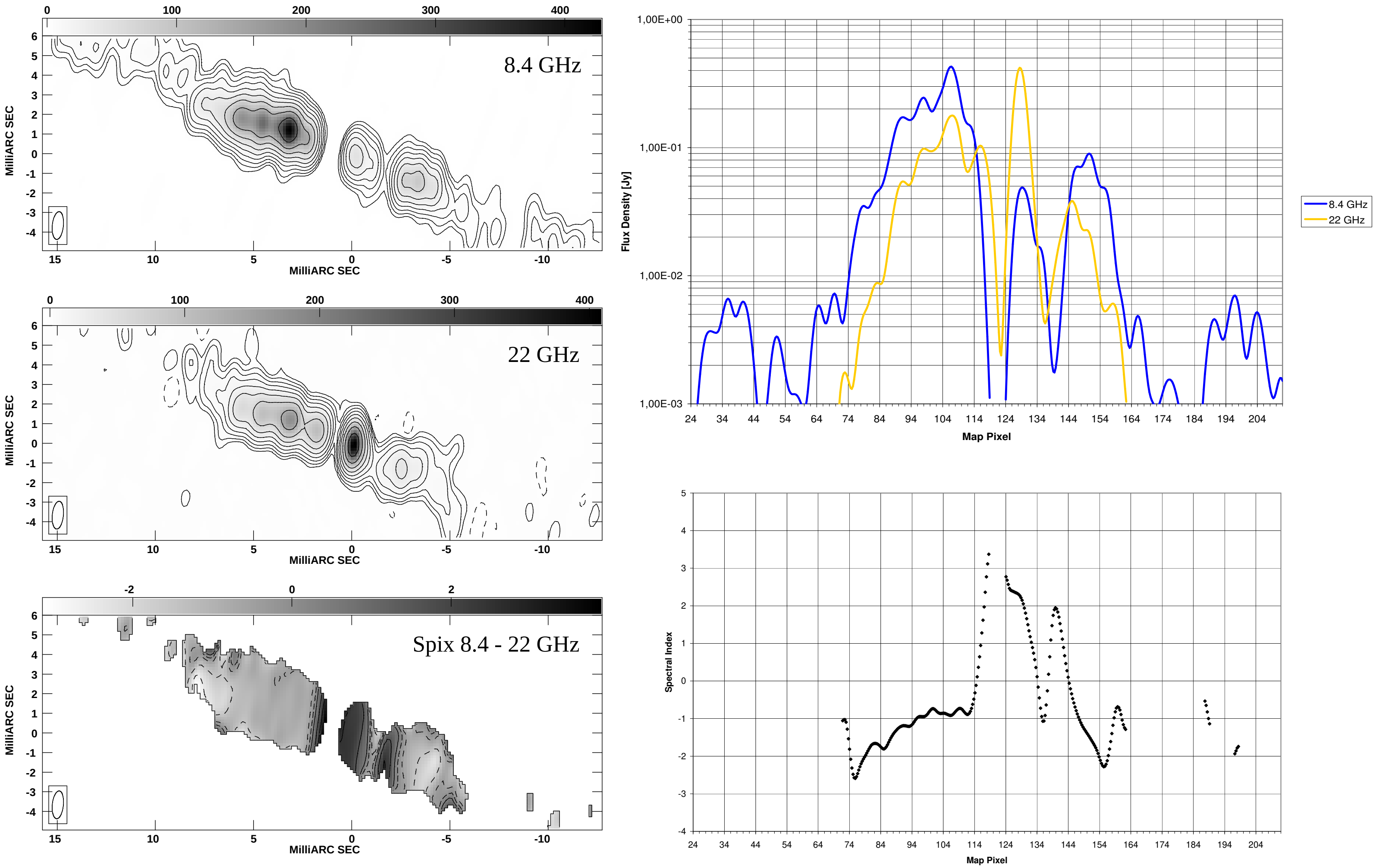

Figure 4.6: Left hand side: Total intensity maps of NGC 1052 at 8.4 and 22 GHz (top) restored with a common beam and the spectral index map between 8.4 and 22 GHz (bottom). The contours and beam parameters are given in Table 4.7. Right hand side: The course of the brightness (top) and the spectral index (bottom) along a P.A. of 69.3° (top left corner to bottom right cornor of the images on the left side.

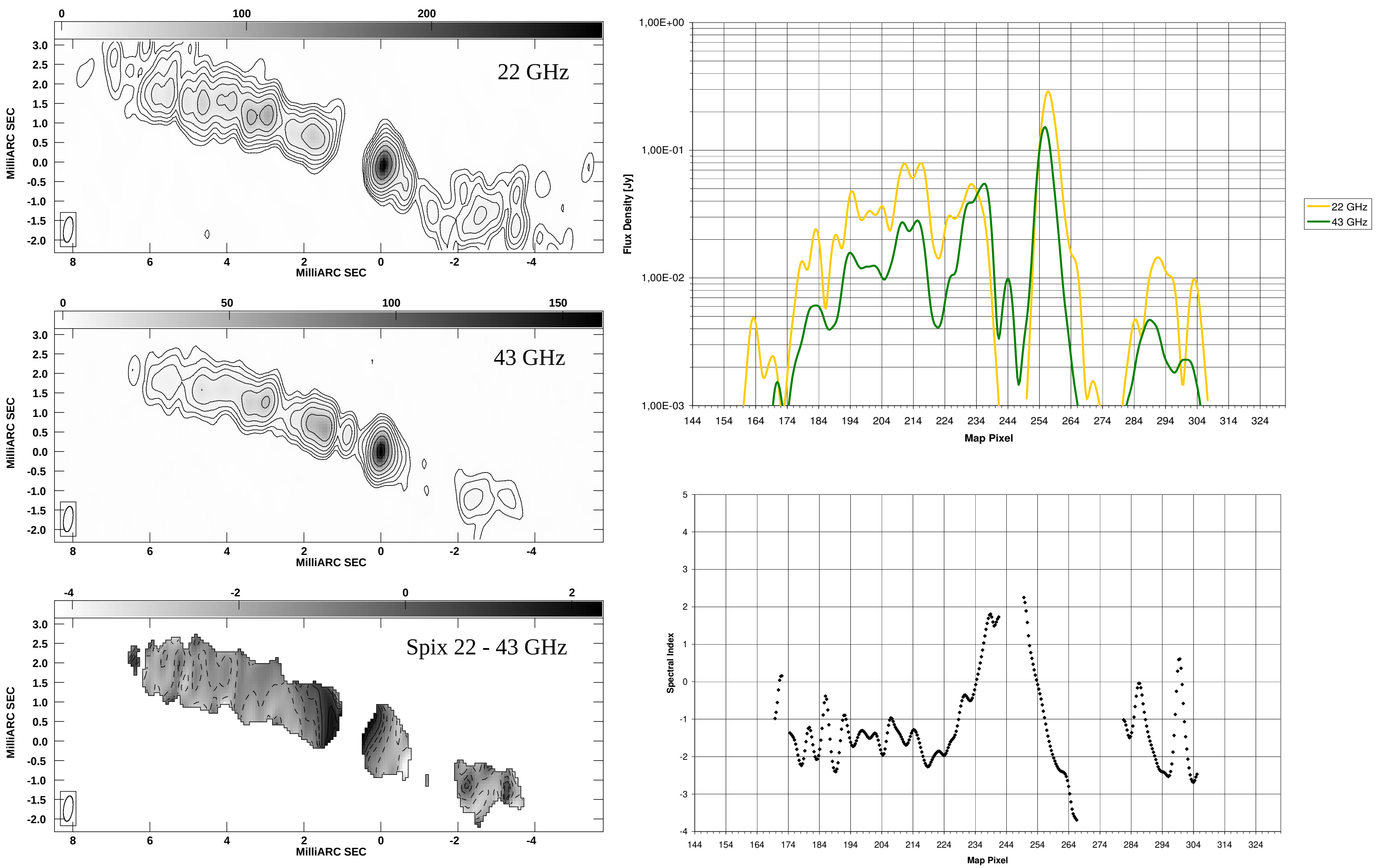

Figure 4.7: Left hand side: Total intensity maps of NGC 1052 at 22 and 43 GHz (top) restored with a common beam and the spectral index map between 22 and 43 GHz (bottom). The contours and beam parameters are given in Table 4.7. Right hand side: The course of the brightness (top) and the spectral index (bottom) along a P.A. of 69.3° (top left corner to bottom right cornor of the images on the left side.

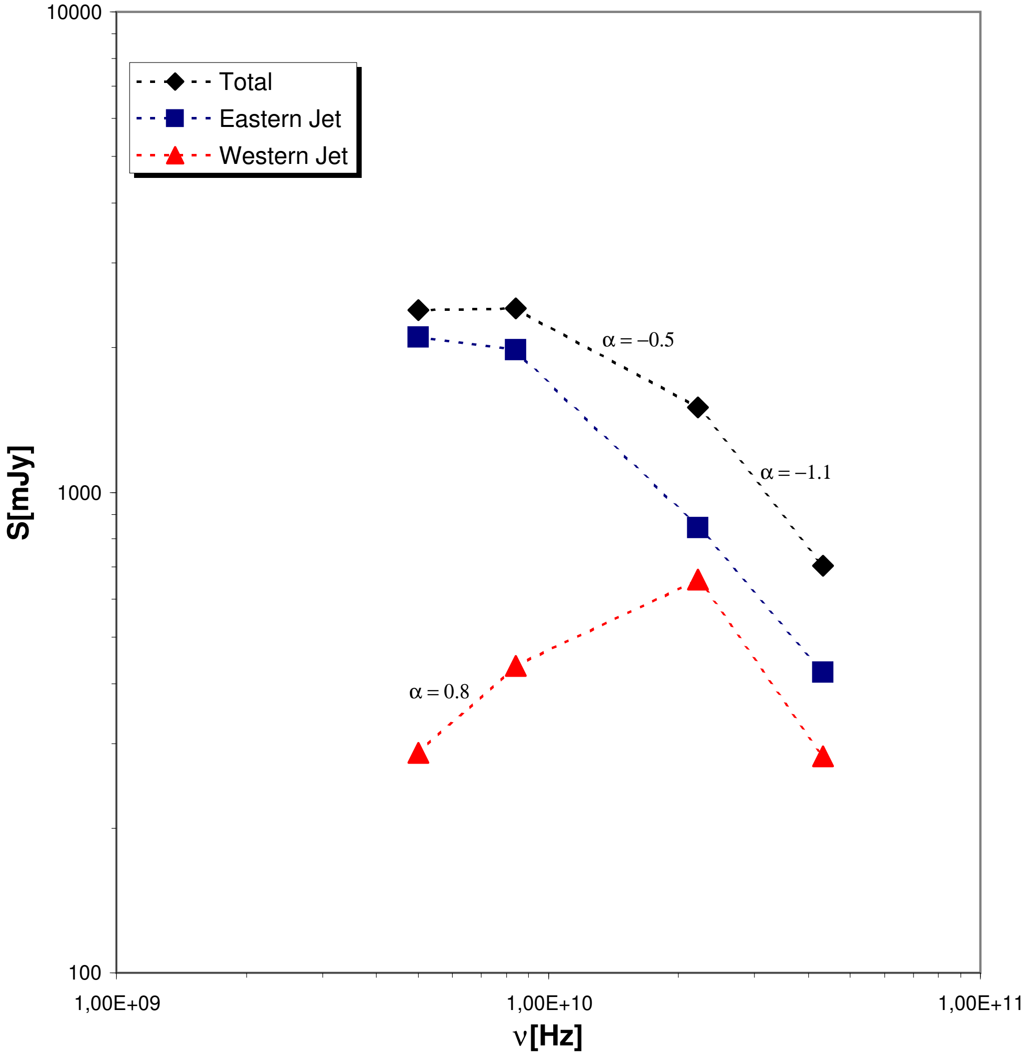

Figure 4.8: Total spectrum of the pc-scale structure of NGC 1052 (as imaged with VLBI) and the two jet spectra between 5 and 43 GHz. No errors are given, since these are negligible small.

A12 inwards. On the western side α rises from the outer edge of component B to its inner edge from values below -2 approaching 2.5 but not exceeding it. In the region around component C the spectral index falls from -1 to -2.5 going outwards with two peaks inbetween.

The influence of external absorption on the the western jet is undisputable since no counterpart of the B2 component is present at 5 GHz. The structure of the eastern jet is rather continuous with no strong and isolated components at its inner part. The data however, indicate a region of external absorption, comparable in extend to the western side. In sum, there are hints for the presence of an obscuring torus or thick disk from the analysis of the spectral index maps, which covers the core of the western jet but also a substantial fraction of the inner eastern jet.

Spectral analysis of the model fit components The flux densities of the model fit components in Table 4.3 to 4.6 can be used to derive spectra of 1) the whole pc-scale structure, 2) the two jets separately and 3) the model fit components themselves. In Figure 4.8 the total spectrum of the pc-scale structure of NGC 1052 between 5 and 43 GHz is shown as well as the spectra of both jets separately. All values were obtained by adding up flux densities[5] of model components (A1 to A15 for the eastern jet and B2b to D for the western one). Components that are not found at a special frequency were given the flux density zero.

At the high frequencies both jets show similar spectra with an optically thin decrease of the flux density above 22 GHz. The spectral index in this regime is around -1 in both jets, with the eastern jet being significantly stronger than the western one. This implies that the eastern jet is the approaching one whereas the western jet is the counterjet. However, below 22 GHz the behaviour of the two spectra differs substantially. The eastern jet spectrum remains optically thin above 8.4 GHz and turns over around 5 GHz. The western jet, on the other hand exhibits a sharp cut–off in its spectrum below 22 GHz with the spectrum becoming even more inverted below 8.4 GHz. Although the spectral index is not above 2.5 the possibility of synchrotron self-absorption seems very unlikely to be responsible for the turnover of the spectrum because of two reasons. First, the similarity of the spectra of eastern and western jet at high frequencies proposes similar intrinsic physical properties on both sides making it suspicious that the self absorption frequency differs by at least a factor of 3. Second, the kinematical analysis of Vermeulen et al. (2002) shows the jet axis to be close to the plane of the sky and the motions to be only weakly relativistic. There is little evidence for strong Doppler boosting. Moreover, such an effect should shift the turnover frequency of the counterjet to lower frequencies, rather than to higher ones.

If the spectrum of the western jet is decomposed into the spectra of the different jet regions A, B, C and D (see Figure 4.9) it turns out, that the region B, the innermost region on the western side, is responsible for the cut–off of the western jet spectrum below 22 GHz. Its spectrum between 8.4 and 22 GHz is highly inverted with a spectral index of 1.9 but the fact that it is not detectable at all at 5 GHz makes the spectral index in this regime larger than 4. Such big positive spectral indices cannot be due to synchrotron self absorption but indicate a region of external absorption in front of the source. The spatially isolated position of this component rules out arguments dealing with misregistration effects and makes this case one of the most pronounced external absorption effect in extragalactic radio sources. The highly inverted spectrum of this component in NGC 1052 and the necessity of an external absorber was first mentioned by Kellermann et al. (1999) and later confirmed by Kameno et al. (2001). Other sources in which evidence for an central free-free absorber was found are e.g., Cen A (Tingay & Murphy 2001), NGC 1275 (Vermeulen et al. 1994), NGC 4261 (Jones et al. 2000) and 0108+388 (Marr et al. 2000).

One open question at this point is, whether the eastern jet is also affected by external absorption or not. Kameno et al. proposed an obscuring torus, covering 0.7 mas of the western jet and 0.1 mas of the eastern jet. However, their results are very sensitive to shifts in the registration of the multi-frequency maps. Figure 4.10 shows the spectra of the model fit components of the eastern jet. Most components show optically thin synchrotron spectra with spectral indices around -1. The outer components A1, A2, A3, A4 and A5 show typically optically thin spectra and become too dim to be detected at

[5]For all quantities that are derived from the model component flux densities, a standard error calculation has been performed. The calculated errors are indicated in the plots, where they are not negligible.

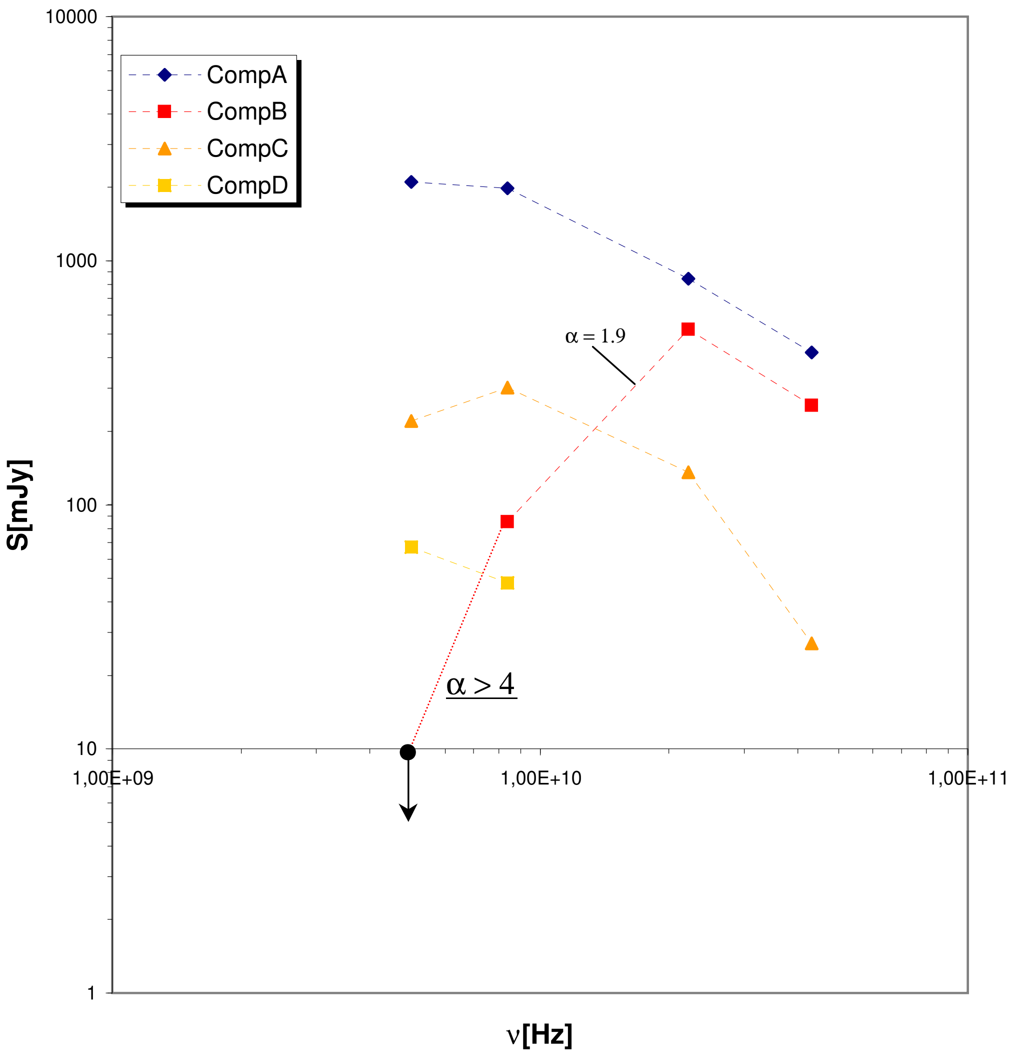

Figure 4.9: The spectra of the four jet regions A,B,C and D (see Figure 4.1 for the definition of the jet regions). No errors are given, since these are negligible small.

frequencies above 8.4 GHz. The very flat spectral index of some spectra (e.g. A6, A9) below 8.4 GHz indicates a turnover of the spectrum around 5 GHz. There is a general trend of the turnover of the components spectra to be shifted to lower frequencies the farther from the core a component is located. A12 and A13, e.g. are (self-) absorbed at low frequencies and seem to have their turnover close to 43 GHz.

The A11 counterpart is not detected at 5 GHz. Estimating (conservatively) a flux density of 10 mJy at 5 GHz yields a spectral index of 5. This would suggest that the innermost part of the eastern jet is also strongly affected by external absorption. However, the A10 and A11 components are very close to each other. If both flux densities are summed up at 5 and 8.4 GHz, a spectral index of 2.3 can be calculated, a value very close to the expected one for pure synchrotron self-absorption. Due to the small distances between the inner components in the eastern jet it cannot finally be judged, whether free-free absorption plays an important role or not. In Figure 4.11 the formal spectral indices of the components in the eastern jet are shown as a function of distance along the jet.

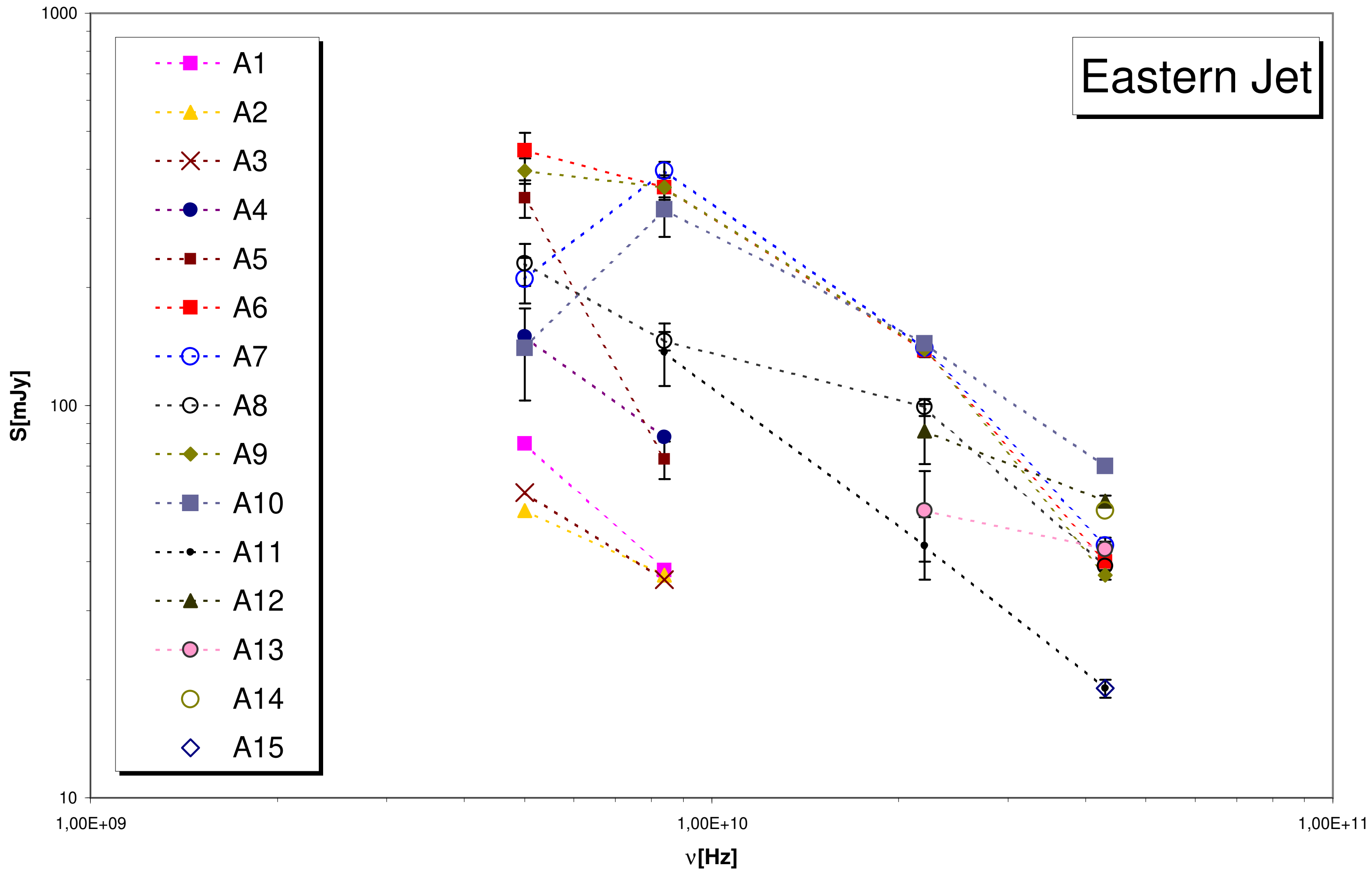

Figure 4.10: Spectra of the model fit components in the eastern jet (see Figure 4.3 for the locations of the various components). Errorbars for the components A5 to A13 are given. For the remaining components the errors are negligible.

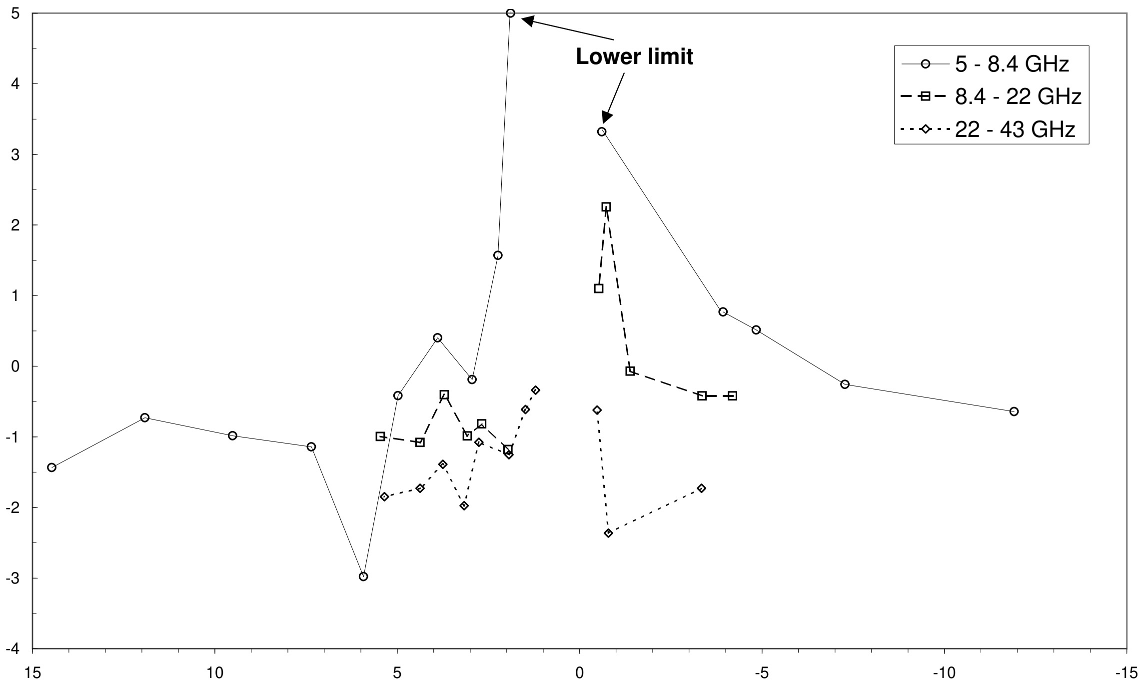

Figure 4.11: The spectral indices of the model components between 5 and 8.4 GHz, 8.4 and 22 GHz, as well as between 22 and 43 GHz (compare to Figure 4.5 to 4.7). Lower limits for the spectral indices between 5 and 8.4 GHz of the two innermost components at 8.4 GHz (B2a/b and A11), calculated from an upper limit of 10 mJy flux density at 5 GHz, are shown.

Their errors have been calculated from the formal errors of the model components, using a standard error calculation. A comparison with Figure 4.5 to 4.7 gives a good qualitative agreement to the slices through the spectral index maps of NGC 1052.

From the model fitted flux densities of both jets the jet-to-counterjet ratio of NGC 1052 can be determined. Figure 4.12 shows the ratio of the flux densities of the model components on either side of the gap as a function of frequency. At 5 GHz the eastern jet outshines the western one by a factor of 7.34. At 8.4 GHz it is still brighter than the counterjet by a factor of 4.56 but falls close to unity at 22 GHz. At 43 GHz the ratio rises again to 1.5. This behaviour is quite untypicall as in other similar sources (e.g. in Cygnus A) the ratio at 5 GHz is rather small increasing towards higher frequencies and reaching a maximum, before it finally falls again. The maximum is usually explained by resolution effects of the central absorber. At low frequencies the obscured area of the counterjet is unresolved so the obscuration has no net impact on the intrinsically frequency-independent jet-to-counterjet ratio. With rising frequency the obscuration has a bigger influence, as the resolution increases and the obscured area becomes resolved. At even higher frequencies the frequency dependence of free-free absorption makes the absorber partially transparent and the jet-to-counterjet ratio falls back to its initial value (which may differ from unity, due to boosting effects). This picture can explain the rise (or at least the stopped decrease) of R above 22 GHz, implying that the absorber covers a large fraction of the counterjet at 5 GHz. This is no surprise since component B is totally absorbed at 5 GHz. More surprising is the fact that the jet-to-counterjet even keeps rising at lower frequencies up to 50 at 2.3 GHz (Kameno et al. 2001). This suggests that either a much bigger part of the western jet is covered by the absorber or that curvature effects

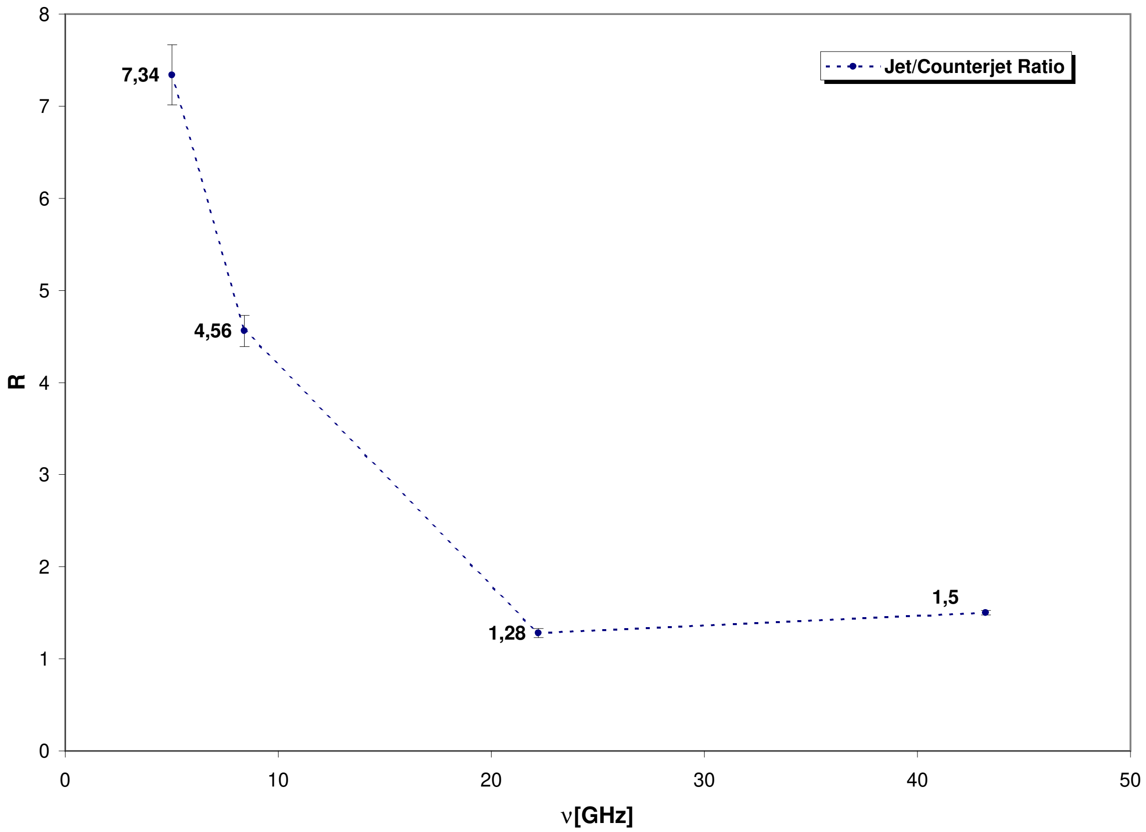

Figure 4.12: The jet-to-counterjet ratio determined from the fluxes of the model fit components as a function of frequency

play an important role. In the first scenario the density of the absorber falls fast enough with radius that at 5 GHz the absorber has become optically thin a few milliarcseconds from the core and component C is only weakly absorbed. In the latter case, the counterjet bends away from the observer at a distance of a few milliarcseconds from the core and its radiation is Doppler de–boosted.

4.4 Brightness temperature distribution

In this section a method of analyzing the brightness temperature distribution along a jet is presented and applied to the eastern jet of NGC 1052. This method provides a tool to find regions in a jet which are affected by external absorption. In the inner region of the eastern jet of NGC 1052 this method unveils the existence of an obscuring torus and sets limits to its geometrical extent and density.

The brightness temperature of a source is defined as the temperature of a blackbody, producing the same flux density at the measured frequency as the source. For a non-thermal source the brightness temperature is a frequency-dependent quantity. From this definition follows (see e.g. Condon et al. 1982)

$$T_b = \frac{1}{\pi r^2}\frac{c^2 S_\nu}{2k_B\nu^2} = 1.22\cdot 10^{12}\mathrm{K}\left(\frac{S_\nu}{\mathrm{Jy}}\right)\left(\frac{\nu}{\mathrm{GHz}}\right)^{-2}\left(\frac{\Theta}{\mathrm{mas}}\right)^{-2} \tag{4.1}$$

with S_ν the flux density of the source, ν the observing frequency, r the diameter of the source and Θ its apparent diameter at half maximum[6]. According to this equation, brightness temperatures have been computed for the model fit components at all four frequencies. The resulting values are given in Table 4.8 to 4.11. The uncertainties in T_b were computed using Gaussian error propagation from the errors in flux density and FWHM of the model components (see Table 4.3 to 4.6). In Figure 4.13 the brightness temperatures of the eastern jet are plotted as a function of distance from the central engine. Once again, this was assumed to lie at the center between the components A15 and B2b (see Section 4.6 for a detailed discussion).

On both sides of the gap there is a substantial rise of T_b towards the center, but on the eastern side there is a conspicuous cut–off around 3 mas from the center (dashed line in Figure 4.13). This cut–off is present at all four frequencies although the inner components (only visible at 22 and 43 GHz) exhibit again a rise in T_b even above the cut–off value. The value of the innermost component A15 falls significantly below the extrapolation of the curve defined by A12, A13 and A14.

In the logarithmic plot of the brightness temperature distribution along the eastern jet (Figure 4.13) the data points above the cut–off can well be approximated with a straight line[7]. A linear regression of the form $\log(T_b/10^9\,\mathrm{K}) = A + B \cdot \log(r/1\,\mathrm{mas})$ (see Table 4.12 for the fitted parameters A and B, as well as the theoretical brightness temperatures T_b^{theo} from the fitted relation) was performed. The quantity B determines the slope of the regression line in Figure 4.13. A is a measure for the offset between the four lines at the four frequencies. Physically, A is the brightness temperature in units of 10^9 K of a component at a distance of 1 mas, assuming the validity of a linear extrapolation of $\log T_b$. The application of the linear regression gives at all four frequencies very similar dependences of T_b on approximately the -4th power of the radius, a result that constrains the turnover frequency distribution along the jet:

Table 4.8: Brightness temperatures and related parameters at 5 GHz

Component	$T_b[10^9\mathrm{K}]$	$T_b^{\mathrm{theo}}[10^9\mathrm{K}]^{\mathrm{a}}$	τ
D	0.96 ± 0.03	–	–
C1	0.50 ± 0.03	–	–
C2	6.17 ± 0.74	–	–
C3	9.30 ± 0.58	–	–
A10	$(47.64 \pm 13.61)^{\mathrm{b}}$	1192.73 ± 131.57	3.22 ± 0.29
A9	714.60 ± 255.87	388.91 ± 38.14	-0.61 ± 0.12
A7/8	66.54 ± 8.80	126.61 ± 10.73	0.64 ± 0.11
A6	46.72 ± 11.81	46.78 ± 3.34	0.0 ± 0.1
A5	28.14 ± 8.17	23.16 ± 1.41	-0.19 ± 0.13
A4	11.02 ± 0.56	9.64 ± 0.45	-0.13 ± 0.07
A3	1.63 ± 0.07	3.40 ± 0.09	0.74 ± 0.04
A2	1.11 ± 0.06	1.368 ± 0.01	0.21 ± 0.04
A1	1.26 ± 0.04	0.624 ± 0.007	-0.7 ± 0.03

[a] Theoretical brightness temperatures, calculated from a power–law fit of the measured values farther out than 3 mas along the eastern jet.
[b] Values in brackets are not used for the power–law fit.

Along a jet the flux density is proportional to $(\nu - \nu_t)^\alpha$ with ν fixed. If the turnover

[6] This corresponds to the FWHM of a circular Gaussian model component.

[7] No detailed examination of the brightness temperature distribution along the western jet is presented, since this suffers from the large gaps between the components and their small number.

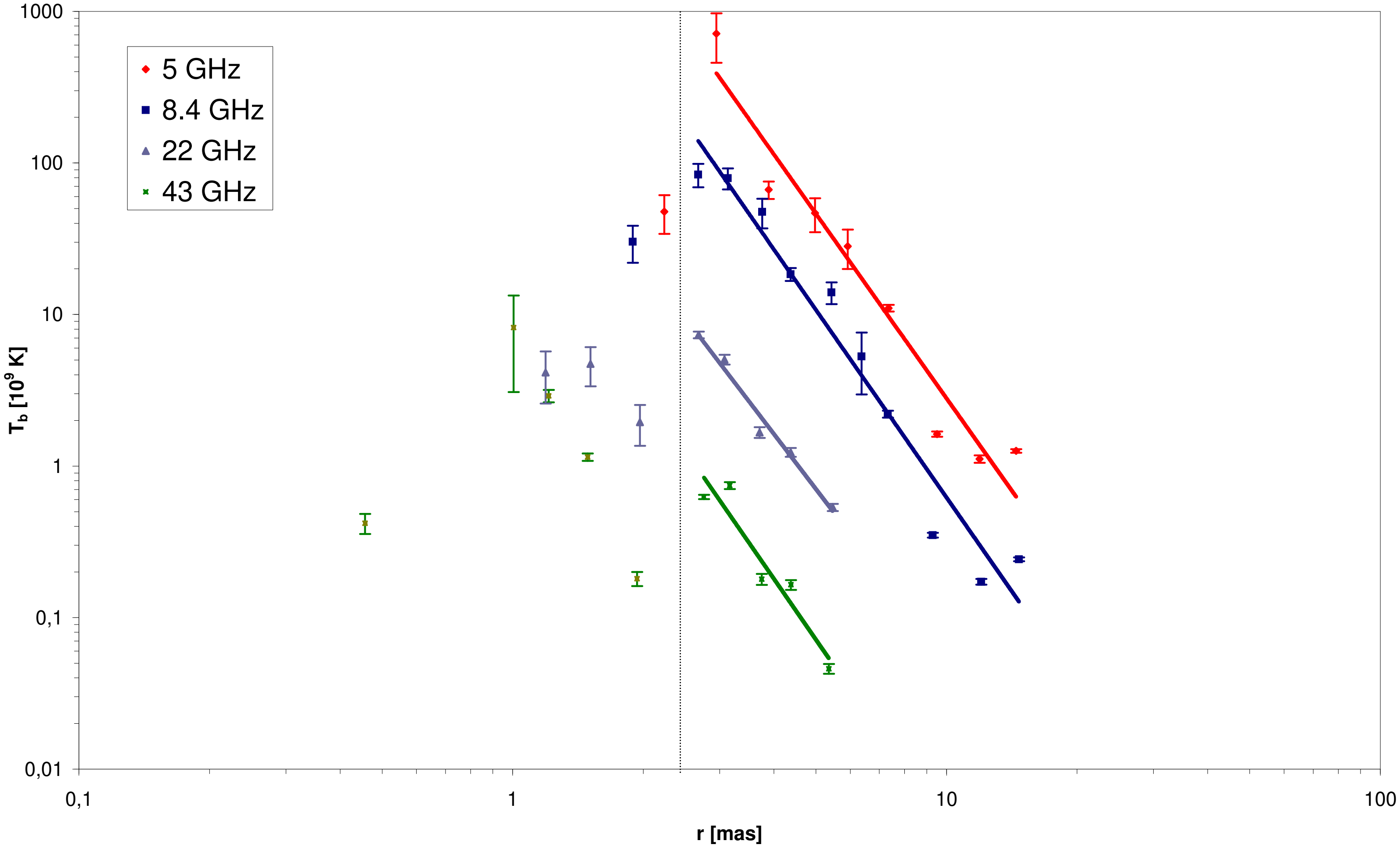

Figure 4.13: Logarithmic representation of the brightness temperature distribution along the eastern jet of NGC 1052. Above the cut–off distance the data can be fitted by a straight line (see Table 4.12 for the linear regression parameters) with a slope of ~ -4. The offset between the four data sets of brightness temperatures reflects the frequency dependence of T_b (see 4.1).

Table 4.9: Brightness temperatures and related parameters at 8.4 GHz

Component	$T_b[10^9\mathrm{K}]$	$T_b^{\mathrm{theo}}[10^9\mathrm{K}]^{\mathrm{a}}$	τ
D	0.251 ± 0.008	–	–
C1	0.19 ± 0.01	–	–
C2	2.43 ± 0.27	–	–
C3	4.63 ± 0.35	–	–
B1	7.70 ± 0.73	–	–
B2a/b	11.02 ± 1.00	–	–
A11	$(30.23 \pm 8.32)^{\mathrm{b}}$	590.18 ± 43.64	2.97 ± 0.2
A10	83.88 ± 14.88	141.47 ± 8.69	0.52 ± 0.16
A9	79.44 ± 12.57	74.30 ± 4.11	-0.07 ± 0.08
A8	47.51 ± 10.51	35.03 ± 1.68	-0.3 ± 0.07
A7	18.45 ± 1.81	18.82 ± 0.77	0.02 ± 0.07
A6	14.00 ± 2.31	7.72 ± 0.23	-0.6 ± 0.08
A5	5.28 ± 2.31	4.01 ± 0.09	-0.27 ± 0.11
A4	2.20 ± 0.12	2.26 ± 0.03	0.02 ± 0.05
A3	0.35 ± 0.01	0.849 ± 0.002	0.89 ± 0.03
A2	0.172 ± 0.008	0.294 ± 0.007	0.53 ± 0.04
A1	0.242 ± 0.007	0.129 ± 0.005	-0.63 ± 0.05

[a] Theoretical brightness temperatures, calculated from a power–law fit of the measured values farther out than 3 mas along the eastern jet.
[b] Values in brackets are not used for the power–law fit.

Table 4.10: Brightness temperatures and related parameters at 22 GHz

Component	$T_b[10^9\mathrm{K}]$	$T_b^{\mathrm{theo}}[10^9\mathrm{K}]^{\mathrm{a}}$	τ
C3b	0.08 ± 0.01	–	–
C3a	0.55 ± 0.05	–	–
B1	1.28 ± 7.26	–	–
B2a	6.68 ± 0.77	–	–
B2b	28.76 ± 1.81	–	–
A13	$(4.15 \pm 1.56)^{\mathrm{b}}$	153.54 ± 6.27	3.61 ± 0.26
A12	$(4.73 \pm 1.37)^{\mathrm{b}}$	62.80 ± 2.19	2.59 ± 0.18
A11	$(1.95 \pm 0.59)^{\mathrm{b}}$	23.46 ± 0.67	2.49 ± 0.18
A10	7.35 ± 0.37	7.31 ± 0.15	0.00 ± 0.04
A9	5.05 ± 0.38	4.38 ± 0.07	-0.14 ± 0.05
A8	1.67 ± 0.14	2.17 ± 0.02	0.27 ± 0.05
A7	1.23 ± 0.08	1.17 ± 0.002	-0.05 ± 0.05
A6	0.53 ± 0.03	0.508 ± 0.004	-0.05 ± 0.04

[a] Theoretical brightness temperatures, calculated from a power–law fit of the measured values farther out than 3 mas along the eastern jet.
[b] Values in brackets are not used for the power–law fit.

frequency ν_t varies as r^{-t}, with $t \geq 1$, a component further out is expected to have a lower flux density since the observing frequency is farther from the turnover frequency than for a component which is located at a smaller distance r. The flux density thus varies as $S_\nu \propto (r^{-t})^\alpha = r^{\alpha-t}$. If the jet has a constant opening angle, the diameters θ of the model components vary as $\theta \propto r$, leading to an overall dependence of $T_b \propto r^{\alpha-t-2}$ of the brightness temperature on the distance from the center of jet activity. The spectral indices of the model components in the eastern jet scatter around -1 (see Figure 4.11). The measured dependence of T_b on the -4th power of r thus implies, that $t = 1$ (assuming, that the jet–axis lies in the plain of the sky, as suggested by the kinematical studies at 2 cm by Vermeulen et al. 2002), i.e. the turnover frequency varies as $\nu_t \propto r^{-1}$ along the eastern jet.

The linear regression fit parameters to the brightness temperatures as a function of

Table 4.11: Brightness temperatures and related parameters at 43 GHz

Component	$T_b[10^9\mathrm{K}]$	$T_b^{\mathrm{theo}}[10^9\mathrm{K}]^{\mathrm{a}}$	τ
C3b	0.029 ± 0.003	–	–
B2a	0.62 ± 0.05	–	–
B2b	4.37 ± 0.05	–	–
A15	$(0.42 \pm 0.06)^{\mathrm{b}}$	1446.63 ± 233.72	8.15 ± 0.17
A14	$(8.21 \pm 5.14)^{\mathrm{b}}$	55.08 ± 4.24	1.90 ± 0.08
A13	$(2.91 \pm 0.28)^{\mathrm{b}}$	25.55 ± 1.60	2.17 ± 0.08
A12	$(1.15 \pm 0.07)^{\mathrm{b}}$	10.86 ± 0.52	2.25 ± 0.06
A11	$(0.18 \pm 0.02)^{\mathrm{b}}$	3.65 ± 0.10	3.01 ± 0.06
A10	0.63 ± 0.02	0.839 ± 0.004	0.29 ± 0.01
A9	0.74 ± 0.04	0.476 ± 0.009	-0.45 ± 0.03
A8	0.18 ± 0.01	0.236 ± 0.009	0.28 ± 0.06
A7	0.16 ± 0.01	0.125 ± 0.007	-0.28 ± 0.07
A6	0.046 ± 0.003	0.054 ± 0.005	0.16 ± 0.10

[a] Theoretical brightness temperatures, calculated from a power–law fit of the measured values farther out than 3 mas along the eastern jet.
[b] Values in brackets are not used for the power–law fit.

Table 4.12: Linear regression parameters for the brightness temperature distribution along the eastern jet. The linear regression was applied to the values of $\log T_b$ as a function of $\log r$: $\log(T_b/10^9\,\mathrm{K}) = A + B \cdot \log(r/1\,\mathrm{mas})$.

Frequency	A	B
5 GHz	4.49±0.33	-4.05 ± 0.39
8.4 GHz	3.91±0.25	-4.11 ± 0.31
22 GHz	2.47±0.19	-3.75 ± 0.32
43 GHz	1.75±0.44	-4.14 ± 0.75

distance from the jet origin can be used to examine the frequency dependence of the determined T_b-data sets. From Equation (4.1) a dependence of $T_b \propto \nu^{-2+\overline{\alpha}}$ is expected, with an average spectral index $\overline{\alpha}$ along the jet. To analyze the dependence of A with frequency a linear regression of the form $A = A' + B' \cdot \log(\nu/1\,\mathrm{Hz})$ was performed. This gave $B' = -3.02 \pm 0.14$ implying a dependence of $T_b \propto \nu^{-3.02\pm0.14}$. The best value for the average spectral index is thus $\alpha_{mean} = -1.02 \pm 0.14$. The plot of the linear regression in Figure 4.14 demonstrates the quality of the fit and shows that -1 is a reasonable estimate of the intrinsic spectral index along the eastern jet of NGC 1052. Therefore, the energy distribution of the electrons follows a power-law with an index of $s_{mean} = 1 - 2\alpha_{mean} = 3.04 \pm 0.28$.

If the maximal brightness temperature of the jet were constant along the jet, a set of measurements of T_b and the spectral indices α of the model components could be used to derive the precise turnover frequency distribution in the jet. As a natural choice for the maximal T_b, the cut–off brightness temperature measured at 5 GHz can be used. For each component a factor can be calculated, by which the measured value of T_b has to be multiplied to reach the maximal value. The small value measured for T_b can be attributed to the shape of the corresponding model component spectrum. Assuming an optically thin spectrum with a spectral index α measured at the corresponding frequency, the turnover frequency (at which the maximal value should be reached) can be calculated from the correction factor. The application of this idea leads to a turnover frequency distribution along the jet for each frequency data set. However, offsets between the four curves reflect the fact that the maximal brightness temperature along the eastern jet of NGC 1052 is

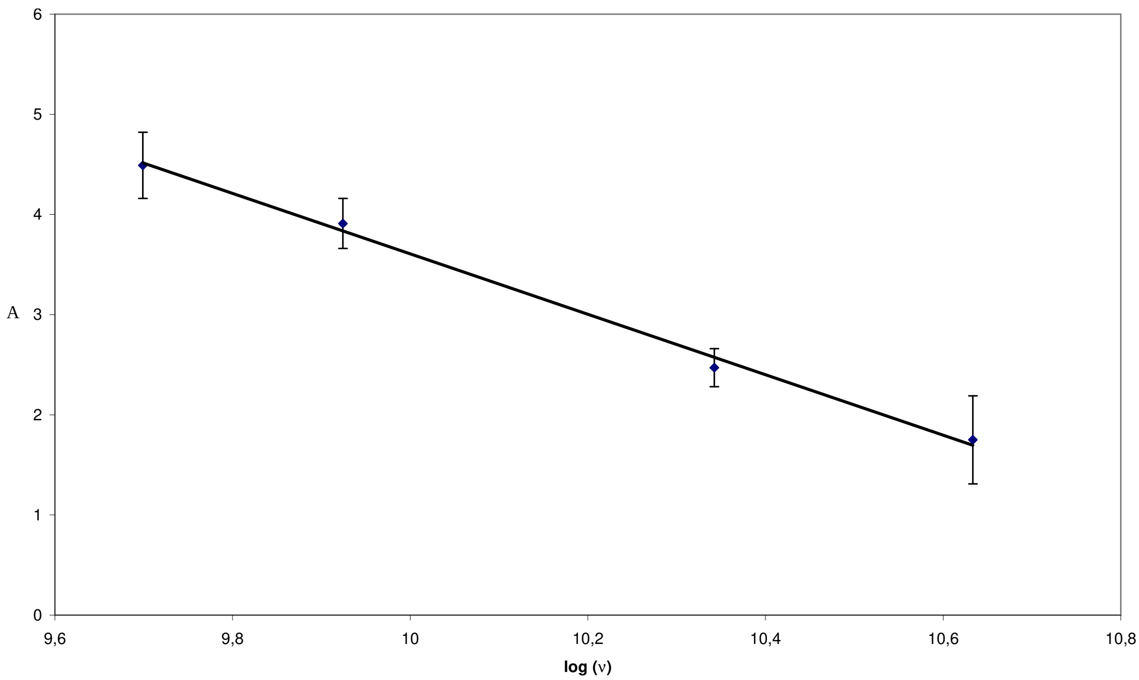

Figure 4.14: Frequency dependence of the brightness temperatures in the eastern jet of NGC 1052. The value of A ($\hat{=} \log T_b(r = 1\,\mathrm{mas})$ assuming a linear extrapolation of the linear regression line) is plotted as a measure for the relative offset between the four T_b-data sets as a function of frequency. The fitted dependence of $r^{-3.02\pm0.14}$ indicates an average spectral index of ~ -1 along the eastern jet (see text).

not constant. It is not possible to find a consistent model with just one maximal value of T_b, i.e., there is an evolution of the maximal brightness temperature with distance. A more detailed model of this evolution should in principle be able to reproduce consistent values of ν_t, from all four data sets, but this will be kept for later efforts.

The frequency–independence of the cut–off distance of 3 mas implies an external effect suggesting that at this position the influence of the nuclear absorber starts to affect substantially the jet and the brightness temperature of its components. This suggests the presence of an obscuring torus around the central engine of NGC 1052 with a sharp edge, rather than a circumnuclear cloud system. To check this hypothesis it was tested if the free-free absorber model can cause the observed cut–off in the brightness temperature distribution. In the case of free-free absorption, the observed flux density $S_{\nu,\mathrm{abs}}$ should depend on the intrinsic flux density S_ν, the optical depth of the absorber τ_f and the observing frequency ν as

$$S_{\nu,\mathrm{abs}} = S_\nu \cdot e^{-\tau_f} \tag{4.2}$$

From this equation, the optically depth of the absorber, needed to change the theoretical value (extrapolation of the linear regression line) to the measured one, can be calculated. This calculation can be done for A10 at 5 GHz, for A11 at 8.4 GHz, for A11, A12 and A13 at 22 GHz, and finally for A11, A12, A13, A14 and A15 at 43 GHz. The calculated values are given in Table 4.13. At each of the three highest frequencies it turns out that the resulting values for τ_f are very similar within one dataset except the one for the innermost component which has a significantly higher optically depth. This larger value can be explained in terms of additional synchrotron self absorption, so that the measured optically depth is a superposition of two distinct contributions $\tau = \tau_f + \tau_s$, expected at the most compact component in a jet.

Assuming an absorbing pathlength of 0.3 pc (comparable to the extent of the absorbing region in the plane of the sky), the obtained opacities constrain the physical properties in the torus. Equation (2.28) can be simplified to

$$\begin{aligned} \tau_f &= 30 \cdot 10^{16}\, L\, T^{-1.35}\, \nu^{-2.1}\, \overline{n}^2 \\ \Rightarrow \quad T^{-1.35}\, \overline{n}^2 &= 3.33 \cdot 10^{-18}\, L^{-1} \tau_f\, \nu^{2.1} \end{aligned}$$

with a length $L = \int dl$ and an average density $\overline{n}$. For $\tau_f \sim 2.5$ at $\nu = 22\,\mathrm{GHz}$ at a temperature of $T = 10^4\,\mathrm{K}$, this results to a density of $\overline{n} = 6 \cdot 10^5\,\mathrm{cm}^{-3}$ and an absorbing column density of $5.6 \cdot 10^{22}\,\mathrm{cm}^{-2}$. This value is consistent with the implications of the X-ray observations of NGC 1052, which find a (model-dependent) column density of 10^{22}-$10^{23}\,\mathrm{cm}^{-2}$ towards the unresolved nuclear X-ray core (Appendix D; compare also Weaver et al. 1999, Guainazzi & Antonelli 1999).

Table 4.13: Calculated values of τ. Note that the given error is a formal uncertainty. A more realistic value can be estimated from the scatter in Figure 4.15 to ~0.5.

ν	A10	A11	A12	A13	A14	A15
5 GHz	$3.22 \pm 0.29^{\mathrm{a}}$	-	-	-	-	-
8.4 GHz	0.52 ± 0.16	$2.97 \pm 0.20^{\mathrm{a}}$	-	-	-	-
22 GHz	0.00 ± 0.04	2.49 ± 0.18	2.59 ± 0.18	$3.61 \pm 0.26^{\mathrm{a}}$	-	-
43 GHz	0.29 ± 0.02	3.00 ± 0.06	2.25 ± 0.06	2.17 ± 0.08	1.90 ± 0.08	$8.15 \pm 0.17^{\mathrm{a}}$

[a] The jet core is likely to show a combination of self- and free-free absorption.

The results from the analysis of the brightness temperature distribution along the eastern jet draw a consistent picture of the situation at the center of NGC 1052. At the inner 3 mas of the eastern jet a free-free absorbing medium dominates the flux density properties. This absorber has a nearly sharp edge since its influence rises rapidly within one milliarcsecond, corresponding to less than 0.1 pc. The components which are visible nearer than 3 mas to the center are observed through this absorber and thus are substantially dimmed relative to their initial brightness. With the information of the absolute contribution of the obscuring torus and the knowledge of its spatial extent it will be possible to derive additional information about its density gradients in the analysis of the core–shift in Section 4.6 .

4.5 Polarimetry

The polarimetric information contained in the measurement of all four Stokes parameters can be used to image the polarized emission of the observed sources. The calibration method described in Section 3.3 makes it necessary to compare the derived electric vector position angles (EVPA) to other measurements in order to make sure that the polarization calibration worked properly. 3C 345, included as a calibrator source in the VLBA observations of NGC 1052, is very well suited for this purpose since a big 'database' exists in the literature from which the EVPA of the core and jet regions in this source can be obtained. Once the EVPA of 3C 345 at a special frequency and epoch is calibrated the corresponding rotation can be applied. The same rotation of the EVPA then has to be applied to the corresponding dataset of NGC 1052 at the same epoch and frequency.

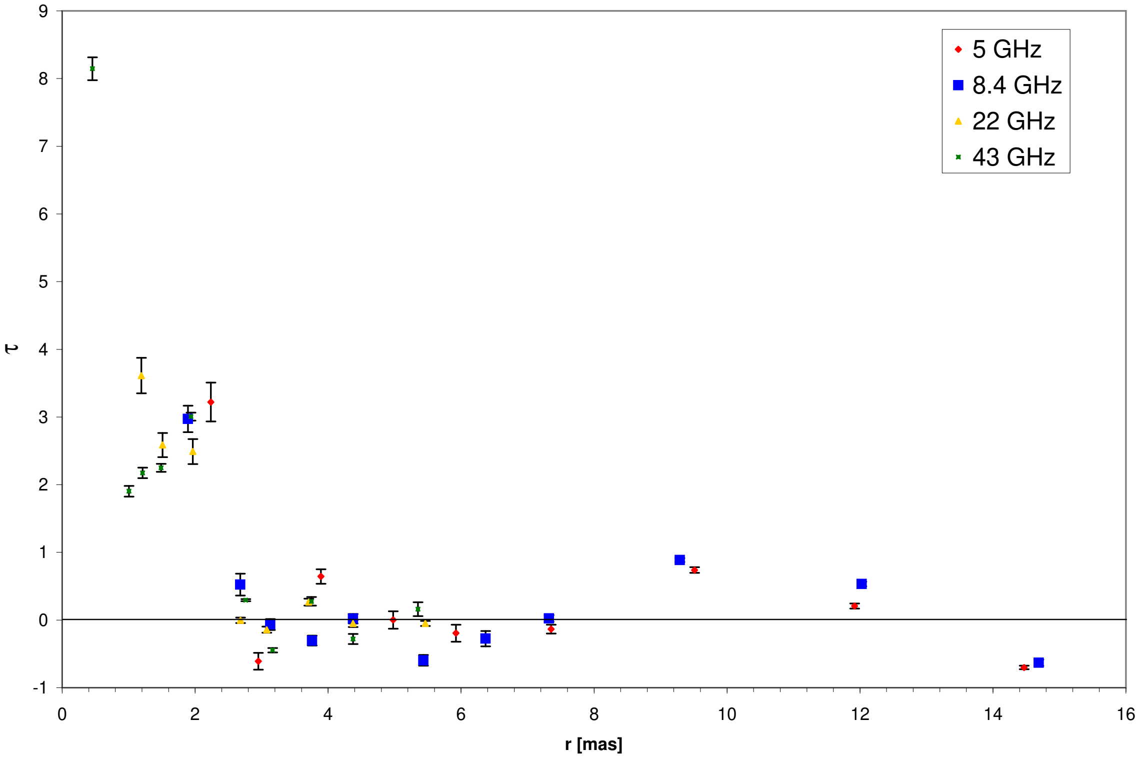

Figure 4.15: Calculated opacities along the eastern jet of NGC 1052.

3C 345 was mapped in DIFMAP using the automatic mapping scripts MUPPET and AUTOMAP developed by Shepherd and Taylor (for the CJ-survey). Special care was taken at 43 GHz where the same 'manual' mapping technique was used as for the target source NGC 1052 (see Section 3.3). The FITS-files were then read into $\mathcal{AIPS}$ and the mapping of the Q, U and V Stokes parameters was done. In this mapping procedure an antenna table was applied which contained the D-terms of the VLBA at the corresponding frequency, determined from NGC 1052 (Section 3.3). The maps of Q and U were combined using the task COMB. The linearly polarized intensity and the EVPA are presented in Figure 4.16. It should be mentioned that these maps are only a by-product of the target observation of NGC 1052 and are based only on two scans of 5 minutes each at all frequencies. 3C 345 shows a core-jet structure with 3 main components at 43 GHz.

It is known that the EVPA in 3C 345 is highly variable at 5 GHz in the core region but stable at the two extended jet regions starting at ∼3 mas from the core, where the EVPA is roughly parallel to the jet. This is in good agreement with the EVPA in these regions in Figure 4.16. Therefore, no EVPA rotation was necessary from the polarization calibration at this frequency.

At 8.4 GHz the situation is more difficult since no stable region of EVPA is known at this frequency in 3C 345. For the calibration of the EVPA the single dish results from the Michigan database (accessible via the Internet at the URL: `http://www.astro.lsa.umich.edu-/obs/radiotel/umrao.html`) were used. A rotation of the electric vector of -73° was needed. At 22 and 43 GHz the D-term results from the 3C 120 monitoring from Gómez et al. (2000) were used. No correction of the EVPA at 43 GHz had to be applied. At 22 GHz a rotation about -75° was necessary.

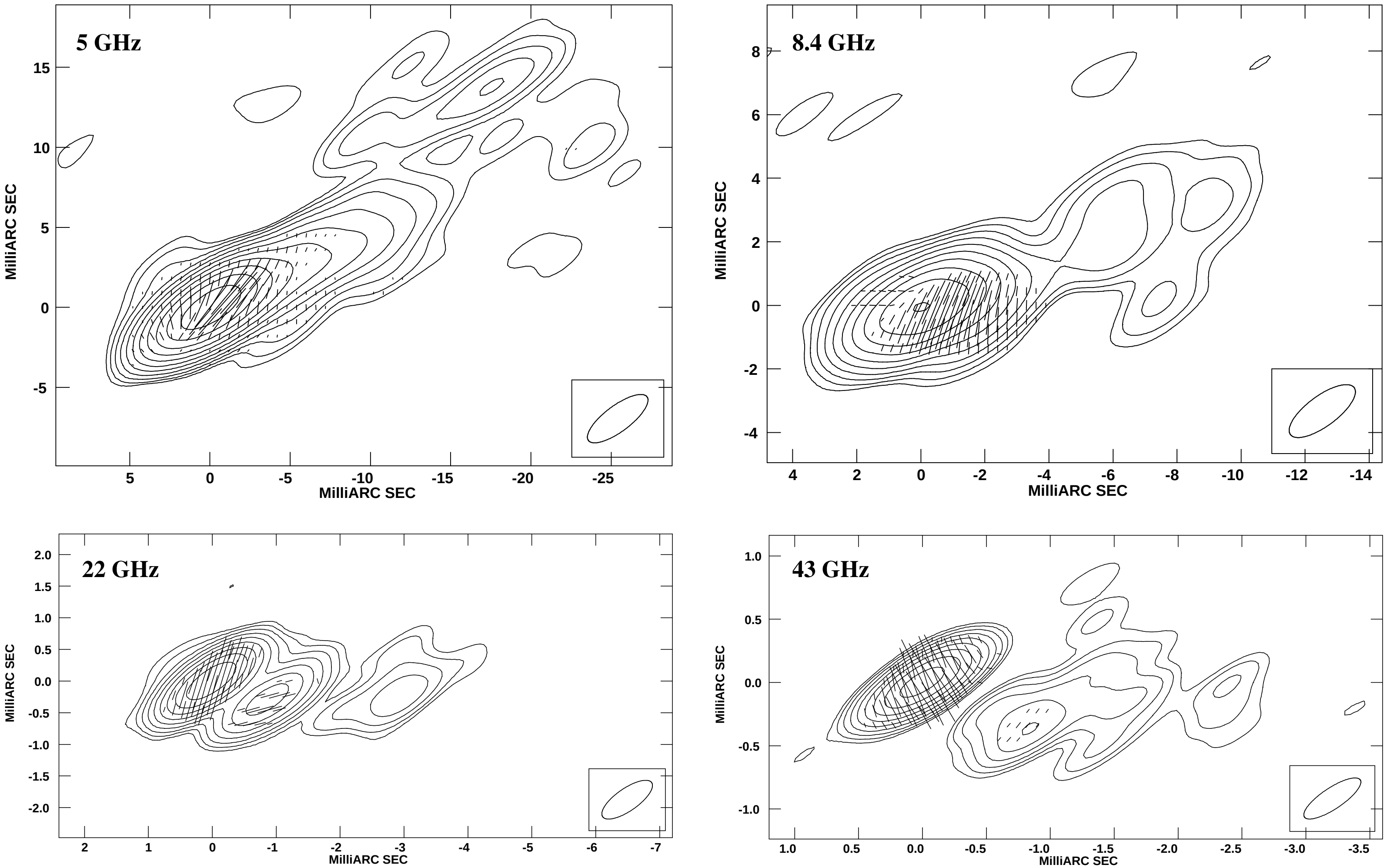

Figure 4.16: Polarized emission images of 3C 345 at 5, 8.4, 22 and 43 GHz. The total intensity is shown in contours. Superimposed, the EVPAs are shown, with a length proportional to the linearly polarized intensity. The contour level intervals are 3, 8, 10 and 8 mJy at 5, 8.4, 22 and 43 GHz, and a length of 1 mas of the EVPA corresponds to 33, 67, 133 and 267 mJy, respectively.

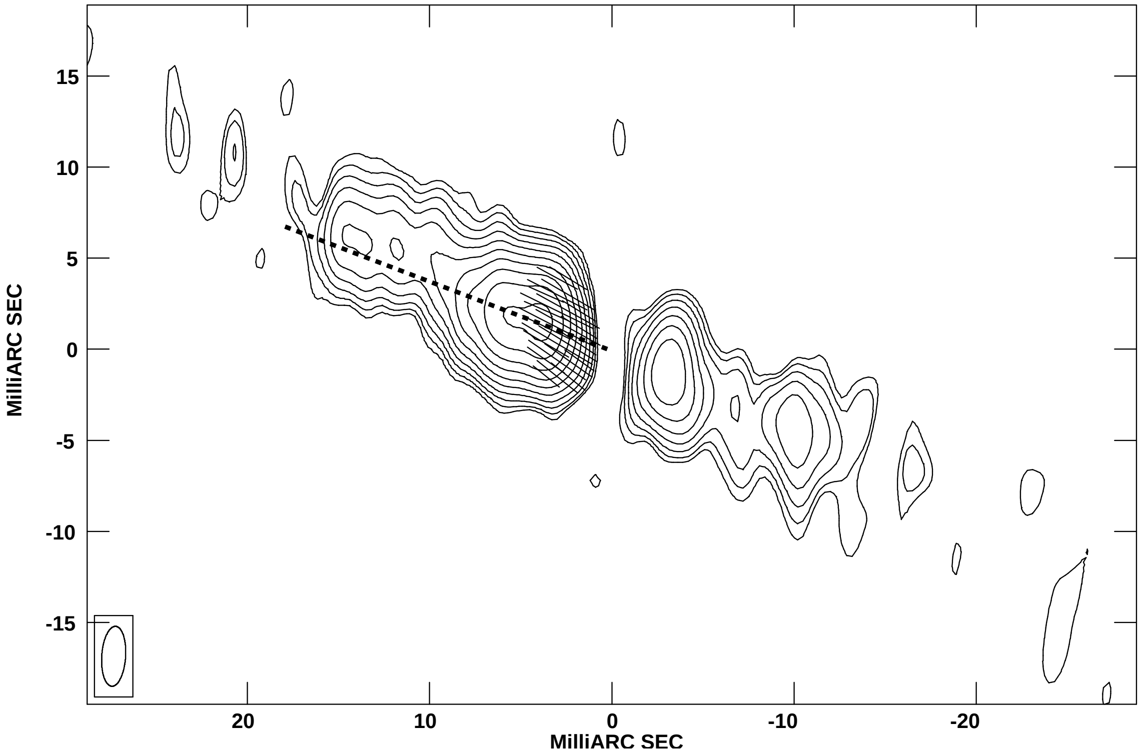

Figure 4.17: The C–band map of the polarized emission in NGC 1052.

The maps in Figure 4.16 are χ-corrected and thus show the true polarimetric structure of 3C 345 at epoch 1998.99.

NGC 1052 was mapped in all four Stokes parameters according to the procedure described in Section 3.3 . Figure 4.17 shows the linearly polarized intensity and its EVPA overlaid on the total intensity at 5 GHz. A region of linearly polarized emission is visible at the base of the eastern jet. The peak is about 3 mJy per beam and the EVPA is about 70°, roughly parallel to the jet. This indicates an ordered magnetic field perpendicular to the jet axis, if no Faraday rotation is assumed. To decide whether the region of linearly polarized emission is resolved or unresolved, a slice through jet axis of both the total intensity map and the polarization map was produced, using the task SLICE in $\mathcal{AIPS}$ (Figure 4.18). In this plot the polarized emission peaks about 1 mas offset from the total intensity maximum. A comparison to Figure 4.3 ascribes this part of the jet to component A10, which is optically thick at 5 GHz. A weak asymmetry of the polarized emission slice suggests a contribution of at least two components. The polarized emission is thus slightly resolved and originates in the optically thick part of the eastern jet at 5 GHz.

No linearly polarized emission from NGC 1052 could be detected at the other three frequencies. Usually the degree of polarization rises with frequency[8] and thus it would be expected that the eastern jet should exhibit polarized emission from the region around component A10 and A11 also at 8.4 GHz. Having the polarization the same (flat) spectrum

[8]Beam depolarization should lower the degree of polarization at the lower frequency much stronger than at the higher frequency, due to the different beam sizes.

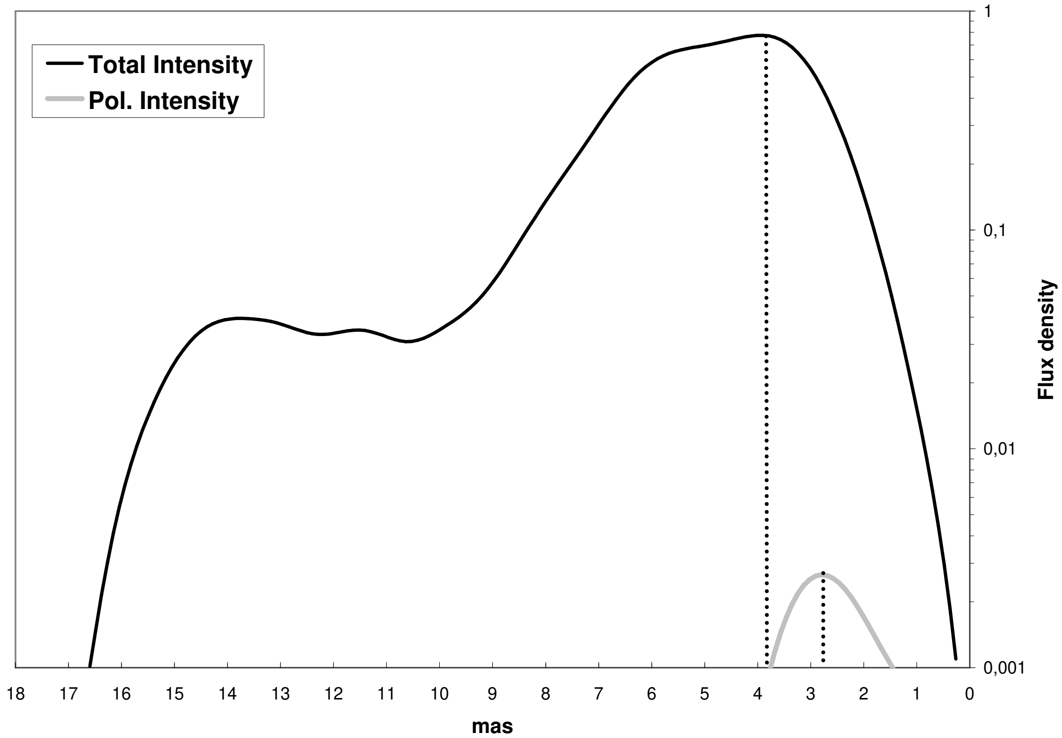

Figure 4.18: Slice through the total intensity and polarized emission along the eastern jet of NGC 1052 at 5 GHz.

as the total intensity in this regime, it should reach a value of about 3 mJy per beam at 8.4 GHz (comparable to the polarized flux at 5 GHz). At higher frequencies these components become optically thin and thus fall in total intensity. If their emission is polarized to the same degree than at 5 GHz this would correspond to less than 1 mJy and thus below the detection threshold.

The simplest explanation for this behavior of the linearly polarized emission from this jet-region is, that the different layers of the jet have a different degree of polarization. Since the region around component A10 is optically thick at 5 GHz, the detected emission originates in an outer layer of the jet. If this outer layer is polarized to a higher degree than the inner layers of the jet, one indeed expects no polarized emission at 8.4 GHz, where the region around A10 is optically thin and we are observing a much deeper region of the jet. However, this raises the question, why the region around A11 appears to be unpolarized, which is still optically thick at 8.4 GHz. In principle the higher column density at this more central region could cause higher Faraday depolarization than it does at the region around A10. This idea is supported by the fact that A10 is the first component which seems to be affected by strong free-free absorption (see Section 4.4). In this scenario the radiation from the outer jet layers is intrinsically linearly polarized. Inside a radius of 3 mas however, Faraday depolarization inside a central torus makes the radiation appear unpolarized. This scenario needs to be tested with observations at longer wavelengths and especially around 5 GHz, where the depolarization is expected to start dominating.

4.6 Core shift analysis

The symmetry between the jet and the counterjet constrains the position of the central engine in NGC 1052. The core of both jets (compare Section 2.2.3 for a definition of the term "core") are located at the distances to the central engine r_c, where the optical depth τ has fallen to be ~ 1. This distance is given by: $r_c \sim \nu^{-\frac{1}{k_r}}$, where $k_r = ((3 - 2\alpha)m + 2n - 2)/(5 - 2\alpha)$, with m and n the power indices of the magnetic field and the particle density: $B \sim r^{-m}$, $N \sim r^{-n}$ (Lobanov 1998). Taking logarithms leads to:

$$\log(r_c) = \text{const.} - \frac{1}{k_r} \cdot \log(\nu).$$

Measuring r_c at two frequencies allows one to determine k_r in the corresponding region of the jet. For a freely expanding jet in equipartition Blandford & Königl (1979), k_r=1. The value of k_r is larger in regions with steep pressure gradients and may reach 2.5, for reasonable values of m, n ($\leq$4, see Lobanov 1998). If external absorption determines the apparent core position, comparable density gradients of the external medium can alter k_r to values above 2.5 (see Section 2.2.3 for details).

The values of k_r deduced depend crucially on the absolute values of r_c on the two sides and therefore on the assumed position of the central engine. Four scenarios have been tested with different reference points (see Figure 4.19). Table 4.14 gives the derived values of k_r for each scenario.

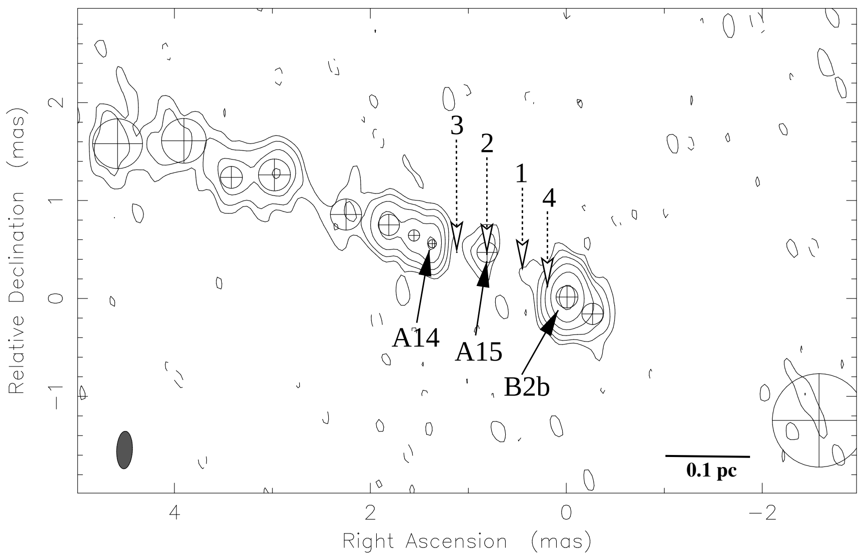

Figure 4.19: Image with the model fitting results of the 43 GHz data. The circles represent the Gaussian components. The innermost jet components are labeled as A14, A15 and B2b. The putative locations of the central engine are indicated (dashed arrows) for 4 different scenarios (see discussion in the text).

The area between the model components A15 and B2b is the most likely location of the central engine and the center between both components is a natural choice for its exact position (scenario 1). Shifting the reference point eastwards (scenarios 2 and 3) alters the values of k_r into unphysically large regimes (requiring density gradients $\propto r^{-10}$ and higher). Assuming the true center of activity to be located more westwards (closer to B 2b, scenario 4), the values of k_r derived are still acceptable.

Table 4.14: k_r values for the four different putative centers of activity.

ν [GHz]	—Scenario 1— $k_{r,\text{east}}$	$k_{r,\text{west}}$	—Scenario 2— $k_{r,\text{east}}$	$k_{r,\text{west}}$	—Scenario 3— $k_{r,\text{east}}$	$k_{r,\text{west}}$	—Scenario 4— $k_{r,\text{east}}$	$k_{r,\text{west}}$
5–8.4	3.1±2.6	–	2.5±2.2	–	3.0±3.6	–	3.4±2.8	–
8.4–22	2.1±0.5	6.6±2.8	1.5±0.3	11.9±5.1	1.0±0.2	14.8±6.2	2.4±0.6	3.8±1.6
22–43	3.9±0.8	6.8±2.7	2.4±0.5	13.0±5.2	1.3±0.2	17.1±7.1	4.8±1.0	3.6±1.3

The core positions of both jets at the different frequencies for the first case (scenario 1) are shown in Figure 4.20. The eastern jet has rather high values of k_r below 22 GHz, although still in agreement with steep pressure gradients in the jet environment. Above 22 GHz k_r is 3.9±0.8, which is a good indicator for free-free absorption affecting the jet opacity. The western jet has values of k_r as high as 6.8±2.7 between 22 and 43 GHz, suggesting a large contribution from free–free absorption.

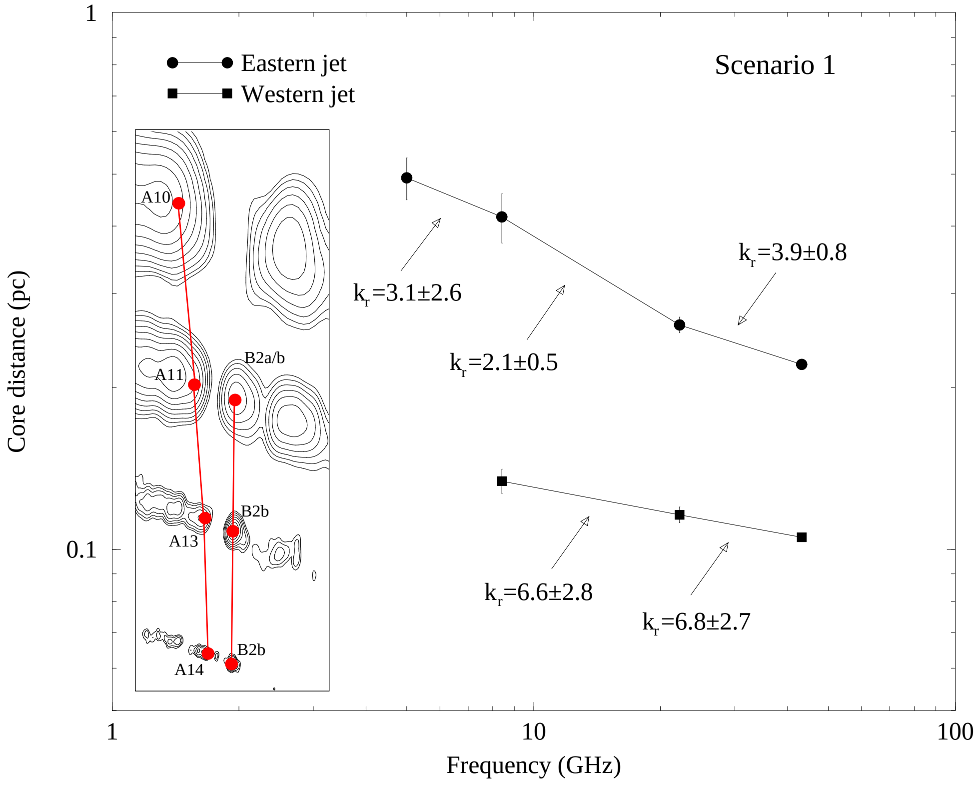

Figure 4.20: Core positions in the two jets at the different frequencies for scenario 1 (see Figure 4.19). The corresponding values of k_r for the core–shift between adjacent frequencies are labeled. Smaller core–shifts correspond to higher values of k_r. Table 4.14 provides the values of k_r for the other three scenarios. The inlaid panel shows the core-locations in the source at the four frequencies (from top to bottom at 5, 8.4, 22 and 43 GHz).

The results from the core–shift analysis support the picture of a free–free absorbing torus covering mainly the inner part of the western jet and also a smaller fraction of the eastern jet. The extend of this torus along the eastern jet is consistent with the results derived from the analysis of brightness temperature distribution (Section 4.4). The true center of activity in NGC 1052 can be determined to lie between the model components A 15 and B 2b, with an uncertainty of only ~ 0.03 pc.

Chapter 5

The big picture

In Chapter 4 and in Appendix A, C and D various approaches have been made to the understanding of the physical situation at the very center of the elliptical galaxy NGC 1052. This chapter summarizes the distinct results derived and puts them together into a consistent model of the pc–scale structure of the source. The model is kept as simple as possible in order to describe the observations on the one hand and not to introduce unnecessary and complicating components. It is based on the standard model for AGN (see Section 1.2.2 and 1.2.3), considering only the components accessible by radio interferometry (e.g., the BLR and NLR can be observed in optical astronomy but are not obviously needed from VLBI observations). It is assumed that the twin jet originates at the center of NGC 1052 in the vicinity of a supermassive black hole, which is surrounded by an accretion disk. The dimensions of the accretion disk are assumed to be negligible, compared to the resolved scales, i.e. its diameter is $\ll 1$ pc.

The main result of this thesis is the fact that another component, a central absorber, is unavoidably needed for a correct model of the source. The dominance of this absorber is spatially bounded to the central parsec around the black hole and corresponds to the obscuring torus in the standard model (the geometrical, toroidal structure is not *a–priori* given; however, the term "obscuring torus" is used synonymously for "geometrically thick absorber", since it has become fairly common in usual terminology). Evidence for the presence of an obscuring torus surrounding the pc–scale twin jet of NGC 1052 comes from the following approaches:

- **Spectral index mapping:** Between 5 and 43 GHz the spectral index α diverges at both jet-cores. At high frequencies values of 2.5, the theoretical maximal spectral index in the case of synchrotron self-absorption, are approached but not exceeded. Between 5 and 8.4 GHz however, α reaches values larger than 4 on both sides of the emission gap. Although it is in principle possible to lower the values of α on the eastern side by choosing a different alignment, the effect of free-free absorption on the western side is indisputable.

- **Component spectra:** The model-fitting of the source with circular Gaussian components yielded component spectra with spectral indices larger than 4. The absorbed model components are the innermost ones of the 8.4 GHz model, representing the jet-cores of the eastern and the western jet respectively. Only a very conservative estimate of the (undetected) component flux density at 5 GHz can explain the spectrum of the core on the eastern side without the contribution of free-free absorption. On the western side this effect is again indisputable.

- **The brightness temperature distribution:** Along the eastern jet the distribution of brightness temperatures for the model-fit components can be explained well with an external absorber model. A cutoff in the distribution of T_b appears frequency-independent in all four models at a distance of about 3 mas east of the core. Inside this radius (corresponding to about 0.3 pc) the brightness temperatures of all model components fall substantially below the extrapolation from the outer part of the jet. They appear to be seen through a layer of free-free absorbing material with a column density of $\sim 6 \cdot 10^{22}\,\mathrm{cm}^{-2}$.

- **The absence of polarization above 5 GHz:** Although the total intensity from the core of the eastern jet is comparably strong at 5 and 8.4 GHz, the linear polarized emission detected at 5 GHz from this region has no counterpart at 8.4 GHz. One possible explanation for this behavior is that strong Faraday depolarization makes the intrinsically present linear polarization at 8.4 GHz from this (more central) jet-region undetectable.

- **The core shift analysis:** NGC 1052 is one of only a small number of extragalactic radio jets in which absolute core shifts with frequency can be measured. This is due to the symmetry of the twin jet, which constrains the absolute position of the central engine. Within the uncertainties of the latter, various scenarios agree on the necessity of free-free absorption to explain the measured core shifts. In the most plausible case the core shifts in both jets are caused by free-free absorption, with the western side being much stronger affected.

- **The X-ray spectrum of the nucleus:** The spectrum of the compact, nuclear X-ray emission implies an absorbing column density comparable to the values suggested by the brightness temperature analysis (see Appendix D). Attempts to avoid the absorbed component in the modeling of the measured spectrum do not lead to satisfactory results.

All of these various aspects of data analysis from observations of NGC 1052 are consistent with a model of a very dense absorber surrounding the central engine. This absorber seems to have a rather sharp edge since it starts to dominate the radiation from the eastern pc–scale jet within a few tens of milliarcseconds. It covers the inner 0.3 pc of the eastern jet and at least the same scale on the western side. A more detailed modeling of the absorber is difficult but might be possible with additional data from future observations. The combination of simultaneously performed multi-frequency VLBI and X-ray observations is capable of yielding estimates for the absolute density and the density gradients of the absorber. For the latter, the absolute position of the central engine needs to be determined more precisely from multi-epoch VLBI observations at the highest frequencies.

A sketch of this model is shown in Figure 5.1. The geometry of the absorber cannot be determined finally from the present data, but is not in contradiction to the standard model, which assumes a toroidal structure. Since the two jets seem to be oriented fairly close to the plane of the sky, it is difficult to distinguish a torus from a radially symmetric absorber. The most universally valid geometrical structure in concordance with the observational data presented in this thesis is an ellipsoid with a short axis of ~0.3 pc. The edge of

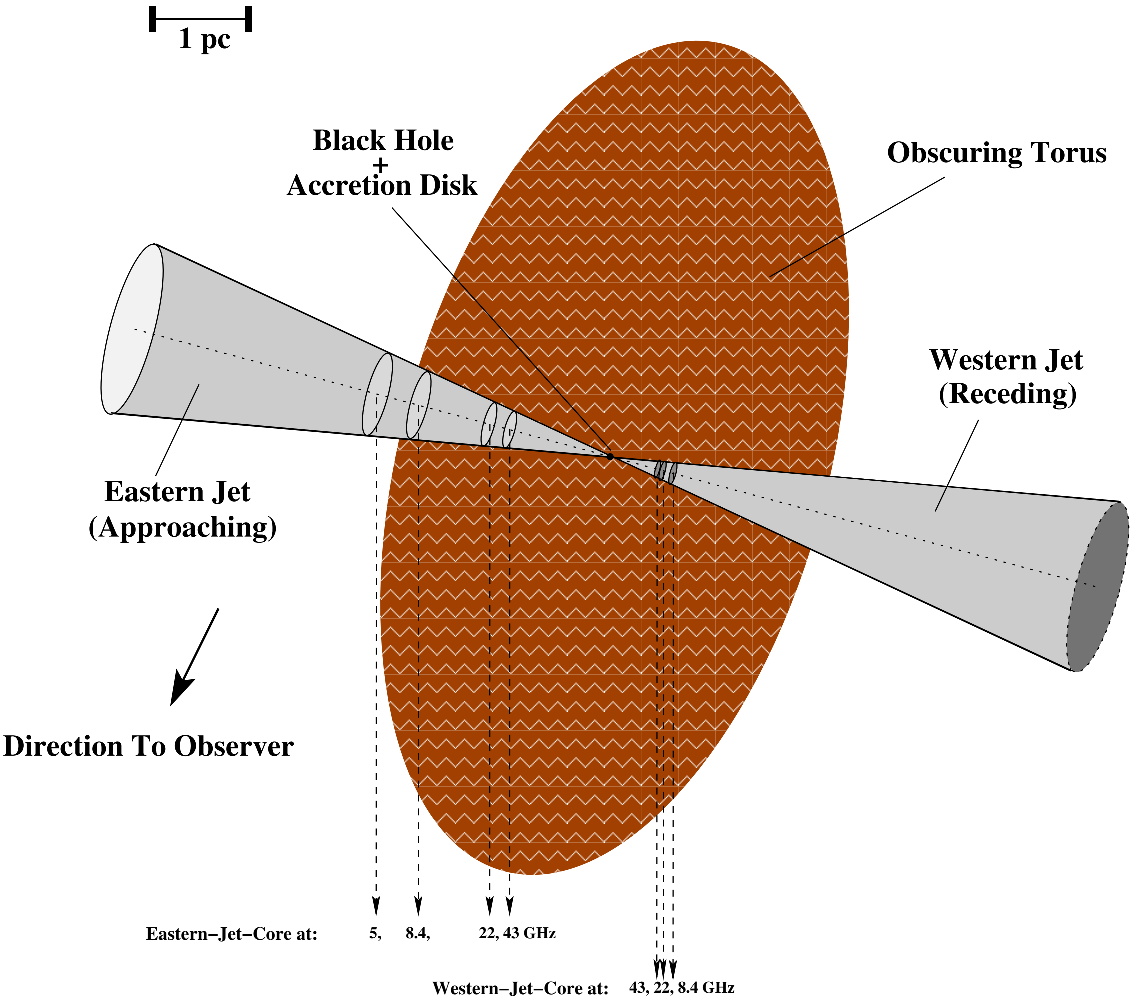

Figure 5.1: Model of the central parsecs in NGC 1052

the absorber may represent the surface of ionization from a central source, for example the accretion disk. Therefore, temperatures larger than 10^4 K are expected within the absorber, ensuring the presence of ionized, free-free absorbing material.

Appendix A

The single dish spectrum of NGC 1052

NGC 1052 is variable at all frequencies observations have been carried out at so far. Variations occur on timescales of months with a tendency of shorter timescales at higher frequencies. For this, it is difficult to obtain a complete source spectrum, since the observations have to be done quasi-simultaneously.

Between August 2001 and March 2002 several flux density measurements of NGC 1052 have been carried out within the scope of this thesis. 9 data points have been obtained with the Effelsberg 100 m telescope between 1.4 and 30 GHz. At 100 and 230 GHz (3 and 1.3 mm) the source flux density has been determined with the Pico Veleta 30 m telescope. Table A.1 lists the available measurements and the obtained spectrum is plotted in Figure A.1.

Table A.1: Flux density measurements of NGC 1052

Frequency	Wavelength	Date	Flux density	Telescope
1.4 GHz	21 cm	18.3.2002	1.40± 0.01 Jy	Effelsberg[a]
1.66 GHz	18 cm	29.8.2001	1.474± 0.020 Jy	Effelsberg[a]
4.85 GHz	6 cm	4.9.2001	1.471± 0.009 Jy	Effelsberg[a]
4.85 GHz	6 cm	10.12.2001	1.463± 0.010 Jy	Effelsberg[a]
8.55 GHz	3.5 cm	8.1.2002	1.40± 0.01 Jy	Effelsberg[a]
10.45 GHz	2.8 cm	10.12.2001	1.378± 0.010 Jy	Effelsberg[a]
22 GHz	1.3 cm	8.1.2002	940± 20 mJy	Effelsberg[a]
22 GHz	1.3 cm	1.2.2002	815.5± 61.7 mJy	Effelsberg[a]
30 GHz	1 cm	26.3.2002	790± 40 mJy	Effelsberg[a]
100 GHz	3 mm	18.9.2001	600±30 mJy	Pico Veleta[b]
230 GHz	1.3 mm	9.12.2001	200±40 mJy	Pico Veleta[c]

[a] performance of the measurements by Dr. A. Kraus; [b] performance of the observation by Dr. H. Ungerechts; [c] performance of the observation by J. Kaufmann

Although it has to be kept in mind that these single dish measurements have been done in winter 2001/2002, about 3 years after the VLBA observations in December 1998, the obtained single dish spectrum can give valuable additional information for the correct interpretation of the VLBI data.

The spectrum appears nearly flat up to $\sim$10 GHz. Between 10 and 22 GHz it turns over and becomes steep. Since no data are available between these frequencies, the exact turnover frequency cannot be located more precisely. Between 10 and 22 GHz the spectral index is -0.6, the spectrum becoming flatter between 22 and 100 GHz ($\alpha_{22-100} \sim -0.25$).

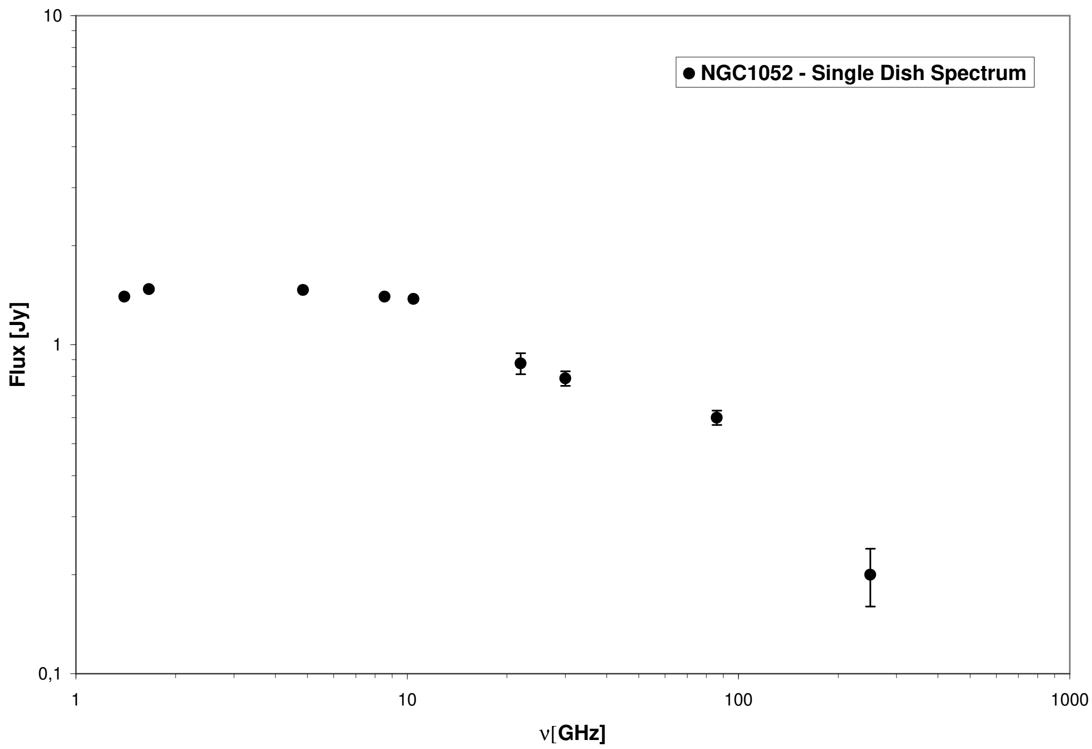

Figure A.1: Single dish spectrum of NGC 1052, measured between August 2001 and March 2002.

It is interesting to note that the VLBI spectrum (from December 1998) turns over in the same regime between 8.4 and 22 GHz and that this could be attributed mainly to the strong decrease of the flux density from the eastern jet compare Figure 4.8. The brightness temperature distribution (Section 4.4) revealed that free-free absorption starts inwards of 3 mas from the central engine, a region of the jet with local turnover frequencies above 8.4 GHz. The sharp cutoff of the single dish spectrum above 10 GHz thus can be interpreted as free-free absorption of the inner jet-regions of the bright, approaching eastern jet, by a stationary obscuring torus. In this picture, the counterjet contributes only an negligible fraction to the registered flux density below 10 GHz, since it is much stronger affected by the obscuration. This explains the flatness of the single-dish spectrum below 10 GHz, which is typical for a one–sided pc–scale jet. Above 10 GHz the inner part of the eastern jet should maintain the flat spectrum, but the edge of the absorber cuts off the spectrum at this point. This interpretation can be tested in a long-term monitoring of the spectrum of NGC 1052. Even if the overall shape of the spectrum varies with time, the cutoff between 10 and 22 GHz should remain a stationary feature of the source-spectrum.

At even higher frequencies (>100 GHz) the spectrum becomes very steep ($\alpha_{100-230} \sim -1.3$). This can be understood in terms of a lack of high energy (synchrotron producing) electrons. If a magnetic field of 60 mG is assumed, a cutoff in the electron energy distribution above $\gamma =\sim 1300$ can be estimated from Equation (2.6). This high value is indeed needed, if the strong and compact X-ray emission from the core of NGC 1052 shall be interpreted in terms of the SSC model (compare Equation 2.12).

Appendix B

MERLIN and CHANDRA observations and data reduction

In this section the radio interferometer MERLIN and the X-ray satellite CHANDRA will be introduced. Both facilities have been used to study the structure of NGC 1052 on kpc–scales in order to visualize more completely the source as a whole than offered by VLBI studies of the radio core alone. Especially spectroscopy of the compact X-ray core in connection with high resolution VLBI imaging is capable of giving a much deeper insight into the physical processes at work in the very vicinity of the central engine. Since VLBI is not sensitive to the emission from the jets on kpc–scales, radio interferometric observations with smaller baselines (as offered by MERLIN) are needed to connect the extended X-ray emission detected by CHANDRA to the radio regime. The data from both facilities have been obtained from public archives and the observations and the data reduction are presented in this chapter The results are presented and discussed in Appendix C and D.

MERLIN data: MERLIN stands for **M**ulti-**E**lement **R**adio-**L**inked **I**nterferometer **N**etwork, a telescope array consisting of 8 individual antennas connected by microwave links and thus forming an aperture synthesis radio telescope with a biggest baseline of about 217 km. MERLIN is capable of observing in full polarimetric mode and its resolution (40 mas at 6 cm wavelength) lies in the middle between the resolutions obtained with VLBI and connected arrays as the VLA. Observations can be done between 151 MHz and 22 GHz with corresponding angular resolutions between 1.4 arcsec and 8 mas. The array consists of the 76 m Lovell telescope and the 37×25 m Mk2 telescope at Jodrell Bank, three 25 m dishes, of the same design as the VLA antennas, located at Tabley and Darnhall in Cheshire and Knockin in Shropshire, another 25 m antenna at Defford in Worcestershire, a second elliptical 37×25 m dish at Wardle (Mk3 telescope) and the 32 m telescope in Cambridge. The location of the MERLIN antennas is shown in Figure B.1.

Data, older than one year, can be obtained from a public archive, provided by the university of Manchester, the operator of MERLIN. On the MERLIN website[1] a complete catalog of MERLIN observations since 1991 can be searched and the *a–priori* calibrated data, processed in a uniform manner by the MERLIN archivist, can be obtained.

MERLIN observed NGC 1052 on November 22nd 1995 with all 8 antennas of the array at 1.4 GHz. The observation was planned and scheduled by Dr. A. Pedlar. The data, ob-

[1] `http://www.merlin.ac.uk`

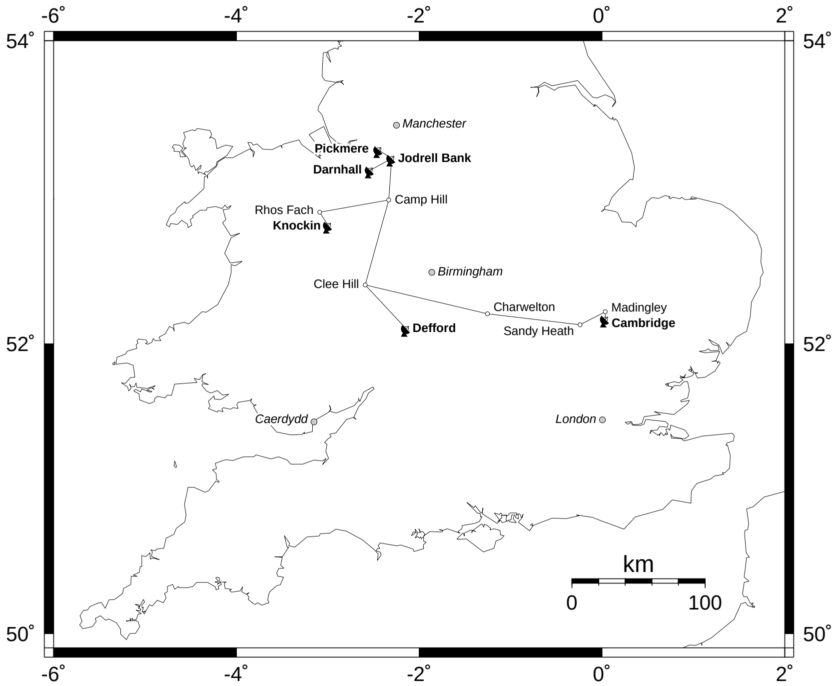

Figure B.1: The antennas of MERLIN

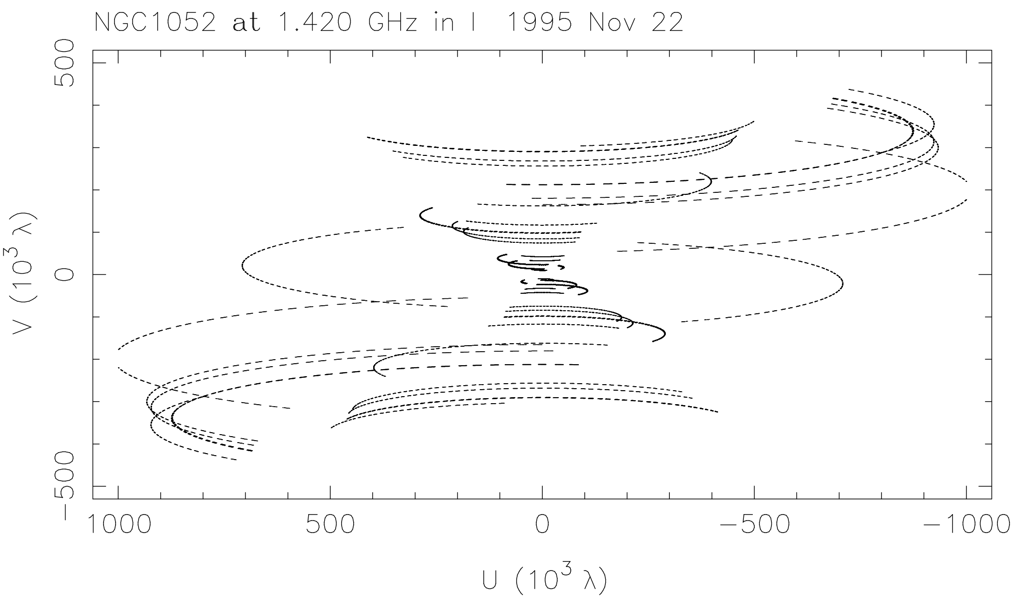

Figure B.2: The (u, v) coverage of the MERLIN observation of NGC 1052.

tained during this experiment, were retrieved from the MERLIN archive with the consent of the principle investigator.

The post-processing of these data was done in DIFMAP. Basically the same strategy as for the mapping and self calibration of the VLBI data, described in Section 3.3, was used with special care on the weighting of the data. Figure B.2 shows the (u, v)-coverage during the observation.

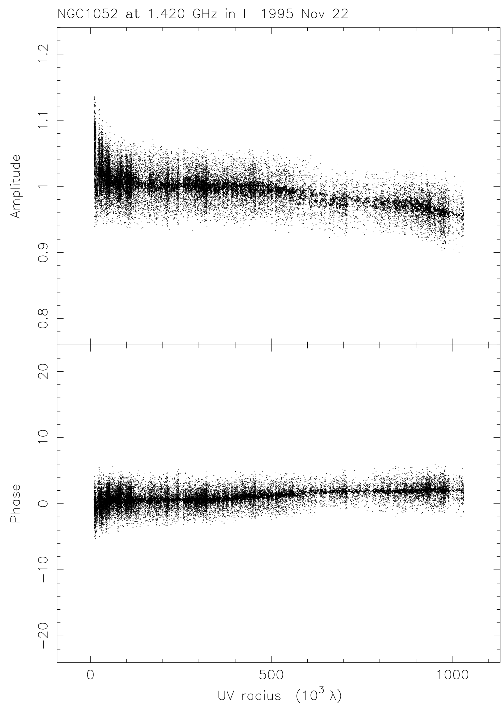

Figure B.3: The visibilities as a function of (u, v) distance and the best model visibilities for the MERLIN observation of NGC 1052.

After a little editing of the data, using the editing option of the commands RADPLOT and VPLOT and the choice of an appropriate map– and cell-size, the mapping was started with natural weighting. After cleaning the central structures, a moderate tapering of the longer baselines revealed more extended emission regions. A strong (u, v)–taper was needed to map the extended lobes of the source, since the synthesized beam of MERLIN at 1.4 GHz is much smaller than these and much of the flux associated with these extended structures would have been resolved out without tapering. After obtaining a good model the data were amplitude self–calibrated, using the command GSCALE, by applying time-independent antenna based correction factors. These factors were 1 without any exception, suggesting a very high quality of the pre-calibrated data. Seven further cycles of cleaning and amplitude calibration were done, each with pure natural weighting for the most compact regions, successively stronger tapering for the more extended regions and decreasing time scales for amplitude self calibration[2]. A final map was produced from the best calibrated data set in two versions, one with the strongest taper applied that had been used during the mapping to show the extended structures of the source, and one with pure natural weighting, showing only the core region of NGC 1052. Figure B.3 shows the visibilities as a function of (u, v)–distance together with the best model, produced with the command RADPLOT. The flatness of the visibility distribution across the (u, v) plane indicates the strong dominance of the central, unresolved core component.

An impression of the quality of the derived model can be obtained by looking at Figure B.4, in which the visibilities on a short (Wardle – Lovell) and a long (Cambridge – Lovell)

[2] A map, produced with uniform weighting for the most compact regions, did not resolve any of the compact features in the natural-weighting-map, but had a higher noise level.

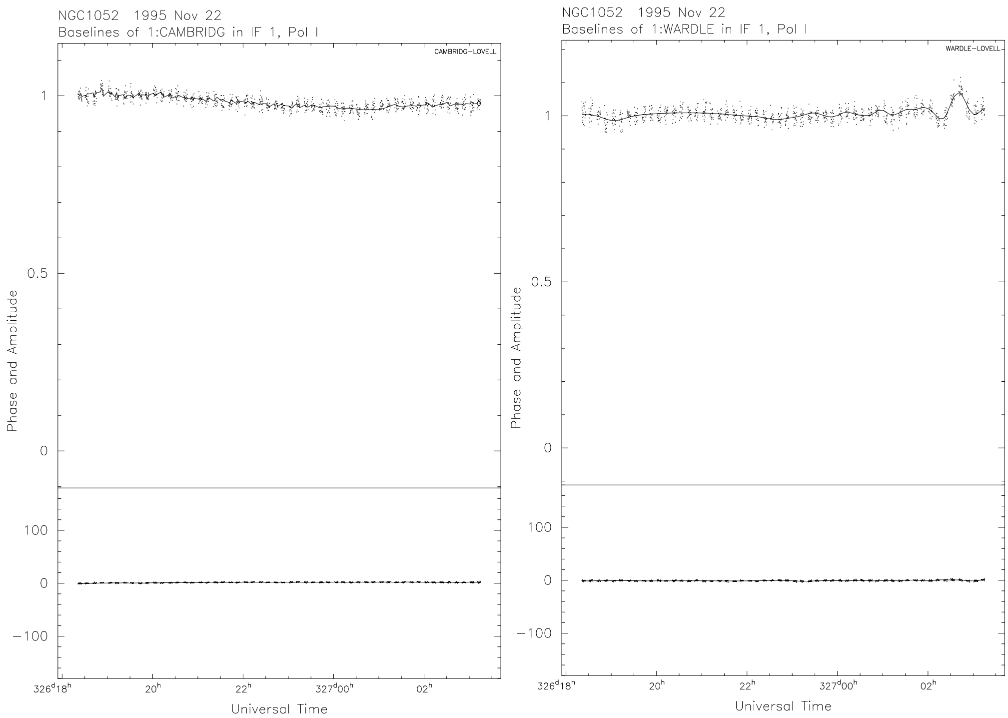

Figure B.4: The visibilities as a function of time for a short (Wardle – Lovell; left panel) and a long (Cambridge – Lovell; right panel) baseline.

baseline as a function of time are shown. The model visibility is seen to lie completely within the scatter of the measured visibilities. The sharp kinks in the model indicate a slight "over modeling" of the data, since a flat curve would probably fit the data nearly as well as the statistically best fit model. However, the deviations are very small and should not affect the final map to a higher degree than introducing spurious features of the same order as the noise level. In Appendix C the final maps are presented and discussed.

CHANDRA data: CHANDRA is one of the most important and efficient X-ray missions of the last and present decade. It has the highest available angular resolution in the X-ray band ($0.5''$), providing the possibility of comparing source structures in the radio (VLA, MERLIN), optical (e.g., the Hubble Space Telescope) and X-ray regime on the same scales. The satellite (Figure B.5) was launched on July 23rd, 1999 and carries a telescope system, consisting of four pairs of mirrors of the Wolter type, which are barrel-shaped and nested (see Figure B.6), focusing incoming X-rays onto a focal plane about 10 m away.

In the focal plane one of two available detectors can be chosen, the **H**igh **R**esolution **C**amera (HRC) and the **A**dvanced **C**CD **I**maging **S**pectrometer (ACIS). Two grating arrays, the low energy transmission grating (LETG) and the high energy transmission grating (HETG) can be flipped into the path of X-rays behind the mirrors for spectroscopy. The CHANDRA data used in this thesis comes from the ACIS detector with no usage of a grating system. For this reason, only the ACIS detector shall be briefly described here.

The ACIS CCD chip array consists of 10 CCD chips divided into two sub-arrays. Four chips make up the ACIS-I array, used for wide-field imaging. It allows a maximal field of view of $16'.9 \times 16'.9$ for each chip with a resolution of $0''.5$, corresponding to a pixel size of $24\,\mu$m. Since the size of the point spread function in the focal plane is of the same order,

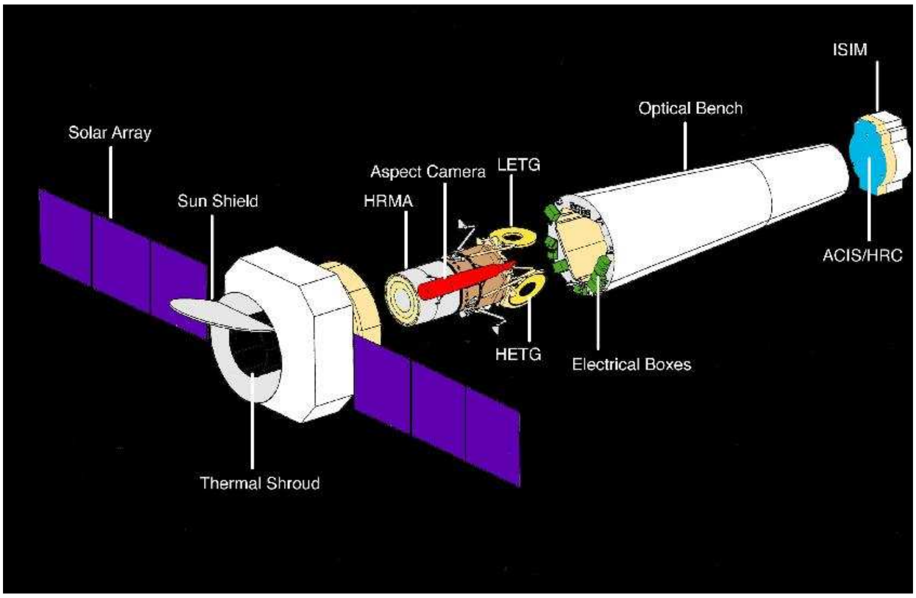

Figure B.5: Components of the CHANDRA satellite. Credits: NASA/CXO/SAO

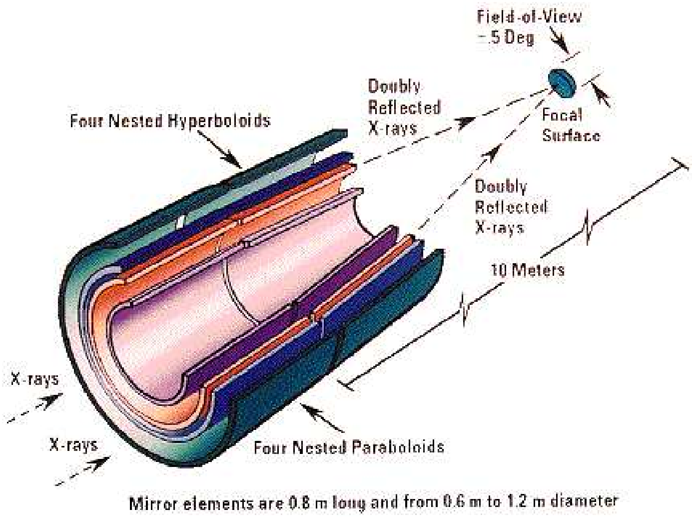

Figure B.6: Illustration of the barrel-shaped mirrors of CHANDRA. Credits: NASA/CXO/SAO

the image from a point-like source is spread over only four pixels. The other six CCD chips make up the ACIS-S array and provide a smaller maximal field of view of $6 \times (8'.3 \times 8'.3)$ for each chip and provide the same resolution as the ACIS-I chips do. Two of the six ACIS-S chips are illuminated from the back side, providing the best possible sensitivity for soft X-rays. Both arrays are capable of measuring the energy of the incoming X-rays. It is thus possible to retrieve both an image of the source and a spectrum within one observation.

The measured spectra are affected by several instrumental effects that have to be removed in order to retrieve the intrinsic source spectrum. One effect is that the angle for total reflection depends on the energy of the incoming photon ($\Theta_c \propto E^{-1}$). Since the focusing angle spans only a small range for a single mirror, this means that photons with the "wrong" energy are not as efficiently focused as photons with the "right" energy are.

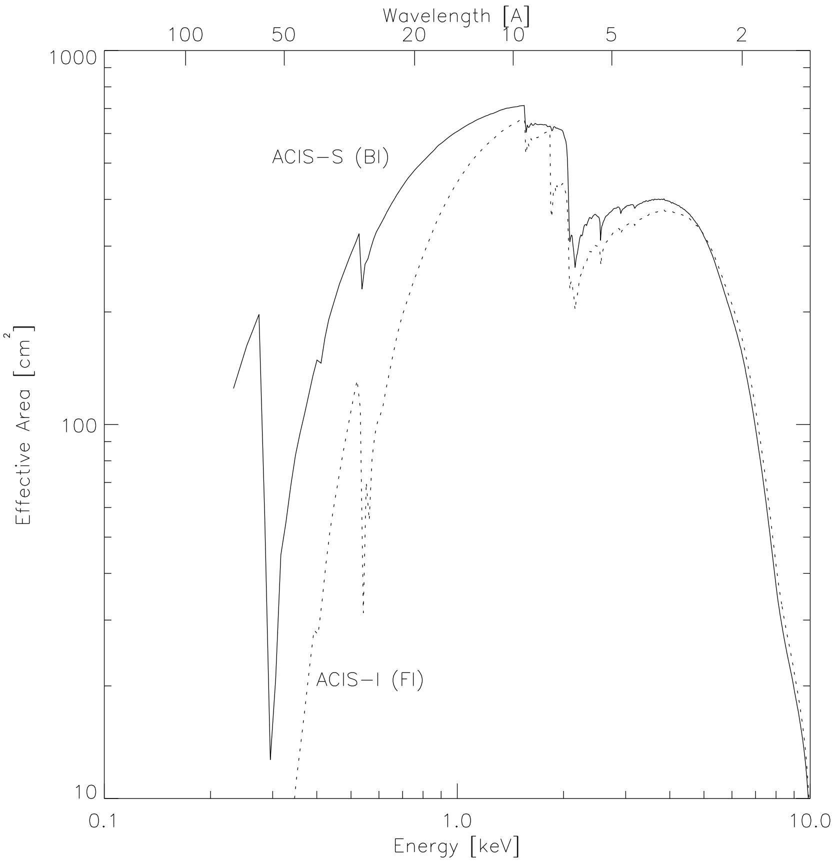

Figure B.7: The predicted effective area for the ACIS-S array versus energy. The dashed line is for the front-illuminated chips, the solid line for the back-illuminated ones (Taken from the CHANDRA Proposers' Observatory Guide at the URL: `http://cxc.harvard.edu/udocs/docs/docs.html`.)

This leads to a variable effective mirror area with respect to the photon energy. This effect is also the reason for the different sizes of the four CHANDRA mirrors: The small inner mirrors focus the hard X-rays, whereas the effective area of the outer mirrors is bigger for the soft X-rays. The interaction of the incoming photons with the detector medium is another instrumental effect that determines the measured spectra. Especially the probability of detecting a photon in a CCD chip, the quantum efficiency, depends on the photon energy. In Figure B.7 the predicted effective area of the ACIS-S array is plotted as a function of photon energy. This function represents the spectral response of the detector to a flat (equal number of incoming photons per energy unit) continuum source. A measured spectrum thus will always be the convolution of this response function with the true, intrinsic source spectrum.

CHANDRA observed NGC 1052 on August 28th, 1999 with an exposure time of 2400 s with the ACIS-S detector configuration. The experiment was planned and scheduled by Dr. G. P. Garmire. After the proprietary period of one year the obtained data has been included in the public data archive[3] from which it was downloaded for analysis. The further

[3]Data from the public CHANDRA data archive can be obtained via the graphical, java based user interface ChaSer (available under `http://cxc.harvard.edu/cda/chaser.html`) or directly at the provisional

processing of the data was done by Dr. J. Kerp with the "CHANDRA Interactive Analysis of Observations" program (CIAO)[4]. A color coded image of NGC 1052 was produced, in which the soft (0.1-1 keV), medium (1-2 keV) and hard (2-3 keV) photon detections are represented by red, green and blue pixels. The technique of adaptive smoothing was used, that spreads the area of a presumed source in the image as far as necessary to reach a specified statistically reliability of the detection. A clipping level of 3σ was chosen. In appendix D the resulting image is presented and discussed.

web interface under `http://cxc.harvard.edu/cgi-gen/cda/retrieve5.pl`.

[4]See `http://cxc.harvard.edu/ciao` for a detailed documentation of this software.

Appendix C

The radio jet of NGC 1052 on kpc–scales

The tapered MERLIN image of NGC 1052, obtained from the November 1995 observation, is shown in Figure C.1. The map is qualitatively very similar to the published image of Wrobel (1984). A very dominant compact core of 1 Jy is seen. Two lobes of extended emission extent about 15 arcsec east and west of the core. In both lobes there are regions of enhanced surface brightness (possibly two hot spots) with a P.A. of about 95°.

Figure C.2 shows the source restored with a circular beam of 1.7 arcsec and the VLA map of Wrobel (1984) from December 1980 with the same linear scale and restoring beam. The VLA, which was operated in its A configuration during the 1980 observations, was more sensitive to extended structures, which partially have been resolved out by MERLIN. Although some contribution by such extended structures might have been lost in the

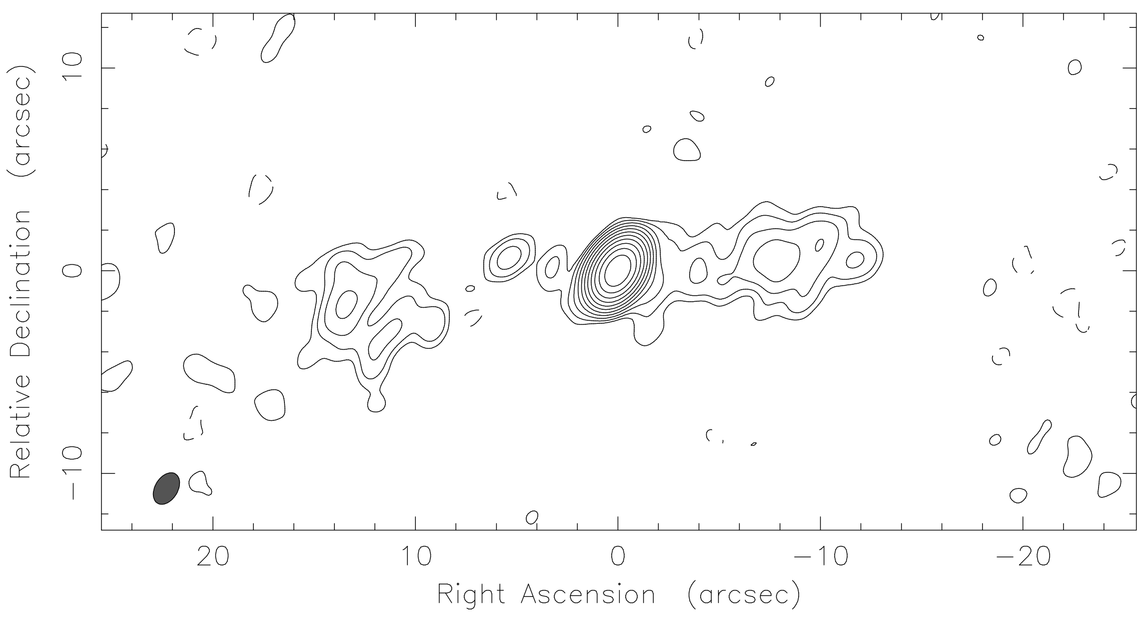

Figure C.1: NGC 1052 on arcseconds scale at 1.4 GHz as imaged by MERLIN. Contours at (−0.5, 0.5, 1, 2, 4, 8, 16, 32, 64, 128, 256, 512) × 1mJy are shown.

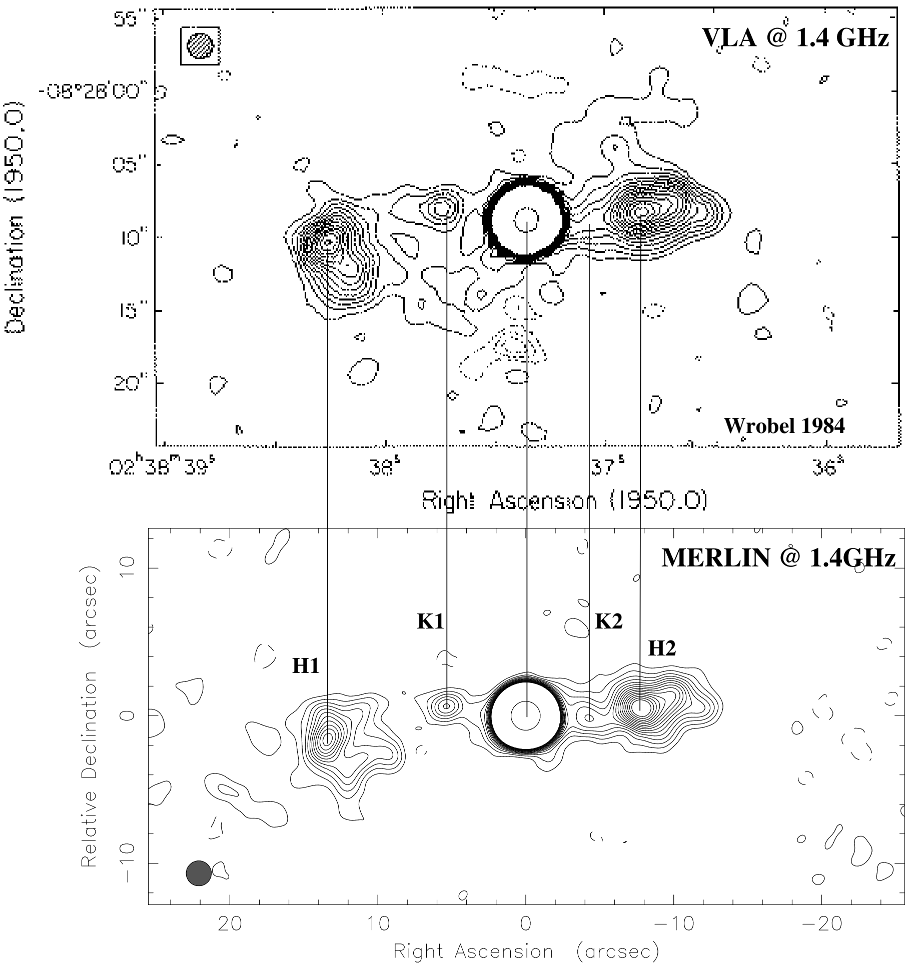

Figure C.2: Comparison between an 1984 VLA image of NGC 1052 (by Wrobel 1984) and the MERLIN image from 1995 at 1.4 GHz. Both maps have been convolved with the same (circular) restoring beam of 1.7 arcsec FWHM. Contours at (-1, 1, 2, 3, 4, 5, 6, 7, 8, 9, 10, 11, 12, 13, 14, 15, 800) × 0.5 mJy are given in both maps (The VLA map shows additionally negative contours at (−4, −3, −2) × 0.5 mJy). The hot spots (labeled as H1 and H2) do not show any motion. Two knots of emission (labeled as K1 and K2) have become significantly brighter (see text). The emission peak of the eastern knot (K1) additionally appears about half an arcsecond closer to the core in the (newer) MERLIN map. The core also brightened from 0.74 Jy to 1.01 Jy.

MERLIN image, it can be stated that the core has varied significantly, with a flux density of 740 mJy in December 1980 and 1 Jy in November 1995. The western hot spot (labeled as H2 in Figure C.2) has increased in flux density, as well as a knot in the western jet (labeled as K2), which was not visible as a local maximum in the 1980 VLA image.

By aligning the core positions at both epochs, the relative separations of the various features in the source can be compared. The hot spots H1 and H2 do not show significant positionally variations but a knot, about 5 arcsec from the core in the eastern jet (labeled as K1), has shifted about half an arcsecond inwards. A close examination of the second, pure naturally weighted MERLIN image (Figure C.3) reveals that this knot K1 is composed out of two separate sub-components (labeled as K1a and K1b). These are separated by the same distance of ∼0.5 arcsec, as the shift of the blended feature in Figure C.2 and

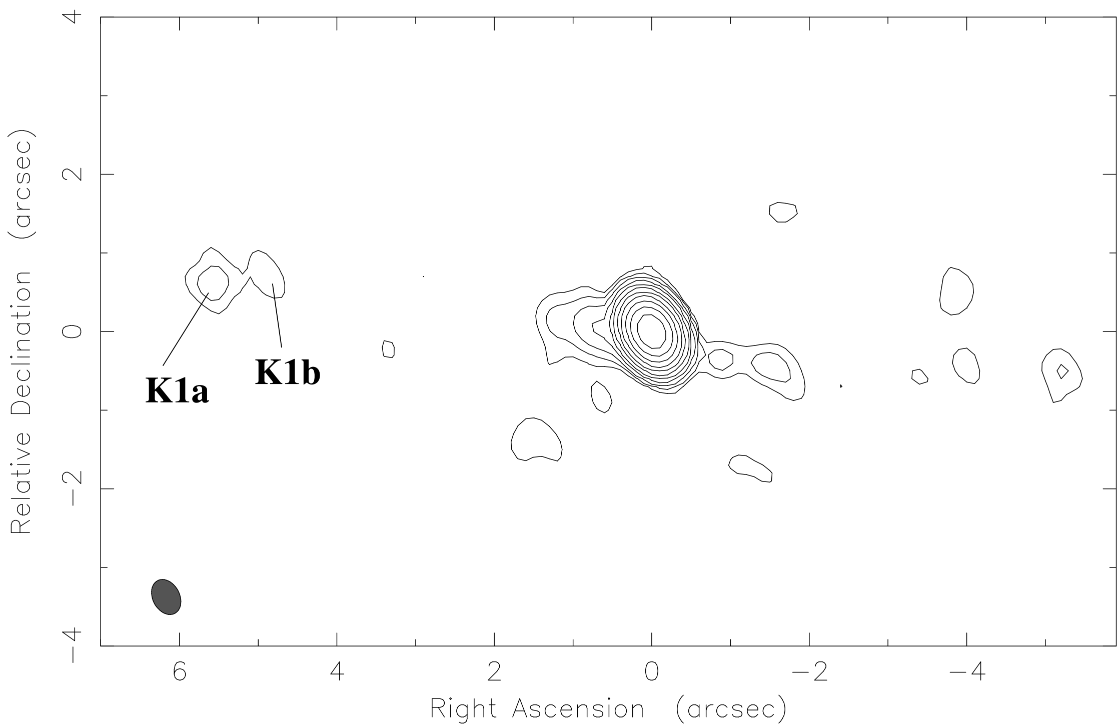

Figure C.3: The core of NGC 1052 with sub arcsecond resolution. The unresolved core has a peak flux density of 1 Jy per beam. Contours at (−0.5, 0.5, 1, 2, 4, 8, 16, 32, 64, 128, 256, 512) × 1 mJy are shown. Two sub components of knot K1 are resolved (labeled as K1a and K1b). Jet and counterjet emission can be seen up to ∼ 1.5 arcsecs from the core with a P.A. of 83° for the jet and −106° for the counterjet.

contribute comparable fractions to the combined flux density of K1. This implies that the inner sub-component K1b might have increased in flux density between 1980 and 1995, causing an apparent shift of K1. Since no high resolution 1980 image of NGC 1052 exists, this statement cannot be tested directly. Nevertheless, it appears more plausible than an inward motion of K1 by about 50 pc in 15 years, which would correspond to a jet speed of $\sim 10\,c$.

Figure C.3 shows for the first time the jet and the counterjet of NGC 1052 with sub–arcsecond resolution. The jet extends out to ∼1.5 arcsec with a P.A. of about 83°, comparable to the P.A. of the pc–scale jet. Weaker counterjet emission is also visible up to 2 arcsec west from the core. Its P.A. of ∼−106° agrees roughly with the P.A. on pc–scales, although a slight bending to the north is suggested.

The main purpose of the Merlin data within the scope of this thesis is to compare the radio structure of NGC 1052 on kpc–scales with the X-ray CHANDRA image, which will be done in Appendix D.

Appendix D

The X-ray jet of NGC 1052

The CHANDRA image of NGC 1052 is shown in Figure D.1. Strong X-ray emission from the AGN is seen in this image as well as diffuse extended emission well aligned with the radio jet, whose MERLIN image is superimposed in contours. This is the first direct detection of the X-ray jet of NGC 1052.

Close to the nucleus a tentative correlation between radio and X-ray emission can be found while the synchrotron emission in the radio lobes tends to anti-correlate with the X-ray intensity distribution. East and west of the core, there are two X-ray emitting regions, coinciding with enhanced brightness regions in the radio regime, which can also be seen in an optical image, taken by the Hubble Space Telescope (Pogge et al. 2000). The X-rays from these knots might be produced in a very different physical process than the more diffuse, extended emission. Synchrotron or inverse Compton radiation could be responsible for their brightness over this large frequency range but the poor photon statistics prevented the derivation of spectra of either knot to test this hypothesis.

To constrain the emission process of the X-ray jet, an annulus which excludes the nucleus itself but includes the whole area of the X-ray jet was selected. Two different models have been fitted to the jet–spectrum (see Figure D.2): a Raymond and Smith plasma (Raymond & Smith 1977) and a simple power–law. The power–law fit result of the X-ray jet is highly implausible, because of the extraordinary steep photon index of $\Gamma \geq 7$.

Because the radio as well as the X-ray jet are considered to be located deep inside the galaxy NGC 1052 itself, the amount of photoelectric absorption distributed along the line of sight has to be determined. Using the thermal source model, an attenuating column density of $N_{\rm HI} \simeq 3.5 \times 10^{21}\,{\rm cm^{-2}}$ is found. This value is about an order of magnitude higher than the galactic foreground column density belonging to the Milky Way of $N_{\rm HI} = 2 \times 10^{20}\,{\rm cm^{-2}}$ (Hartmann & Burton 1997). This additional X-ray attenuation can be attributed to weakly ionized gas located inside the galaxy itself. A plasma temperature of $kT = (0.5 \pm 0.2)\,{\rm keV}$ for the diffuse X-ray jet emission can be derived.

The X-ray spectrum of the nucleus: The nuclear X-ray spectrum was extracted up to a diameter of 2 arcsec. Comparing both X-ray spectra in Figure D.2 reveals the much softer X-ray emission of the jet. The bulk of the X-ray jet emission originates below $E < 2\,{\rm keV}$ while the X-ray spectrum of the nucleus has additional hard X-ray emission. ASCA as well as the ROSAT PSPC could not separate between the nucleus and the jet

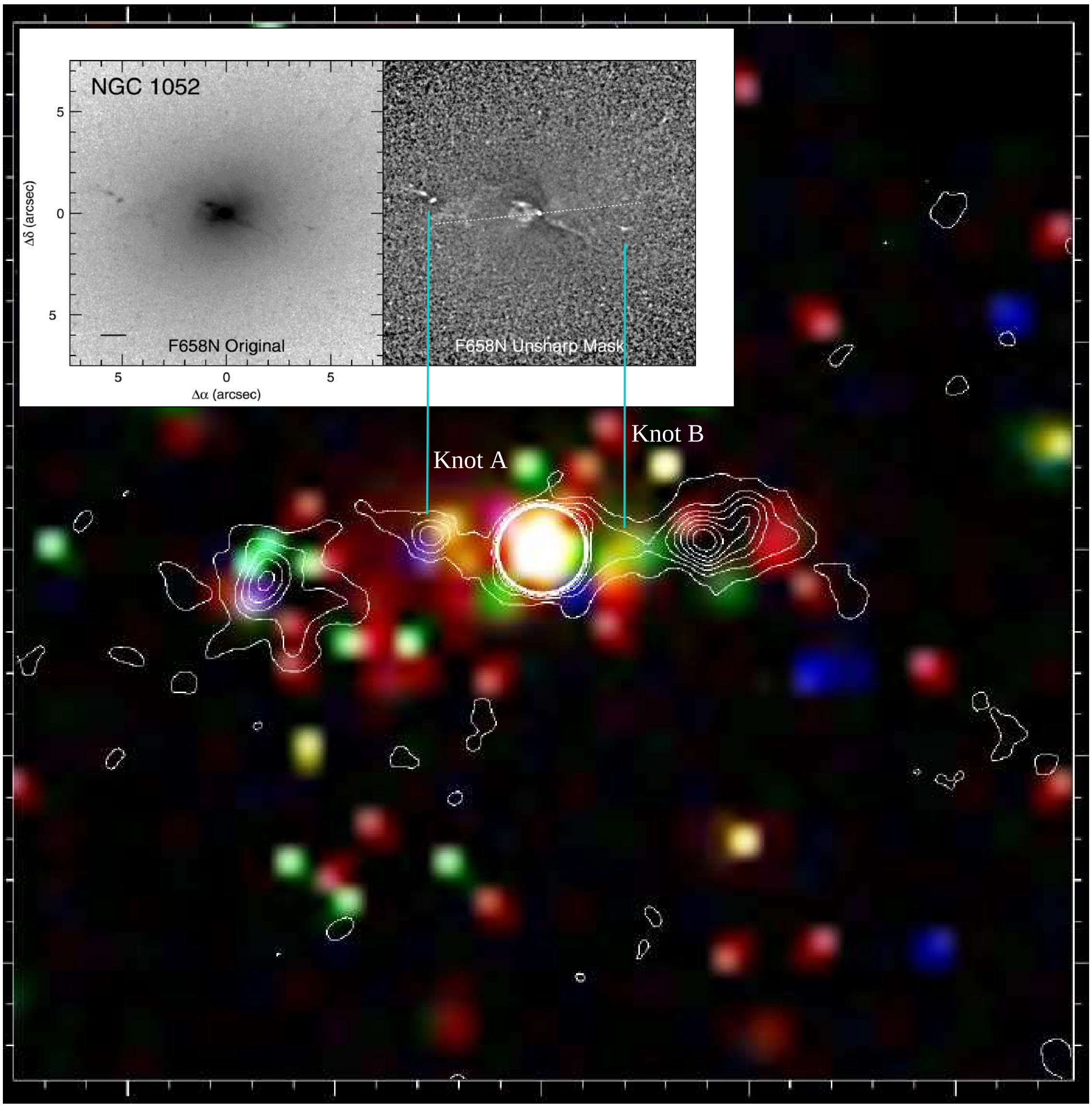

Figure D.1: The X-ray jet of NGC 1052 imaged by CHANDRA. The image has been smoothed to a resolution of $4''$ to increase sensitivity. Each tick corresponds to $2''$. Red represents photons between 0.1 and 1 keV, green between 1 and 2 keV and blue 2 to 3keV. The clipping level is 3σ. Overlaid are the contours of the 1.4 GHz Merlin map. The extended X-ray emission tends to anti-correlate with the radio-synchrotron emission. The jet emission is dominated by soft X-rays below 1 keV, whereas the AGN appears white representing a rather flat X-ray spectrum. The enclosed panel shows the optical jet (compare Figure 1.7) of NGC 1052, imaged with the HST by Pogge et al. (2000), on the same scale. Two knots, labeled as A and B, apear at the same positions as conspicuous peaks of the X-ray emission and regions of enhanced surface brightness in the radio band (K1 and K2 in the terminology of Appendix C).

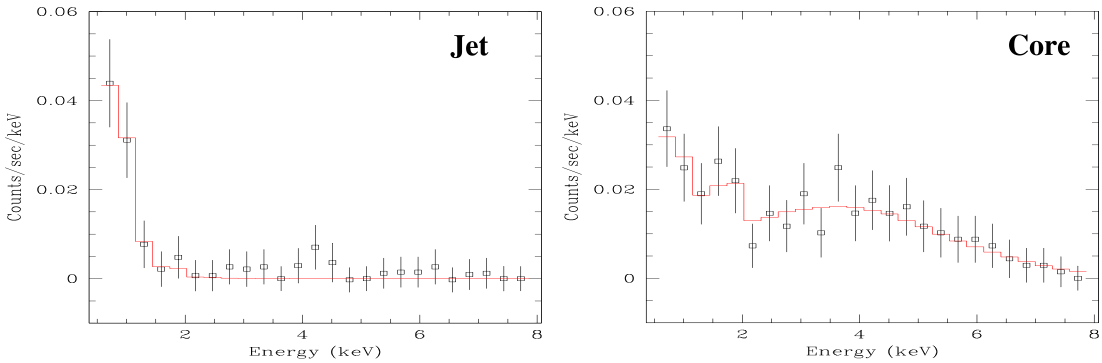

Figure D.2: X-ray spectrum of the jet (left panel) and core (right panel) of NGC 1052. The solid line indicates the best-fit model.

spatially but the soft X-ray emission of the jet was already detectable in terms of a soft excess of the X-ray spectrum in the PSPC data (see Weaver et al. 1999).

The soft X-ray emission below $E < 2\,\mathrm{keV}$ in the nuclear spectrum is at a comparable intensity level as the X-ray emission of the jet. Assuming that a fraction of the diffuse X-ray emission of the jet originates also in the extraction region of the nucleus, a hybrid model for the X-ray spectral approximation of the nuclear spectrum was used. The observed intensity distribution is written as

$$I_{\mathrm{obs}} = (I_{\mathrm{jet}} + I_{\mathrm{nucleus}} \times e^{-\sigma \times N_H(\mathrm{torus})}) \times e^{-\sigma \times N_H(\mathrm{gal.})} \quad \text{(D.1)}$$

where I_{jet} is the X-ray spectrum of the jet and I_{nucleus} is the spectrum of the nucleus. The photoelectric absorption produced by the torus is represented in Equation (D.1) by $e^{-\sigma \times N_H(\mathrm{torus})}$ while the X-ray absorption produced by the interstellar medium of the galaxy is $e^{-\sigma \times N_H(\mathrm{gal.})}$. A power–law type X-ray spectrum of the central X-ray source was assumed. The plasma temperature of the X-ray jet contribution as well as the foreground X-ray absorbing column densities were fixed to the values derived above. The best fit values are: $N_{\mathrm{H}}(\mathrm{torus}) = 0.8^{+1.5}_{-0.60} \times 10^{23}\,\mathrm{cm}^{-2}$ and $\Gamma = 0.38^{0.31}_{-0.21}$. The absorbed X-ray flux is $F_{\mathrm{X}}(0.3\,-\,8.0\,\mathrm{keV}) = (4.3\,\pm\,1.4) \times 10^{-12}\,\mathrm{erg\,s^{-1}\,cm^{-2}}$.

The derived $N_{\mathrm{H}}(\mathrm{torus})$ is rather low. Data of other X-ray observatories imply much higher values for both, the $N_{\mathrm{H}}(\mathrm{torus})$ as well as Γ (Weaver et al. 1999, Guainazzi & Antonelli 1999, Guainazzi et al. 2000) but these high torus column densities are not supported by the CHANDRA data. This apparent discrepancy between the CHANDRA data and previous X-ray observations concerning the photon index can be caused by the pile–up degradation ($\sim 30\,\%$) of the CHANDRA data. The nuclear X-ray spectrum might appear flatter than expected, because of the artificial hardening of the X-ray spectrum. Taking this into consideration, the derived results are consistent with the analysis of Weaver et al. (1999) who fitted the combined ROSAT and ASCA data – both are not affected by the pile–up – and derived in general steeper X-ray photon indices using a variety of models. The determined absorbing column density, however, is not so sensitive to the pile–up effect.

Substituting I_{nucleus} from a power–law to a thermal bremsstrahlung model gave no sufficient results. In all cases the temperature values exceed the upper temperature boundary of 1 MeV.

The CHANDRA data provide for the first time direct evidence for an X-ray jet in NGC 1052 perfectly correlated in extent with the well studied radio jet. The X-ray jet can be approximated best with thermal X-ray emission of a plasma with $\mathrm{k}T = 0.5\,\mathrm{keV}$. This temperature is consistent with the thermal component found earlier by Weaver et al. (1999) using ASCA and ROSAT data. Its unabsorbed flux is $F_{\mathrm{X-ray\,jet}}(0.3 - 8.0\,\mathrm{keV}) = (1.7 \pm 0.8) \times 10^{-13}\,\mathrm{erg\,s^{-1}\,cm^{-2}}$, only 2% of the X-ray emission of the nucleus. Because of the strong pile–up degradation of the CHANDRA data, no firm conclusions on the X-ray spectrum of the nucleus can be deduced.

The absorbing column density of ionized material towards the approaching VLBI–jet derived from the brightness temperature distribution is of the order of $\sim 6 \cdot 10^{22}\,\mathrm{cm^{-2}}$. This is in a good agreement with the absorbing column density of neutral hydrogen ($0.8^{+1.5}_{-0.60} \cdot 10^{22}\,\mathrm{cm^{-2}}$) derived from X-ray spectroscopy of the compact X-ray core of NGC 1052.

Appendix E

NGC 1052 – The film

To give an visual impression of the full multi-frequency structure of NGC 1052 the aligned CLEAN maps were used to produce a movie from the aligned CLEAN models of the Difmap output, interpolating them with a linear model, creating FITS-images (Flexible Image Transport System, Wells et al. 1981) and producing GIF-files (Graphic Interchange Format) from these using the WIP package (Morgan 1995). The resulting set of GIF-files was concatenated using the program FMP (Fast Movie Processor, Copyright 1997-1999 R. Tibljas and Z. Nicolic).

There are two different versions of this movie available, one "Hollywood version" (`http://www.mpifr-bonn.mpg.de/staff/mkadler/hollywood_1052.avi`) which starts at 5 GHz with a field of view of 40 mas zooming into the center of the galaxy as the frequency is tuned up. In a second ("Ufa") version of the movie (`http://www.mpifr--bonn.mpg.de/staff/mkadler/ufa_1052.avi`) a fixed field of view and a fixed beamsize of 1×0.5 mas (corresponding to the resolution at 2 cm) was chosen. A close inspection of the "Ufa" version of the film shows clearly the stationary emission regions in the outer parts of both jets fading away towards higher frequencies, the region B showing up at the base of the western jet above 5 GHz and the core of the eastern jet moving inwards slowly as expected in the case of a conical jet model (see Section 4.6). The choice of 1×0.5 mas for the beam makes the movie superresolved below 15 GHz. For this reason one has to be careful in order not to overinterprete this part. However, the movie is still a valid representation of the dynamics of the derived model which is not bordered by a special beamsize.

Two sequences of frames from each version of the movie are shown in Figure E.1. In various sections of this thesis the movie can be used as a helpful tool to visualize the discussed effects (opacity changes in various jet regions, core shift). As it exhibits clearly many aspects of general jet physics the movie is also meant to serve as an educational tool.

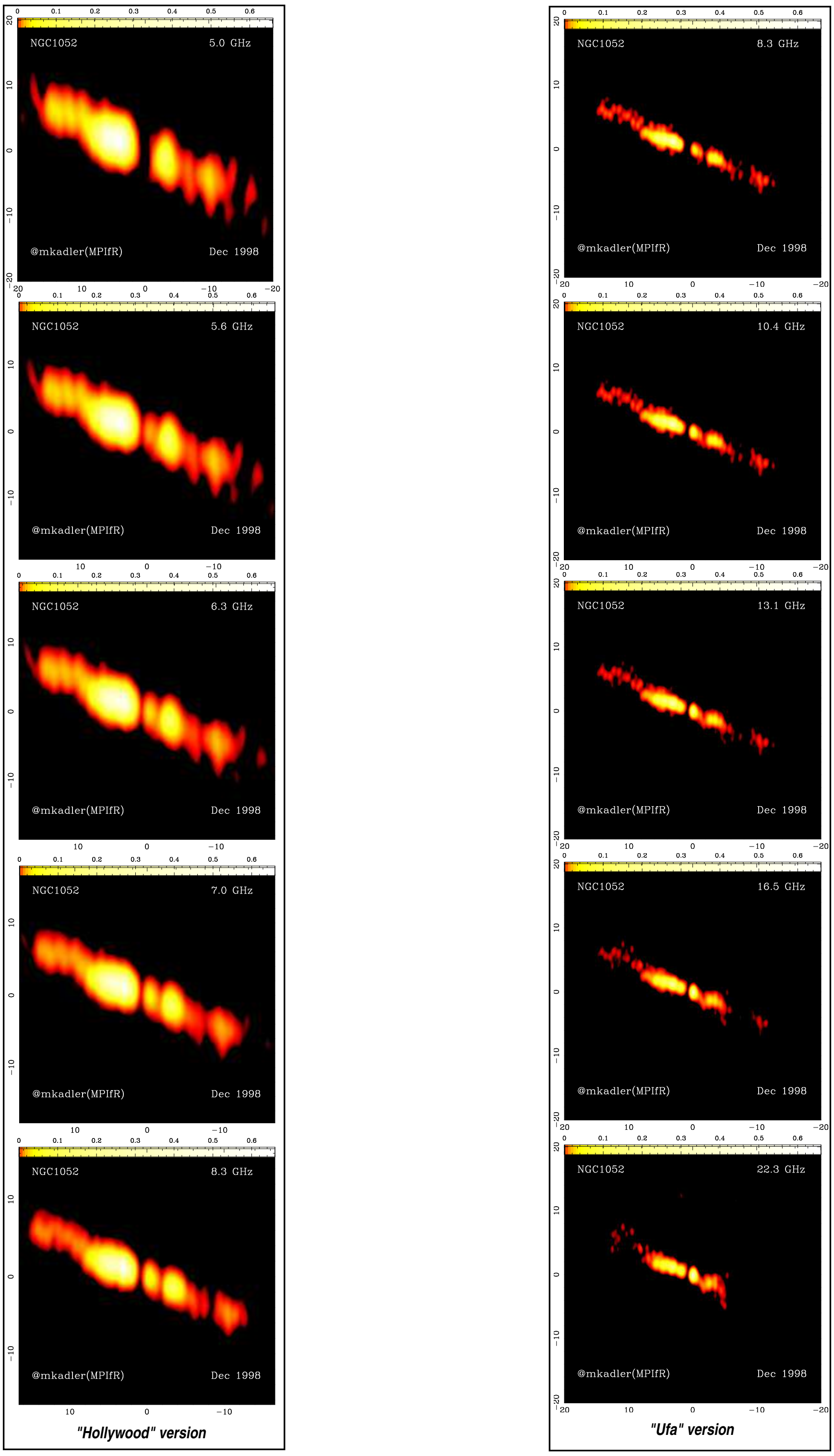

Figure E.1: Sequences of frames from the two versions of the NGC 1052-movie. Left panel: 5 frames from the “Hollywood” version of the film, showing the source evolution from 5 to 8.4 GHz. The field of view and the beam size are optimized for the special frequency of each frame. The appearance of component B at the core of the western jet is seen very clearly. Right panel: 5 frames from the “Ufa” version of the film between 8.4 and 22 GHz. The field of view is kept fixed for a better comparison of positional shifts with frequency. The beam size corresponds to the VLBA-beam at 15 GHz. The core shift in the eastern jet is very pronounced and positionally stationary features in the outer parts of both jets fade away towards higher frequencies (optically thin regime). Both movies can be obtained in the Internet from the URLs: `http://www.mpifr-bonn.mpg.de/staff/mkadler/zoom_1052.avi`, respectively `http://www.mpifr-bonn.mpg.de/staff/mkadler/ufa_1052.avi`.

Bibliography

Barth, A. J., Filippenko, A. V., & Moran, E. C. 1999, Astrophys. J., 515, L61

Bayer, J. 1603, Uranometria (Augsburg)

Becklin, E. E., Tokunaga, A. T., & Wynn-Williams, C. G. 1982, Astrophys. J., 263, 624

Blandford, R. D. & Königl, A. 1979, Astrophys. J., 232, 34

Blumenthal, G. R. & Gould, R. J. 1970, Reviews of Modern Physics, 42, 237

Braatz, J. A., Wilson, A. S., & Henkel, C. 1996, Astrophys. J. Suppl., 106, 51

Brown, R. L. 1987, in Spectroscopy of Astrophysical Plasmas, 35–58

California Institute of Technology. 1991, BAAS, 23, 991

Claussen, M. J., Diamond, P. J., Braatz, J. A., Wilson, A. S., & Henkel, C. 1998, Astrophys. J., 500, L129

Condon, J. J., Condon, M. A., Gisler, G., & Puschell, J. J. 1982, Astrophys. J., 252, 102

Daly, R. A. & Marscher, A. P. 1988, Astrophys. J., 334, 539

de Vries, W. H., Barthel, P. D., & O'Dea, C. P. 1997, Astron. & Astrophys., 321, 105

Eckart, A. & Genzel, R. 1996, Nature, 383, 415

Falcke, H. & Biermann, P. L. 1995, Astron. & Astrophys., 293, 665

Falcke, H., Wilson, A. S., & Simpson, C. 1998, Astrophys. J., 502, 199

Fomalont, E. 1981, Newsletter. NRAO No. 3, p. 3, 1981, 3, 3

Forbes, D. A., Georgakakis, A. E., & Brodie, J. P. 2001, Monthly Not. Roy. Astron. Soc., 325, 1431

Fosbury, R. A. E., Mebold, U., Goss, W. M., & Dopita, M. A. 1978, Monthly Not. Roy. Astron. Soc., 183, 549

Gómez, J. L., Marscher, A. P., Alberdi, A., Jorstad, S. G., & García-Miró, C. 2000, Science, 289, 2317

Gabel, J. R., Bruhweiler, F. C., Crenshaw, D. M., Kraemer, S. B., & Miskey, C. L. 2000, Astrophys. J., 532, 883

Gallagher, J. S. 1986, Publ. Astron. Soc. Pacific, 98, 81

Georganopoulos, M. & Marscher, A. P. 1996, in ASP Conf. Ser. 100: Energy Transport in Radio Galaxies and Quasars, 67

Guainazzi, M. & Antonelli, L. A. 1999, Monthly Not. Roy. Astron. Soc., 304, L15

Guainazzi, M., Oosterbroek, T., Antonelli, L. A., & Matt, G. 2000, Astron. & Astrophys., 364, L80

Harris, D. E., Carilli, C. L., & Perley, R. A. 1994, Nature, 367, 713

Harris, D. E. & Krawczynski, H. 2002, Astrophys. J., 565, 244

Hartmann, D. & Burton, W. B. 1997, Atlas of galactic neutral hydrogen (Cambridge; New York: Cambridge University Press)

Heeschen, D. S. 1970, Astron. J., 75, 523

Heeschen, D. S. & Puschell, J. J. 1983, Astrophys. J., 267, L11

Hevelius, J. 1690, Firmamentum Sobiescianum sive Uranographia (Gdansk)

Ho, L. C., Filippenko, A. V., & Sargent, W. L. 1995, Astrophys. J. Suppl., 98, 477

Ho, L. C., Filippenko, A. V., & Sargent, W. L. W. 1997, Astrophys. J. Suppl., 112, 315

Högbom, J. A. 1983, in Indirect Imaging. Measurement and Processing for Indirect Imaging. Proceedings of an International Symposium held in Sydney, Australia, August 30-September 2, 1983. Editor, J.A. Roberts; Publisher, Cambridge, England, New York, USA, Cambridge University Press, 1984, 247

Johnston, K. J., Fey, A. L., Zacharias, N., Russell, J. L., Ma, C., de Vegt, C., Reynolds, J. E., Jauncey, D. L., Archinal, B. A., Carter, M. S., Corbin, T. E., Eubanks, T. M., Florkowski, D. R., Hall, D. M., McCarthy, D. D., McCulloch, P. M., King, E. A., Nicolson, G., & Shaffer, D. B. 1995, Astron. J., 110, 880

Jones, D. L., Tingay, S. J., Murphy, D. W., Meier, D. L., Jauncey, D. L., Reynolds, J. E., Tzioumis, A. K., Preston, R. A., McCulloch, P. M., Costa, M. E., Kemball, A. J., Nicolson, G. D., Quick, J. F. H., King, E. A., Lovell, J. E. J., Clay, R. W., Ferris, R. H., Gough, R. G., Sinclair, M. W., Ellingsen, S. P., Edwards, P. G., Jones, P. A., van Ommen, T. D., Harbison, P., & Migenes, V. 1996, Astrophys. J., 466, L63

Jones, D. L., Wehrle, A. E., Meier, D. L., & Piner, B. G. 2000, Astrophys. J., 534, 165

Jones, D. L., Wrobel, J. M., & Shaffer, D. B. 1984, Astrophys. J., 276, 480

Kameno, S., Sawada-Satoh, S., Inoue, M., Shen, Z., & Wajima, K. 2001, Publ. Astron. Soc. Japan, 53, 169

Kellermann, K. I., Vermeulen, R. C., Cohen, M. H., & Zensus, J. A. 1999, in American Astronomical Society Meeting, Vol. 194, #20.02

Kellermann, K. I., Vermeulen, R. C., Zensus, J. A., & Cohen, M. H. 1998, Astron. J., 115, 1295

Kemball, A. J., Diamond, P. J., & Cotton, W. D. 1995, Astron. &. Astrophys. Suppl., 110, 383

Knapp, G. R., Faber, S. M., & Gallagher, J. S. 1978, Astron. J., 83, 139

Krichbaum, T. P., Alef, W., Witzel, A., Zensus, J. A., Booth, R. S., Greve, A., & Rogers, A. E. E. 1998, Astron. & Astrophys., 329, 873

Krolik, J. H. 1999, Active galactic nuclei : from the central black hole to the galactic environment (Princeton, NJ, USA : Princeton University Press, 1999.)

Leppänen, K. J., Zensus, J. A., & Diamond, P. J. 1995, Astron. J., 110, 2479

Levinson, A., Laor, A., & Vermeulen, R. C. 1995, Astrophys. J., 448, 589+

Lobanov, A. P. 1998, Astron. & Astrophys., 330, 79

Marr, J. M., Taylor, G. B., & Crawford, F. 2000, in Astrophysical Phenomena Revealed by Space VLBI, Proceedings of the VSOP Symposium, held at the Institute of Space and astronautical Science, Sagamihara, Kanagawa, Japan, January 19 - 21, 2000, Eds.: H. Hirabayashi, P.G. Edwards, and D.W. Murphy, Sagamihara, Kanagawa, Japan: Institute of Space and astronautical Science, 2000, 91

Mayall, N. U. 1939, Lick Observatory Bulletin, 497, 33

McDowell, J. C. 1994, in Einstein Obs. Unscreened IPC Data Archive

Mirabel, I. F. & Rodríguez, L. F. 1999, Annu. Rev. Astron. Astrophys., 37, 409

Miyoshi, M., Moran, J., Herrnstein, J., Greenhill, L., Nakai, N., Diamond, P., & Inoue, M. 1995, Nature, 373, 127

Morgan, J. A. 1995, in ASP Conf. Ser. 77: Astronomical Data Analysis Software and Systems IV, Vol. 4, 129

Napier, P. J. 1994, in IAU Symp. 158: Very High Angular Resolution Imaging, Vol. 158, 117

Omar, A., Anantharamaiah, K. R., Rupen, M., & Rigby, J. 2002, Astron. & Astrophys., 381, L29

Pearson, T. J., Shepherd, M. C., Taylor, G. B., & Myers, S. T. 1994, in American Astronomical Society Meeting, Vol. 185, #08.08

Peterson, B. M. 1997, An introduction to active galactic nuclei (Cambridge, UK, New York, USA: Cambridge University Press)

Pogge, R. W., Maoz, D., Ho, L. C., & Eracleous, M. 2000, Astrophys. J., 532, 323

Raymond, J. C. & Smith, B. W. 1977, Astrophys. J. Suppl., 35, 419

Ros, E. 1997, Astrometría diferencial de precisión con VLBI en el triángulo de Draco (y estudios de SN 1993J) (València, Spain: Servicio de Publicaciones, Universitat de València), 35

Rybicki, G. B. & Lightman, A. P. 1979, Radiative Processes in Astrophysics (New York, USA: Wiley-Interscience)

Schwartz, D. A., Marshall, H. L., Lovell, J. E. J., Piner, B. G., Tingay, S. J., Birkinshaw, M., Chartas, G., Elvis, M., Feigelson, E. D., Ghosh, K. K., Harris, D. E., Hirabayashi, H., Hooper, E. J., Jauncey, D. L., Lanzetta, K. M., Mathur, S., Preston, R. A., Tucker, W. H., Virani, S., Wilkes, B., & Worrall, D. M. 2000, Astrophys. J., 540, L69

Smith, D. A., Wilson, A. S., Arnaud, K. A., Terashima, Y., & Young, A. J. 2002, Astrophys. J., 565, 195

Thompson, A. R., Moran, J. M., & Swenson, G. W. 1986, Interferometry and synthesis in radio astronomy (New York, Wiley-Interscience)

Tingay, S. J. & Murphy, D. W. 2001, Astrophys. J., 546, 210

Van Gorkom, J. H., Knapp, G. R., Raimond, E., Faber, S. M., & Gallagher, J. S. 1986, Astron. J., 91, 791

Vermeulen, R. C., Readhead, A. C. S., & Backer, D. C. 1994, Astrophys. J., 430, L41

Vermeulen, R. C., Ros, E., Kellermann, K. I., Cohen, M. H., & Zensus, J. A. 2002, in prep.

Wagner, S. J. & Witzel, A. 1995, Annu. Rev. Astron. Astrophys., 33, 163

Weaver, K. A., Wilson, A. S., Henkel, C., & Braatz, J. A. 1999, Astrophys. J., 520, 130

Wells, D. C., Greisen, E. W., & Harten, R. H. 1981, Astron. &. Astrophys. Suppl., 44, 363

Wilson, A. S. & Yang, Y. 2002, Astrophys. J., 568, 133

Wilson, A. S., Young, A. J., & Shopbell, P. L. 2000, Astrophys. J., 544, L27

Wrobel, J. M. 1984, Astrophys. J., 284, 531

Young, A. J., Wilson, A. S., Terashima, Y., Arnaud, K. A., & Smith, D. A. 2002, Astrophys. J., 564, 176

Yusef-Zadeh, F., Melia, F., & Wardle, M. 2000, Science, 287, 85

Zensus, J. A. 1997, Annu. Rev. Astron. Astrophys., 35, 607

Zensus, J. A., Ros, E., Kellermann, K. I., Cohen, M. H., Vermeulen, R. C., & Kadler, M. 2002, in press (Astron. J., issue August 2002)

Danksagung

Ich möchte mich bei allen Menschen bedanken, die mich bei der Fertigstellung dieser Diplomarbeit unterstützt haben.

PD Dr. Heino Falcke danke ich für die Übernahme des Referats und viele hilfreiche Tipps und Anregungen während der letzten Monate.

Prof. Dr. Uli Klein danke ich fuer die Übernahme des Koreferats.

Dr. J. Anton Zensus gab mir schon in einer frühen Phase meines Studiums die Möglichkeit, einen Einblick in den Alltag an einem wissenschaftlichen Institut zu gewinnen. Während der drei Jahre, in denen ich als studentische Hilfskraft für ihn tätig war, konnte ich vieles lernen, was mir einen "*running start*" in die Diplomarbeit verschafft hat. Darüber hinaus danke ich ihm für die Bereitstellung des Themas dieser Arbeit und die Einbindung in darüber hinausgehende wissenschaftliche Projekte.

Den größten unmittelbaren Einfluss auf das Gelingen dieser Arbeit hatte zweifelsohne Dr. Eduardo Ros Ibarra. Seiner unermesslichen Geduld und Hilfsbereitschaft habe ich vieles zu verdanken, insbesondere die Orientierung in den Wirren der VLBI-Datenauswertung. Für seine Unterstützung möchte ich ihm von Herzen danken.

Den Gründungsmitgliedern des *VLBA 2cm-Survey*, Dr. Ken I. Kellermann, Dr. Rene C. Vermeulen, Dr. J. Anton Zensus, und Dr. Marshall H. Cohen danke ich für die Möglichkeit der Zusammenarbeit in diesem Projekt.

Dr. Andrei P. Lobanov danke ich für die zahlreichen Hinweise und Diskussionen, sowie für die Bereitstellung der Daten, die die Grundlage dieser Arbeit bilden.

Dr. Jürgen Kerp danke ich für die Reduktion der CHANDRA Daten und die vielen klärenden Gespräche, die im Zuge der Auswertung dieser Daten nötig waren.

Dr. Thomas P. Krichbaum, Dr. Richard W. Porcas, Dr. Yoshiaki Hagiwara, Dr. Alan Roy und Jens Klare möchte ich für diverse Tipps und Hilfestellungen während der Datenauswertung und Interpretation der Ergebnisse danken.

Dr. Alexander Kraus danke ich für die Durchführung zahlreicher Messungen am Effelsberger 100 m Teleskop, die in diese Arbeit eingeflossen sind. Ebenso danke ich Dr. Hans Ungerechts und Jens Kauffmann für die Flussdichtebestimmungen von NGC 1052 am Pico

Veleta.

Dr. Andrea Tarchi möchte ich herzlich danken für seine Hilfe bei der Posterpräsentation auf der SRT Konferenz.

Edwin Hammer danke ich für die Durchsicht des Manuskripts und die vielen hilfreichen Hinweise.

Ein besonderer Dank gilt allen Studenten im "Kinderzimmer" (0.20) des Max–Planck–Instituts für Radioastronomie. In chronologischer Reihenfolge ihres Auftretens dort während der letzten Jahre sind dies: Dr. Bernd Weferling, Dr. Michaela Kraus, Andrea Löhr, Maik Wolleben, Hauke Voss, Maja Tisljar und Jens Kauffmann. In wechselnder Besetzung haben wir es stets geschafft diesem Ort einen besonderen Geist einzuhauchen.

Meinem Lehrer Henner Funk möchte ich ganz herzlich danken dafür, dass er mir die Augen geöffnet hat für *die Wunder der Physik*.

Meinem Vater danke ich für seine Unterstützung und Hilfe, auf die ich mich in allen Lebenslagen stets verlassen kann.

Meiner Mutter danke ich für alles, was sie für mich getan hat, ganz besonders für die unzähligen Male, da sie ihr Lexikon studierte, um meine Fragen zu beantworten.

Zu guter Letzt danke ich Dir, Aga, für Deine Liebe und dafür, dass Du mir immer die Augen für die wirklich wichtigen Dinge im Leben offen hältst.

Ich versichere, daß ich die vorliegende Arbeit selbständig verfaßt und keine anderen als die angegebenen Quellen und Hilfsmittel benutzt sowie die Zitate kenntlich gemacht habe.

Referent: PD Dr. H. Falcke
Koreferent: Prof. Dr. U. Klein